



HAL
open science

Development and characterization of perovskite based devices: field effect transistors and solar cells

Noélia Devesa Canicoba

► **To cite this version:**

Noélia Devesa Canicoba. Development and characterization of perovskite based devices: field effect transistors and solar cells. Micro and nanotechnologies/Microelectronics. Université de Rennes1, 2018. English. NNT: . tel-02441378

HAL Id: tel-02441378

<https://hal.science/tel-02441378>

Submitted on 15 Jan 2020

HAL is a multi-disciplinary open access archive for the deposit and dissemination of scientific research documents, whether they are published or not. The documents may come from teaching and research institutions in France or abroad, or from public or private research centers.

L'archive ouverte pluridisciplinaire **HAL**, est destinée au dépôt et à la diffusion de documents scientifiques de niveau recherche, publiés ou non, émanant des établissements d'enseignement et de recherche français ou étrangers, des laboratoires publics ou privés.

THESE DE DOCTORAT DE

L'UNIVERSITE DE RENNES 1
COMUE UNIVERSITE BRETAGNE LOIRE

ECOLE DOCTORALE N° 601
*Mathématiques et Sciences et Technologies
de l'Information et de la Communication*
Spécialité : Electronique

Par

Noelia Devesa Canicoba

**Development and characterization of perovskite based devices:
field effect transistors and solar cells**

Thèse présentée et soutenue à Rennes, le 21 Décembre 2018

Unité de recherche : IETR-CNRS 6164

Rapporteurs avant soutenance :

Antoine Goullet Professeur / École Polytechnique de l'Université de Nantes

Johann Bouclé Maître de Conférences CNRS / Université de Limoges

Composition du Jury:

Examineurs : **Jacky Even** Professeur / INSA Rennes

France Le Bihan Professeur / Université de Rennes 1

Dir. de thèse : **Laurent Le Brizoual** Professeur / Université de Rennes 1

Co-dir. de thèse : **Régis Rogel** Maître de Conférences / Université de Rennes 1

Invité(s)

Aditya Mohite Maître de Conférences / Université de Rice (USA)

TABLE DES MATIERES

Introduction	1
Chapter 1. Hybrid perovskites: introduction and applications	5
1.1 Origin.....	5
1.2 Structure and properties.....	5
1.3 Applications of organometal halide perovskites	8
1.3.1 Field effect transistors.....	8
1.3.2 Solar cells.....	12
1.3.3 LEDs	16
1.3.4 Radiation detectors.....	17
1.3.5 Optically pumped lasers.....	18
1.4 References	20
Chapter 2. Fabrication and characterization	23
2.1 Fabrication techniques	23
2.1.1 Solar cells.....	23
2.1.1.1 Perovskite preparation	23
2.1.1.2 Solar cells fabrication	25
2.1.1.3 Working principle.....	28
2.1.1.4 Characterization and extraction of device performances	29
2.1.2 Field effect transistors.....	32
2.1.2.1 Perovskite preparation	32
2.1.2.2 FET fabrication.....	35
2.1.2.2.1 Insulator deposition/growth	36
2.1.2.2.2 Metal electrodes deposition.....	39
2.1.2.3 Working principle.....	40
2.1.2.4 Characterization and extraction of devices parameters	43
2.2 Characterization techniques.....	45
2.2.1 Microscope techniques.....	45
2.2.1.1 Optical microscope measurement.....	45
2.2.1.2 Scanning electron microscope	45
2.2.1.3 Atomic force microscope.....	46
2.2.2 Crystallinity analysis.....	47
2.2.3 Optical absorption spectroscopy	49
2.2.4 Current voltage curves	49
2.2.4.1 Solar cells characterization.....	49
2.2.4.2 Field effect transistor characterization	50
2.3 References	51
Chapter 3. Hybrid perovskite based field effect transistors.....	53

3.1	Introduction	53
3.2	Motivation	53
3.3	Experimental section	54
3.4	Characterization and analysis of structural and optical properties for large grain size perovskite based films	54
3.5	Perovskite based FETs operating at room temperature	57
3.5.1	Perovskite based FETs characterization using HfO ₂ as dielectric	57
3.5.2	Perovskite based FETs characteristics after consecutive cycles of measurements	62
3.5.3	Channel length variation effect on lead iodide perovskite FETs	67
3.5.4	Impact of gate insulator on lead iodide perovskite based FETs	69
3.6	Conclusion	76
3.7	References	78
Chapter 4. Mixed cation perovskite based field effect transistors		81
4.1.	Introduction	81
4.2.	Motivation	81
4.3.	Characterization and analysis of structural and optical properties for large grain sized perovskite based thin films	81
4.4.	Mixed cation perovskite based FETs.....	85
4.5.1.	Devices performances FA _{0.5} MA _{0.25} CS _{0.25} PbI ₃	89
4.5.2.	Stability and reproducibility of mixed cation and lead iodide perovskite based FETs	91
Chapter 5. Perovskite based solar cells fabricated in different atmospheres		97
5.1	Introduction	97
5.2	Introduction	97
5.3	Perovskite solar cells processed under air	97
5.3.1	Characterization of perovskite thin film quality	97
5.3.2	Perovskite solar cells fabricated under air conditions.....	100
5.3.3	Effect of perovskite thickness: morphology analysis and device performances of perovskite solar cells.....	104
5.3.4	Effect of annealing temperature on mixed halide perovskite: morphology analysis and device performances of perovskite solar cells	110
5.4	Perovskite solar cells processed under nitrogen ambient	114
5.4.1	Comparison of perovskite solar cells fabricated under different atmospheres	114
5.4.2	Improvement of solar cells processed in nitrogen via HTL modification	117
5.4.3	Stability of perovskite solar cells fabricated under a controlled atmosphere	119
5.5	Conclusion	121
5.6	References	122
CONCLUSION AND PERSPECTIVES		125

RÉSUMÉ EN FRANÇAIS..... 130

LIST OF ABBREVIATIONS

AFM :	Atomic force microscope
Al :	Aluminum
ALD :	Atomic layer deposition
Cs :	Cesium
DMF :	Dimethylformamide
DMSO :	Dimethyl sulfoxide
DSSCs :	Dye-sensitized solar cell
EL :	Electroluminescence
ETL :	Electron transport layer
FA :	Formamidinium
FETs :	Field effect transistors
GIWAXS :	Grazing-Incidence Wide-Angle X-ray Scattering
HfO₂ :	Hafnium dioxide
HTL :	Hole transport layer
IR :	Infrared radiation
ITO :	Indium tin oxide
LEDs :	Light-emitting diode
MA :	Methylammonium
MIS :	Metal insulator semiconductor
NIR :	Near-infrared
PbCl₂ :	Lead(II) chloride
PbI₂ :	Lead (II) iodide
PCBM :	[6,6]-phenyl-C61-butyric acid methyl ester
PCE :	Power conversion efficiency
PECVD :	Plasma-enhanced chemical vapor deposition
PeLEDs:	Perovskite based light emitting diodes
PFETs :	Perovskite based field effect transistors
PLQY :	Photoluminescence quantum yield
PSCs :	Perovskite based solar cells
PV :	Photovoltaic
RH :	Relative humidity

List of abbreviations

RPM :	Revolutions per minute
SEM :	Scanning electron microscope
Si₃N₄ :	Silicon nitride
SiO₂ :	Silicon dioxide
TDMAH :	Tetrakis(dimethylamino)hafnium(IV)
UV :	Ultraviolet
XrD :	X-ray diffraction

INTRODUCTION

Nowadays, the emergence of hybrid perovskites as solution-processed semiconductors has raised wide spreading interest over the research community in the exploration for electronic devices, such as radiation detectors (Gamma and X-rays), optically pumped lasers, light-emitting diodes (LEDs), field effect transistors (FETs) and solar cells as main applications. This emerging material exhibits outstanding properties such as low effective mass, high carrier mobility-lifetime product, weak exciton binding energy at room temperature, unusually high defects density tolerance, low trap density[1-8] ...

However, despite being considered as an excellent semiconductor, there are many drawbacks to overcome before transferring perovskite based devices to volume production. These are the toxicity of lead (use of PbI_2), the sensitivity of the perovskite to the atmosphere, the need to use aggressive solvents... By overcoming these important drawbacks, hybrid organic-inorganic perovskite materials could be considered as a highly competitive alternative to silicon for the fabrication of solar cells which would offer promising routes for the development of low-cost, solar-based global energy solutions for the future.

For other devices, such as field effect transistors, the liquid processing offers a low cost and easy technology for printed electronics. Moreover, field effect transistors are considered as a promising platform to study the perovskite properties which have been largely predicated from the performance of solar cells and photodetectors devices. Nevertheless, the demonstration of room temperature operating field effect transistors using 3D hybrid perovskite has remained elusive in the literature.

This thesis has been carried out in two different laboratories: at the Institute of Electronic and Telecommunications of Rennes (IETR) and at the Los Alamos National Laboratory (LANL) (USA).

The objective of this thesis is to address two of the challenges related with hybrid perovskites. These are the demonstration of perovskite based field effect transistors (FET) operational at room temperature and the fabrication of perovskite solar cells under air conditions. The transistor fabrication and characterization were performed in the Light to Energy Team of

LANL directed by Adytia Mohite. The solar cells development and characterization were obtained at the Microelectronics and Microsensors Department of IETR .

More specifically, the studies carried out in this thesis are divided into five chapters as follows:

In chapter 1, we present the state of art about hybrid organic-inorganic perovskite materials. This chapter is mainly focused on the description of perovskite based devices and the major applications developed till now with this emerging material based on MA (methylammonium), Pb (lead), I (iodide) chemical species. We put special emphasis on the two applications developed in this thesis: solar cells and field effect transistors (FETs).

In chapter 2, the fabrication and characterization techniques used for the development of perovskite based solar cells and field effect transistors are explained. We give a detailed description about the materials and techniques used for their fabrication which are essential to understand the devices performances illustrated in the next chapters. The working principle of solar cells and field effect transistors are also described. The last part of the chapter is dedicated to the perovskite thin film morphological and electrical characterization techniques used in this thesis such as X-ray diffraction (XRD), Grazing-Incidence Wide-Angle X-ray Scattering (GIWAXS), optical absorbance spectrum, atomic force microscopy (AFM), scanning electron microscopy (SEM) and current voltage static measurements.

In chapter 3, we examine the feasibility of methylammonium lead iodide (MAPbI_3) perovskite based field effect transistors working at room temperature in dark conditions. This chapter is focused on the study of critical parameters impacting the devices performances, such as perovskite film quality and the gate dielectric material. This challenging study aims at understanding different specific phenomena occurring during the characterization step such as: an existing hysteresis loop, the influence of measurement scan rate, and the aging (biasing) effect.

In chapter 4, we employ mixed cation (FA/MA/Cs) PbI_3 perovskite films as active layers in field effect transistors with different Cesium (Cs) concentrations. The role of Cs on perovskite film quality and consequently on the device performances have been studied. These results are compared with those obtained in chapter 3 by using MAPbI_3 as active layer in FETs. Stability and reproducibility tests with both materials are also performed.

In chapter 5, we report a method for fabricating operational perovskite solar cells under air and normal relative humidity. Optimization of perovskite thin films in terms of thickness and

annealing temperature are correlated to the devices photovoltaic measurements. The results obtained under humid conditions are compared to the solar cells processed under nitrogen ambient. Reproducibility tests with solar cells processed under nitrogen ambient are also performed.

References

- [1] P. Gao, M. Grätzel, M.K. Nazeeruddin, Organohalide lead perovskites for photovoltaic applications, *Energy & Environmental Science*. 7 (2014) 2448–2463.
- [2] A. Chilvery, S. Das, P. Guggilla, C. Brantley, A. Sunda-Meya, A perspective on the recent progress in solution-processed methods for highly efficient perovskite solar cells, *Science and Technology of Advanced MaTerialS*. 17 (2016) 650–658.
- [3] M.D. McGehee, Materials science: fast-track solar cells, *Nature*. 501 (2013) 323.
- [4] N.J. Jeon, J.H. Noh, Y.C. Kim, W.S. Yang, S. Ryu, S.I. Seok, Solvent engineering for high-performance inorganic–organic hybrid perovskite solar cells, *Nature Materials*. 13 (2014) 897.
- [5] P. Fan, D. Gu, G.-X. Liang, J.-T. Luo, J.-L. Chen, Z.-H. Zheng, D.-P. Zhang, High-performance perovskite CH₃NH₃PbI₃ thin films for solar cells prepared by single-source physical vapour deposition, *Scientific Reports*. 6 (2016) 29910.
- [6] W. Nie, H. Tsai, R. Asadpour, J.-C. Blancon, A.J. Neukirch, G. Gupta, J.J. Crochet, M. Chhowalla, S. Tretiak, M.A. Alam, others, High-efficiency solution-processed perovskite solar cells with millimeter-scale grains, *Science*. 347 (2015) 522–525.
- [7] M.A. Green, Y. Hishikawa, W. Warta, E.D. Dunlop, D.H. Levi, J. Hohl-Ebinger, A.W. Ho-Baillie, Solar cell efficiency tables (version 50), *Progress in Photovoltaics*. 25 (2017).
- [8] J. Huang, Y. Yuan, Y. Shao, Y. Yan, Understanding the physical properties of hybrid perovskites for photovoltaic applications, *Nature Reviews Materials*. 2 (2017) 17042.

CHAPTER 1. HYBRID PEROVSKITES: INTRODUCTION AND APPLICATIONS

1.1 Origin

Perovskites take their name from the natural mineral CaTiO_3 , which was first discovered in 1839 by the German scientist, Gustav Rose, during an expedition in the Ural Mountains of Russia and is named after by Lev Perovski (1792-1856) who was the founder of the Russian Geographical Society. The general perovskite chemical formula is AMX_3 (with A a large cation, M a small cation and X an anion) and with the same crystallographic structure as the mineral perovskite CaTiO_3 [1-2].

1.2 Structure and properties

The structure of perovskite crystal was first described by Victor Goldschmidt in 1926 in his work of tolerance factors and published later in 1945 from X-ray diffraction on barium titanate (BaTiO_3) by Helen Dick Megaw. The ideal cubic structure has the B cation stabilized in an octahedral site shared with six X anions while the larger A cation occupies a cubo-octahedral site shared with twelve X anions [3-4] as illustrated in Figure 1.1.

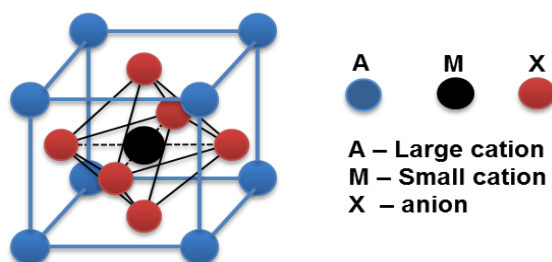


Figure 1.1. Crystal structure of perovskite where A is large cation, M is a small cation and X an anion.

The Goldschmidt tolerance factor (t) has been used extensively to predict the stability and distortion of the perovskite structure, evaluate the maximum ionic size mismatches between ions that the perovskite structure can sustain. The t factor is calculated from the ratio of the

ionic radius (Equation 1.1) in where R_A , R_B and R_X are the ionic radii of A and B site elements and oxygen, respectively.

$$t = \frac{\{R_A + R_X\}}{\{\sqrt{2(R_B + R_X)}\}} \quad (\text{Equation 1.1})$$

The relative ion size requirements are quite stringent to have a high-symmetry cubic structure [5] where tolerance values should be close to 1. Otherwise, the cubic structure will be distorted with a lowered symmetry (e. g, orthorhombic, tetragonal, rhombohedral phases) which has a direct impact in many physical properties of perovskites.

Based on the material composition of the AMX_3 crystal structure, perovskites materials are classified in two main categories[6]: inorganic oxide perovskites and halide perovskites (Figure 1.2).

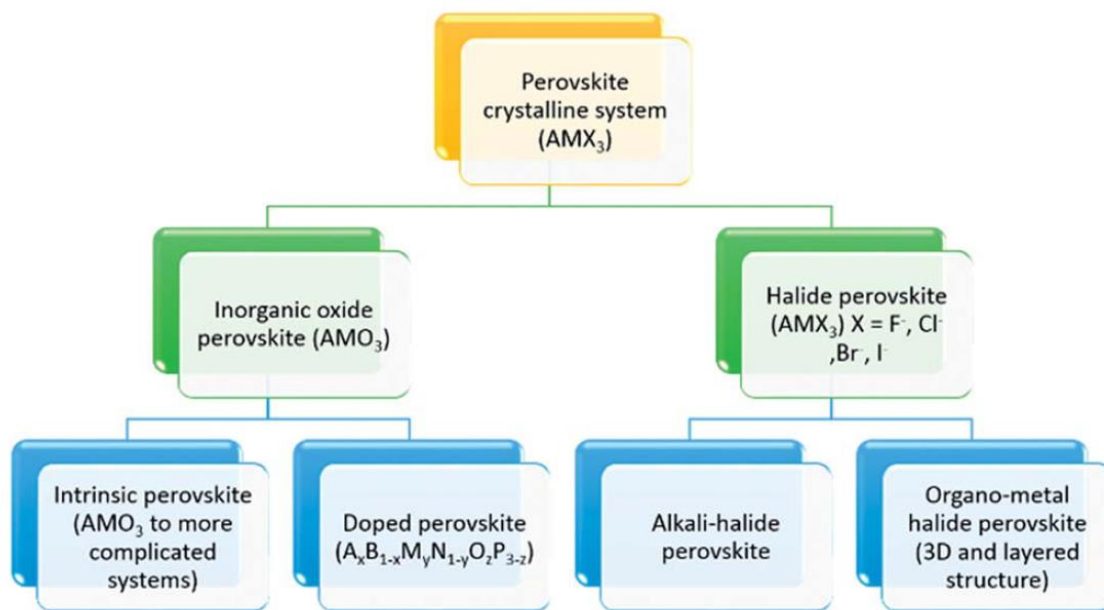


Figure 1.2. Classification of perovskite materials: Inorganic oxide perovskite and Halide perovskite[7].

Perovskite oxides have the structural formula AMO_3 or A_2MO_4 [8] as illustrated in Figure 1.3. In the first structure, AMO_3 , A-site cation is 12-fold coordinated and M-site cation is 6-fold coordinated with oxygen anions. In the A_2MO_4 structure, AMX_3 layers are alternated with AO layers.

Perovskite oxide has a variety of elements and compositions. It demonstrates several physical properties such as ferroelectricity (e.g. BaTiO₃), ferromagnetism (e.g. SrRuO₃), piezoelectricity (e.g. PbZrTiO₃), and superconductivity (Ba₂YCu₃O₇) [9–11]. Several perovskite oxides, mainly Co-, Fe- and Mn-based oxides, are well known for exhibiting high electric conductivity and surface activity to oxygen dissociation simultaneously being widely used for solid oxide fuel cells (SOFCs) and oxygen permeation membranes [9–11]. Moreover, Ta- or Ti-based perovskite is a highly important compound for application to photocatalysts due to its high catalytic activity with respect to various reactions, in particular oxidation reactions [10].

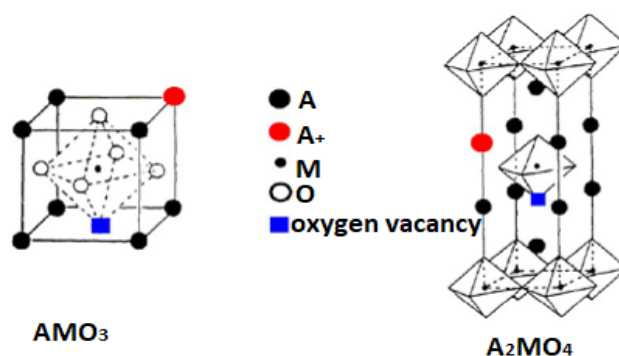


Figure 1.3. Crystal structure of perovskite oxides. a) AMO₃, b) A₂MO₄.

On the other hand, halide perovskites (AMX₃) represent an important series of the perovskite family which can be categorized into alkali-halide perovskites and organo-metal halide perovskites.

The first group, alkali-halide perovskites, is mainly formed from the monovalent alkali metal A^I (Li⁺, Na⁺, K⁺, Rb⁺, Cs⁺) and the divalent M^{II} (Be²⁺, Mg²⁺, Ca²⁺, Sr²⁺, Ba²⁺, Zn²⁺, Ge²⁺, Sn²⁺, Pb²⁺, Fe²⁺, Co²⁺, Ni²⁺) and X as the halogen anion (F⁻, Cl⁻, Br⁻, I⁻) [6]. The first time that halide perovskite was identified as a possible absorber material for photovoltaic applications was in 1980 when Salau reported KPbI₃ as a promising material for solar cells [12]. However, no real solar cell was demonstrated on this alkali metal halide perovskite material.

The second group, organometal halide perovskites, described by the generic chemical formula AMX₃ (A = organic cation, M = metal cation and X = halogen anion) represents a big crystalline family of hybrids consisting of a wide range of organic cations (A: aliphatic or aromatic ammonium) and divalent metal cations (M: Cu²⁺, Ni²⁺, Co²⁺, Fe²⁺, Mn²⁺, Pd²⁺, Cd²⁺, Ge²⁺, Sn²⁺, Pb²⁺, Eu²⁺, etc.).

In the early 1990s, Mitzi *et al.* [4] reported the use of organometal halide perovskite in field effect transistors (Figure 1.4) highlighting carrier mobilities in the range of 0.2~0.6 cm²V⁻¹s⁻¹

for m-fluorophenethylammonium-based $(C_6H_4FC_2H_4NH_3)_2SnI_4$ perovskites demonstrating for the first time the promising property of perovskites in electronic devices.

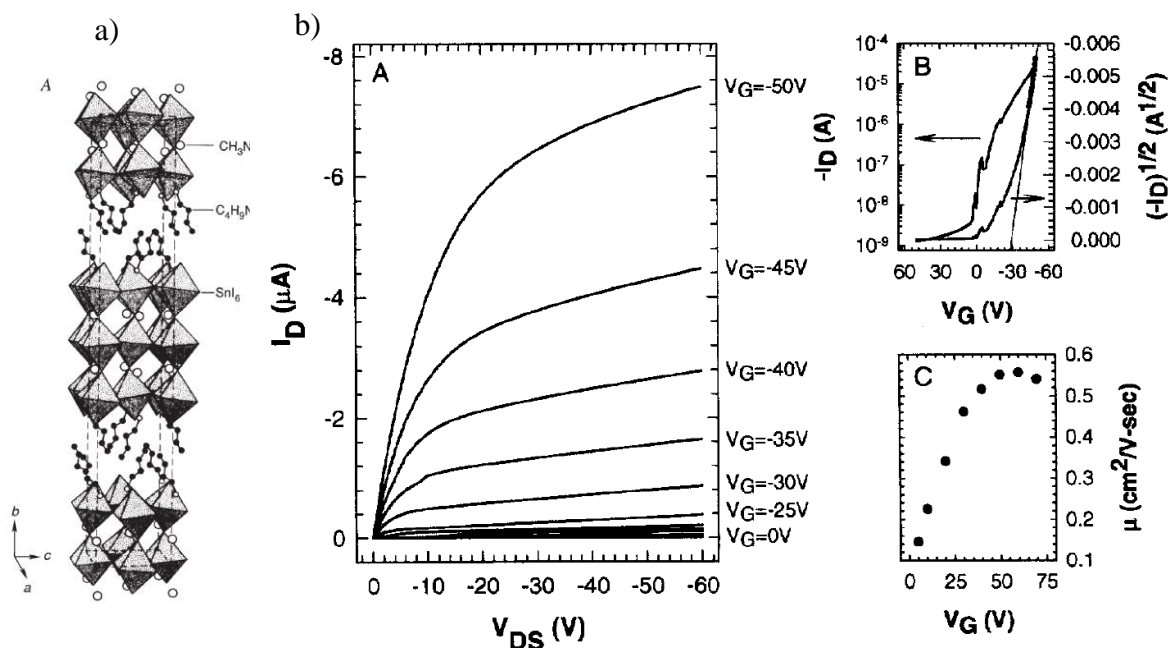


Figure 1.4. a) Polycrystalline state of hybrid perovskite used in FETs by Mitzi et al.[4]. b) Characteristics of $(C_6H_4FC_2H_4NH_3)_2SnI_4$ perovskites reported by Mitzi et al.[4].

In 2009, Miyasaka *et al.* [13] pioneered the first perovskite solar cells highlighting the potential of methylammonium lead iodide ($CH_3NH_3PbI_3$) as photoactive material. Although the photo conversion efficiency obtained at that time was quite poor ($\eta \sim 3.8\%$) it was considered as the starting point of hybrid perovskite research up-to-date.

Organometal halide perovskites combine the advantages of crystalline inorganic compounds with the organic molecules resulting in a material with outstanding properties [18–23]. The main properties are for example large absorption coefficient and tunable bandgap making them extremely attractive materials for optoelectronic devices such as solar cells [14–19], field effect transistors (FETs) [20–24], radiation detectors (Gamma and X-rays)[25–27] and optically pumped lasers[28–29] just to name a few.

1.3 Applications of organometal halide perovskites

1.3.1 Field effect transistors

The principle of field-effect transistor (FET) was first patented by Julius Edgar Lilienfeld in 1926 which was based on amplified effect of the conductivity using a device

fabricated with copper sulfide material. Nevertheless, practical semiconducting devices were not demonstrated until 1947. It was William Shockley who used the concept in practical device structure (junction field effect transistor JFET) being the starting point in various current day applications. The metal–oxide–semiconductor field-effect transistor (MOSFET), which had a profound effect on digital electronic development, was demonstrated by Dawon Kahng and Martin Atalla in 1959. FET is an ideal device for use in almost every application like analog switches, amplifiers, phase shift oscillators, choppers.... Indeed, field effect transistors are often utilized as a platform to evaluate lateral transport (opto) electronic transport properties in isotropic materials.

The first convincing demonstration of a room temperature operating hybrid perovskite FET was performed on 2D layered organic-inorganic perovskite ($(\text{C}_6\text{H}_5\text{C}_2\text{H}_4\text{NH}_3)_2\text{SnI}_4$) [24], with an $I_{\text{ON}}/I_{\text{OFF}}$ ratio of 10^4 and $\mu_{\text{FET}} \sim 0.6 \text{ cm}^2\text{V}^{-1}\text{s}^{-1}$ (Figure 1.4). Li *et al.* [23] reported MAPbI₃ phototransistors exhibiting ambipolar transport characteristics in hybrid perovskites (blue and magenta symbols in Figure 1.5) with high photocurrent and fast response ($<10 \mu\text{s}$) in comparison to previous reports on organic, quantum dots and hybrid photodetectors (typically in the order of milliseconds) [30–33]. However, without light illumination (black and red symbols in Figure 1.5) the device performances obtained exhibited very weak gate dependence highlighting the difficulty to achieve operational perovskite based field effect transistors under dark conditions at room temperature.

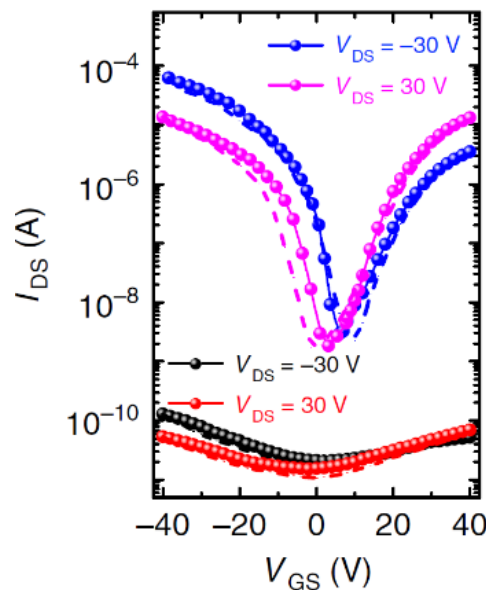


Figure 1.5. Transfer curves of the $\text{CH}_3\text{NH}_3\text{PbI}_{3-x}\text{Cl}_x$ phototransistor in the dark (black and red) and under light illumination (blue and magenta) reported by Li *et al.* [23].

Xin *et al.* [21] reported methyl ammonium lead iodide (MAPbI₃) hybrid perovskite-based FETs that only work at low temperature to overcome screening of carriers due to ionic impurities (Figure 1.6a). Otherwise, no gate modulation was observed at room temperature (Figure 1.6b) due to the screening of carriers.

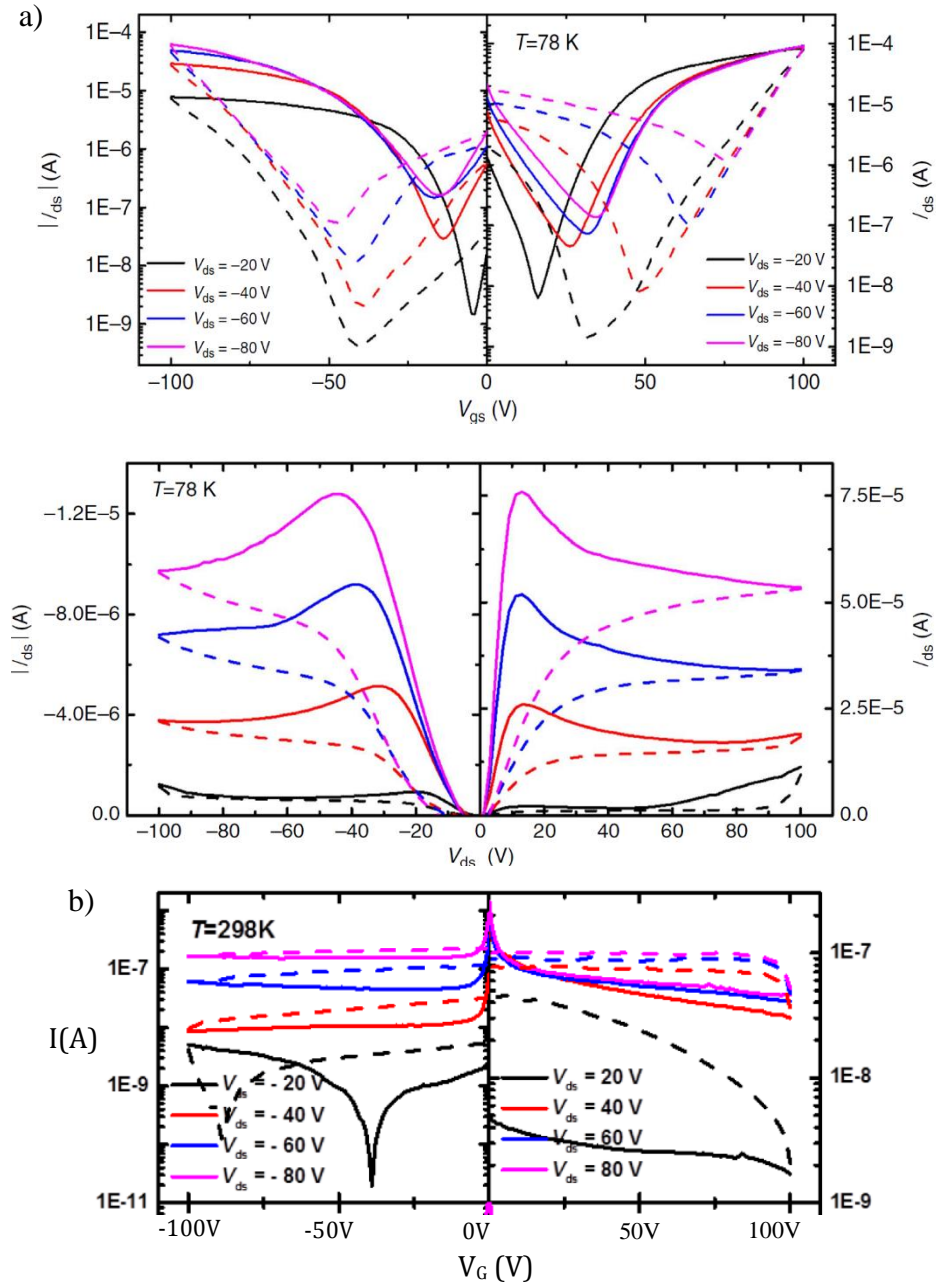


Figure 1.6. Transfer characteristics of perovskite based field effect transistors reported by Xin *et al.* [21] at a) low temperature (78K) and b) room temperature (298K).

Other reports on perovskite FETs have found unusual doping on hybrid perovskites highlighting n or p-type transport depending on the processing conditions [23–24]. Senanayak *et al.*[20] reported MAPbI₃ based FETs operating at low temperature (Figure 1.7a) and room temperature (Figure 1.7b) showing n-type transport characteristics.

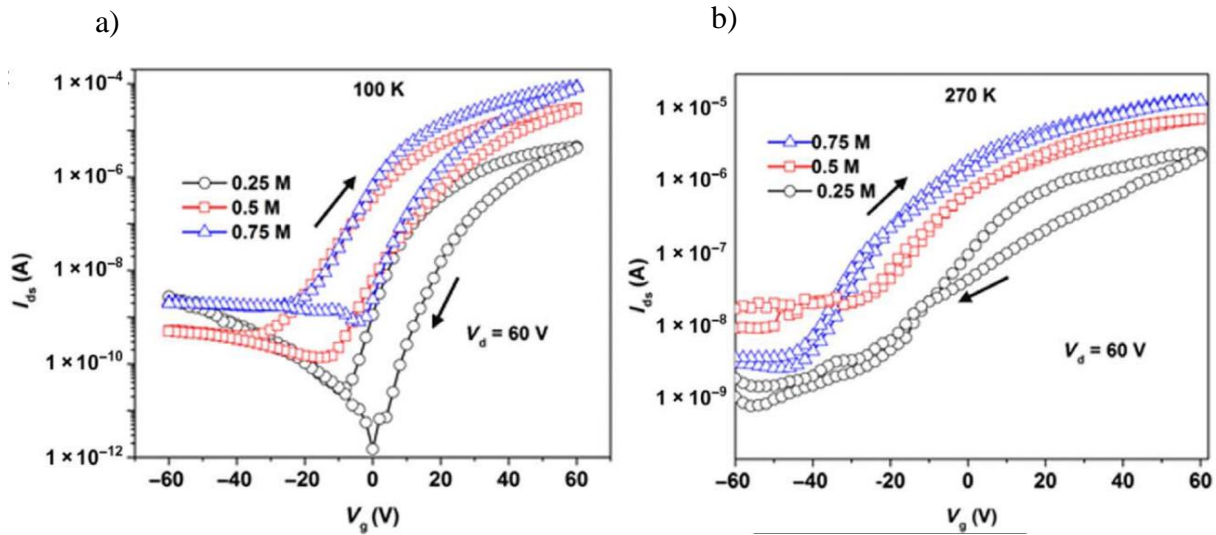


Figure 1.7. Transfer characteristics of PFETs reported by Senanayak *et al.*[20] operating at a) low and b) room temperature.

Moreover, hybrid perovskite-based field effect transistors have also been reported to exhibit hysteresis in the current-voltage characteristics during device operation [20–22]. The rapid device degradation during its operation has hindered the complete determination of the intrinsic transport properties in hybrid perovskites.

Thus, despite the intrinsic character and promising charge transport properties of perovskite which have been largely extracted from the performance of solar cells and photodetectors, the demonstration of room temperature operating FETs using 3D hybrid perovskite has remained difficult. Moreover, the intrinsic doping density ($\sim 10^{16}/\text{cm}^3$)[34], which should, in principle, facilitate ambipolar charge transport has also not been observed. This is largely due to the low channel conductivity most likely arising from the interface traps/defects, which pins the Fermi-level and prevents the effective modulation of the conductance via a capacitively coupled gate electrode. Therefore, the ability to modulate the conductance of hybrid perovskites using a FET geometry remains a key bottleneck.

The demonstration of operational FETs at room temperature is still challenging. This success could pave a way towards the utilization of such devices for different applications such as low light detection, charge detection etc. Further, it will serve as a platform for study the transport properties of hybrid perovskites.

1.3.2 Solar cells

As the energy demand is steadily growing due to the large population in the world nowadays, societies face with unprecedented challenges to meet sufficient and clean energy production. Figure 1.8 illustrates the statistical data of the percentage of each energy source in the global energy consumption (2017). The fossil energies (oil, natural gas and coal) represent around the 85% in the total energy need. However, it is well-known that these types of energy are in limited quantity. The renewable energy sources are expected to satisfy a clean and unlimited supply. This kind of energy is currently growing faster than others sources of energy production.

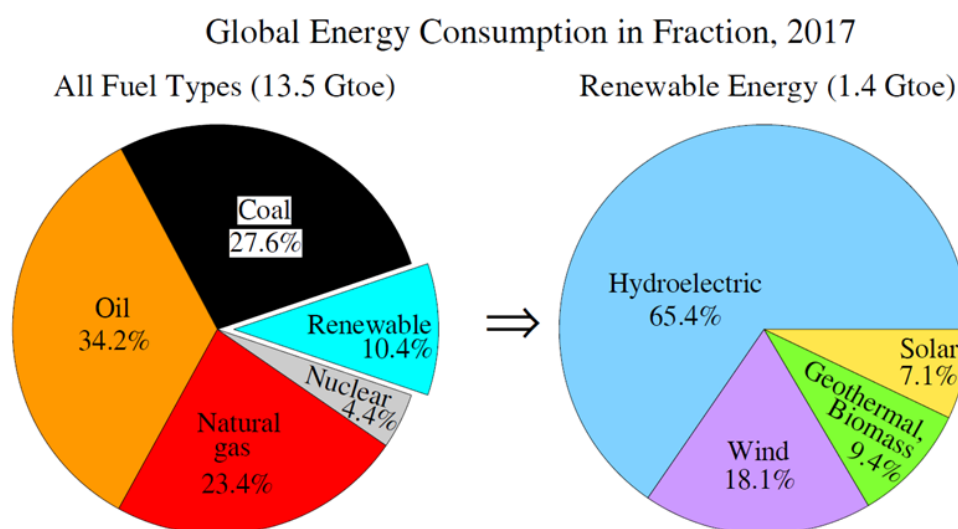


Figure 1.8. Global energy consumption in fraction (2017).

<http://www.columbia.edu/~mhs119/EnergyConsump/>.

Solar cell is a device which can generate clean energy at comparatively low cost with unlimited supply. Three different generations of solar cells can be distinguished. The first generation is based on crystalline silicon solar cells reaching power conversion efficiencies (PCEs) up to 25%. However it requires high temperature production leading to high cost installation[35]. The

second generation based on PV thin films (CdTe, CIGs and GaAs) with PCEs up to 26% [36] are still expensive and possess less Earth abundant materials than the next generation based on organic solar cells, quantum dot solar cells and perovskite solar cells. This third generation reduces the production cost using abundant Earth elements and less expensive production techniques.

Dye-sensitized solar cells (DSSCs) were first reported in 1991 by O'Regan and Grätzel [37] reaching PCEs up to 13% and more important opening the doors to low-cost and easy roll-to-roll fabrication solar cells technology. Based on this work, Dye was later replaced by perovskite materials considered as a promising photovoltaic technology thanks to their excellent properties such as low effective mass, high carrier mobility- lifetime product, weak exciton binding energy at room temperature, unusually high defect tolerance and low trap density[38–41]. Within a period of few years, the devices power conversion efficiencies (PCEs) were drastically increased from low PCEs of 3.8% to current certified values greater than 22%.

National Renewable Energy Laboratory (NREL) photovoltaic efficiency chart illustrated in Figure 1.9 demonstrates the meteoric and incredibly impressive rise of perovskite based solar cells over the last few years compared to emergent photovoltaic research technology, and also traditional photovoltaics thin-film. This impressive rise reaches certified values greater than 22% making it comparable to Cadmium Telluride.

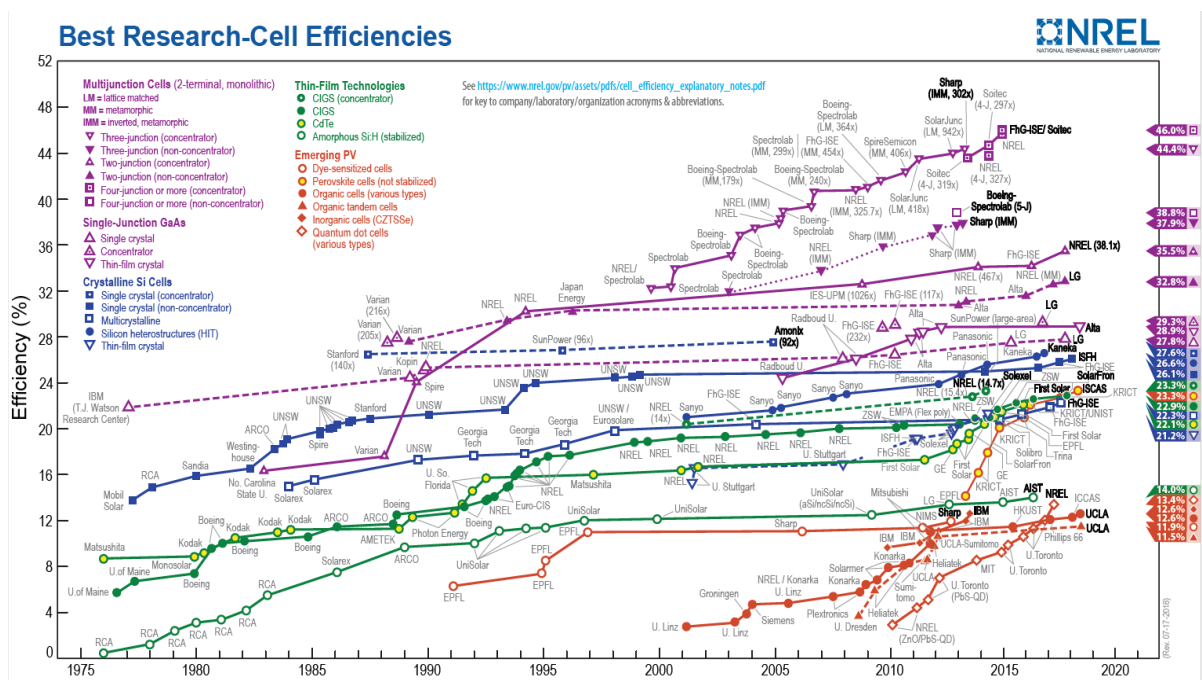


Figure 1.9. NREL photovoltaic efficiency chart extracted from. <https://www.nrel.gov/pv/>.

On the other hand, the development of traditional silicon solar cell is the main product today and the cost is linked to the silicon processing technology. Meanwhile, the emergence of organic-inorganic perovskites offer promising routes for the development of new solar cells with high efficiency and reduced cost. Despite such unprecedented progress, there are still many drawbacks to overcome before transfer to volume production. Besides the good efficiencies, the toxicity of lead and the sensitivity of the perovskite solar cells to the atmosphere during their operation and during their fabrication have been identified as two of the major obstacles to transfer to large-scale PSCs (Perovskite Solar Cells) production [42–43].

The moisture during the perovskite solar cells fabrication dramatically affects the crystallization behavior as well as the degradation of organic-inorganic hybrid perovskites crystals. To address this issue, intensive recent research efforts have been devoted to develop consistent methods for the fabrication of solar cells in air conditions.

Tai *et al.* [44] reported efficient and stable perovskite solar cells fabricated under humid conditions (RH ~ 70%) produced on mesoporous TiO₂ and using Pb(SCN)₂ precursor with power conversion efficiencies values (PCEs) up to 15% (Figure 1.10).

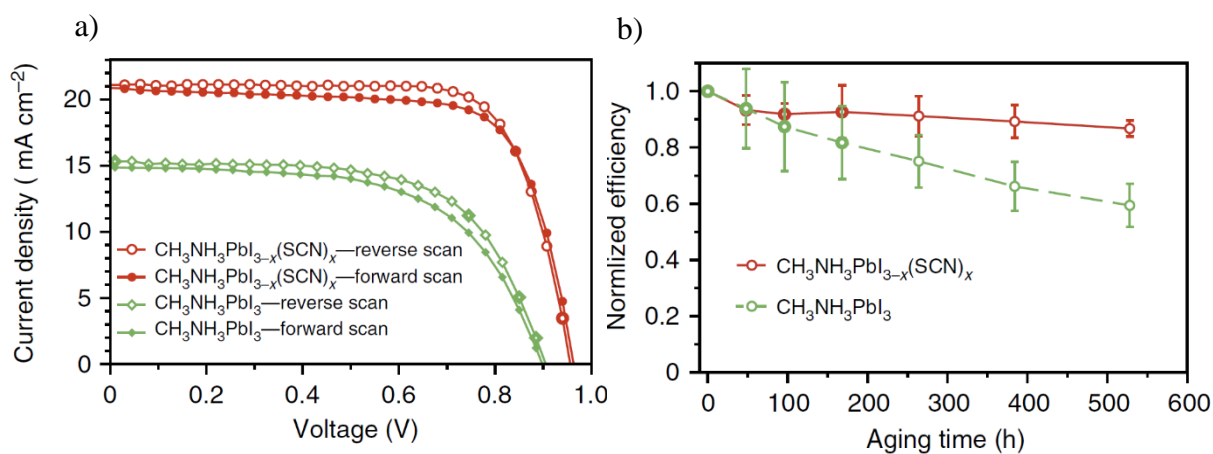


Figure 1.10. a) J - V curves of $\text{CH}_3\text{NH}_3\text{PbI}_{3-x}(\text{SCN})_x$ ($\text{Pb}(\text{SCN})_2$ -derived) and $\text{CH}_3\text{NH}_3\text{PbI}_3$ (PbI_2 -derived)-based solar cells prepared in ambient air. b) Evolution of the PCEs of $\text{CH}_3\text{NH}_3\text{PbI}_{3-x}(\text{SCN})_x$ and $\text{CH}_3\text{NH}_3\text{PbI}_3$ -based solar cells upon aging in air without encapsulation reported by Tai *et al.*[44].

Troughton *et al.*[45] have developed an anti-solvent method during perovskite spin-coating able to capture the moisture and protect the perovskite layer. They obtained efficient solar cells with

PCEs up to 10% (area 13.5 cm^2) fabricated in 75%RH ambient conditions as illustrated in Figure 1.11.

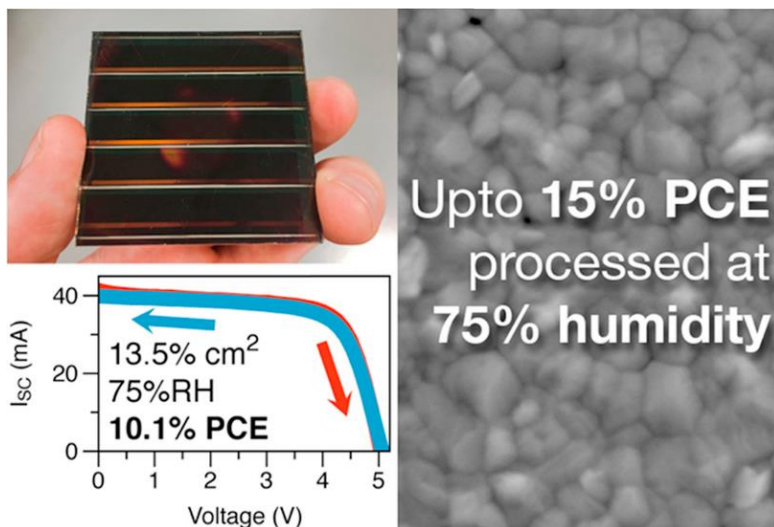


Figure 1.11. Device photograph, I_{sc} - V characteristics and perovskite micro-image of perovskite thin films deposited under air conditions with 75% RH employing the humidity-resistant ethyl acetate anti-solvent method reported by Troughton *et al.* [45].

Moreover, Kavadiya *et al.* [46] reported a novel technique of electro spray deposition to form highly smooth and water resistant perovskite layers at ambient humidity conditions reaching efficiencies up to 12% with long-term stability (Figure 1.12).

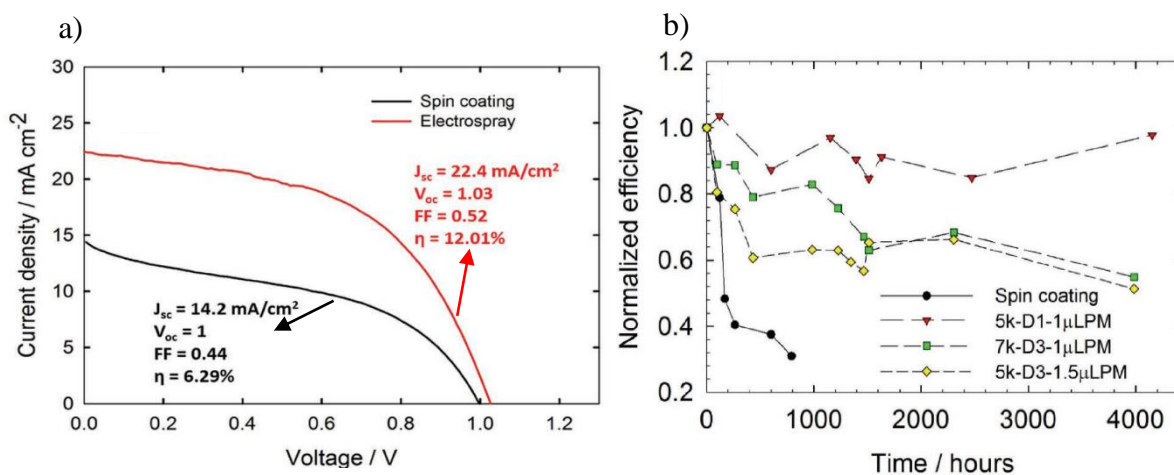


Figure 1.12. I - V characteristics of the two devices fabricated with the two different techniques: spin coating (PCE $\sim 6.29\%$) and electro spray (PCE $\sim 12.01\%$). Time evolution of the efficiency of the perovskite solar cells fabricated using electro spray at various conditions [46].

1.3.3 LEDs

Hybrid perovskite materials exhibit tunable band gap, high photoluminescence quantum yield (PLQY) and good charges mobilities [47–48, 16–19] making them also extremely attractive for electroluminescence (EL) applications.

In 2014, Tvingstedt *et al.* [49] reported for the first time the use of 2D-layered perovskites on LEDs; however, only low operating temperatures hindered its use in real life.

Perovskite based LEDs (PeLEDs) operating at room temperature was reported for the first time by Schmidt *et al.* [50–51] by using 3D perovskites. Later, Tanetaling *et al.*[52] reported the operation of multicolor (NIR, red and green) metal-halide perovskite based LEDs (PeLEDs) at room temperature. Tan *et al.*[53] have reported bright, near-infrared (NIR) and green LED using the 3D perovskites MAPbX₃ (X = Br or I) as emitter with EQE up to 0.7%.

External Quantum Efficiency (EQE) is the ratio of the number of photons emitted from the LED to the number of electrons passing through the device which determine how efficiently the device converts electrons to photons and allows them to escape (Equation 1.2).

$$EQE = \frac{\text{electrons/sec}}{\text{photons/sec}} \quad (\text{Equation 1.2})$$

From then on, considerable advances have been achieved in perovskite based LEDs. Recently, green- and near-infrared-emitting PeLEDs have reach EQEs values up to 10% [54] whereas the demonstration of color-stable and efficient blue 3D PeLEDs remains challenging.

Recent progress on the stability devices have been done by using 2D perovskites. Quasi-2D blue PeLEDs (Figure 1.13) have been reported providing stable color-stable blue-emitting perovskite thin film with record high bright luminance and high EQE opening promising routes for the development of PeLEDs[55].

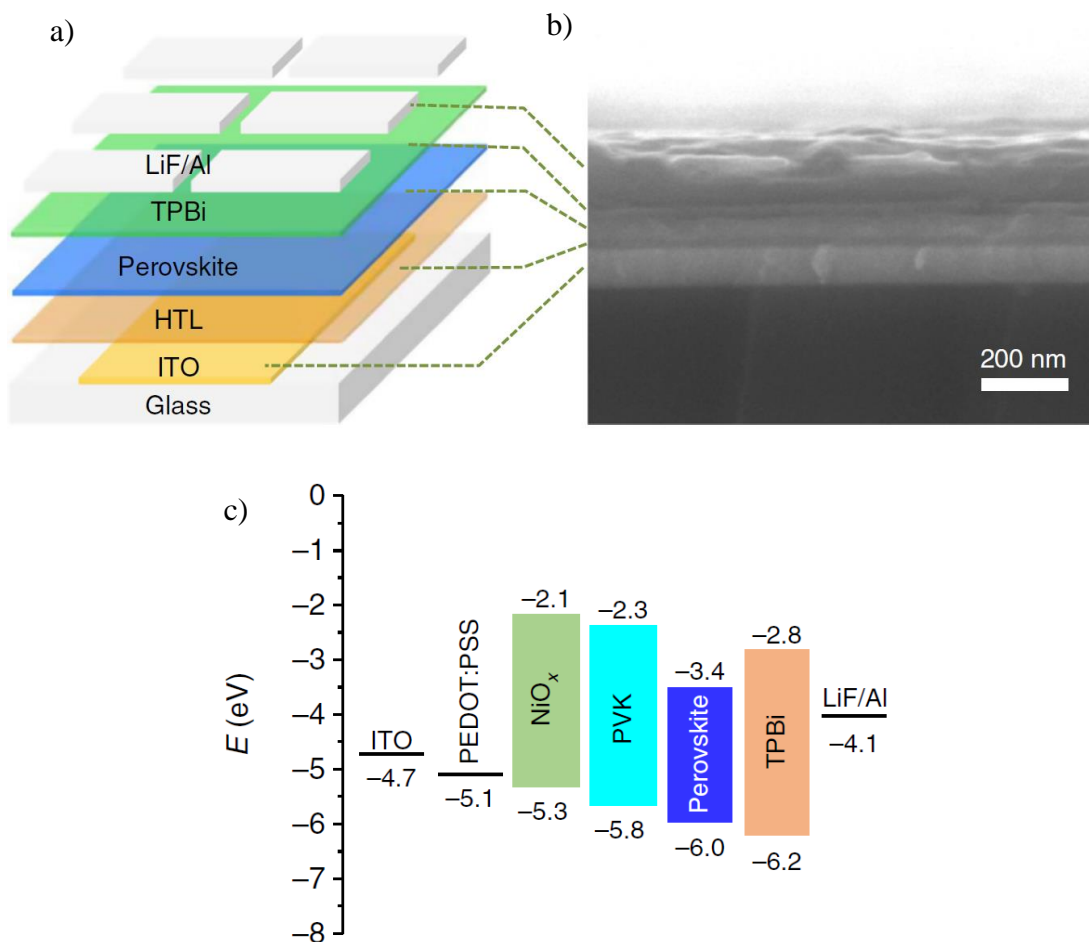


Figure 1.13. Perovskite based light-emitting diodes reported by Xing et al. [55]. a) Device structure. b) device cross-sectional SEM image and c) energy levels alignments of the PeLEDs, showing conduction and valence-band levels with respect to vacuum.

1.3.4 Radiation detectors

The large mobilities and carrier lifetimes in hybrid perovskite single crystals and the high atomic numbers of Pb, I and Br [16–19] make them ideal for radiation detection widely used in the fields of security, defense, medical imaging, industrial material inspection, nuclear power stations and scientific research.

MAPbBr₃ single-crystals have been used in X-ray detectors (Figure 1.14) highlighting high sensitivity and a lowest detectable dose rate [25] meeting the practical needs of medical diagnostics [56].

On the other hand, inorganic perovskites CsPbBr₃ have demonstrated a great potential for detection applications (long-term stability, easy scale-up, low cost, large bandgap, high Z

compound...). They are considered as viable candidates for next generation room temperature radiation detectors. Promising results have been reported by He *et al.* [27] by using CsPbBr₃ planar detectors considered as the major step toward the fabrication of perovskite radiation detectors.

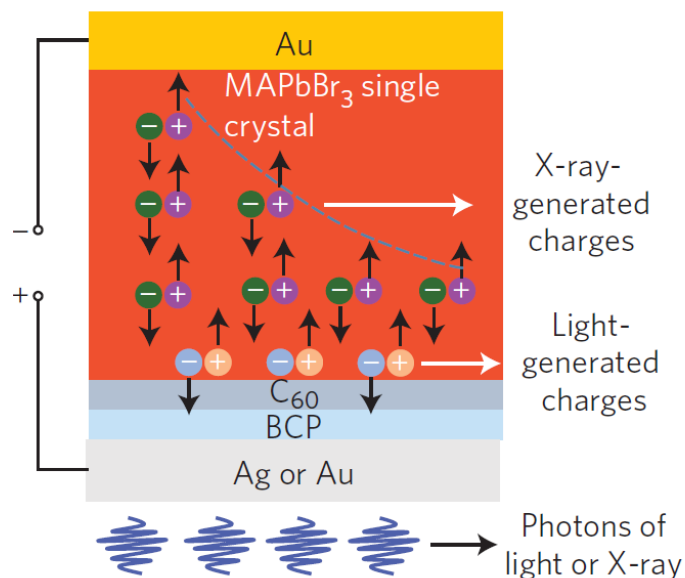


Figure 1.14. Structure of perovskite based X-ray detector previously reported by Wei *et al.*[25].

1.3.5 Optically pumped lasers

Organic-inorganic lead halide perovskites have recently emerged as promising material for tunable semiconductor lasers. However its demonstration has remained challenging so far. Some approaches have demonstrated lasing action in methylammonium lead iodide (Figure 1.15) at room temperature under continuous-wave optical pumping, in ambient air environment. These results represent a promising step toward the fabrication of perovskite laser diodes [57].

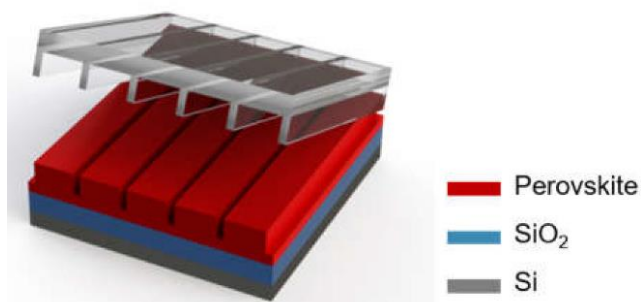


Figure 1.15. Fabrication scheme and of surface-emitting perovskite based lasers reported by Li *et al.*[57].

In this chapter, we have presented the state of art of hybrid organic-inorganic perovskite materials by briefly discussing the origin, material properties and the major applications developed with this emerging material. We mainly focused on the description and challenges related to FETs and solar cells which are the two main applications in this thesis. The fabrication and characterization techniques used will be introduced in the next chapter.

1.4 References

- [1] L. Cavalcante, V. Marques, J. Sczancoski, M. Escote, M. Joya, J.A. Varela, M. Santos, P. Pizani, E. Longo, Synthesis, structural refinement and optical behavior of CaTiO₃ powders: A comparative study of processing in different furnaces, *Chemical Engineering Journal*. 143 (2008) 299–307.
- [2] A.R. Chakhmouradian, P.M. Woodward, *Celebrating 175 years of perovskite research: a tribute to Roger H. Mitchell*, Springer, 2014.
- [3] S. Sasaki, C.T. Prewitt, J.D. Bass, W. Schulze, Orthorhombic perovskite CaTiO₃ and CdTiO₃: structure and space group, *Acta Crystallographica Section C*. 43 (1987) 1668–1674.
- [4] D.B. Mitzi, C. Feild, W. Harrison, A. Guloy, Conducting tin halides with a layered organic-based perovskite structure, *Nature*. 369 (1994) 467.
- [5] C. Li, X. Lu, W. Ding, L. Feng, Y. Gao, Z. Guo, Formability of ABX₃ (X= F, Cl, Br, I) Halide Perovskites, *Acta Crystallographica Section B: Structural Science*. 64 (2008) 702–707.
- [6] A.R. bin M. Yusoff, M.K. Nazeeruddin, Organohalide Lead Perovskites for Photovoltaic Applications., *The Journal of Physical Chemistry Letters*. 7 5 (2016) 851–66.
- [7] P. Gao, M. Grätzel, M.K. Nazeeruddin, Organohalide lead perovskites for photovoltaic applications, *Energy & Environmental Science*. 7 (2014) 2448–2463.
- [8] M.A. Peña, J.L.G. Fierro, Chemical Structures and Performance of Perovskite Oxides, *Chemical Reviews*. 101 (2001) 1981–2018.
- [9] T. Ishihara, Structure and properties of perovskite oxides, in: *Perovskite Oxide for Solid Oxide Fuel Cells*, Springer, 2009: pp. 1–16.
- [10] J. Zhu, H. Li, L. Zhong, P. Xiao, X. Xu, X. Yang, Z. Zhao, J. Li, Perovskite Oxides: Preparation, Characterizations, and Applications in Heterogeneous Catalysis, *ACS Catalysis*. 4 (2014) 2917–2940.
- [11] M. Kubicek, A.H. Bork, J.L. Rupp, Perovskite oxides—a review on a versatile material class for solar-to-fuel conversion processes, *Journal of Materials Chemistry A*. 5 (2017) 11983–12000.
- [12] A. Salau, Fundamental absorption edge in PbI₂: KI alloys, *Solar Energy Materials*. 2 (1980) 327–332.
- [13] A. Kojima, K. Teshima, Y. Shirai, T. Miyasaka, Organometal halide perovskites as visible-light sensitizers for photovoltaic cells, *Journal of the American Chemical Society*. 131 (2009) 6050–6051.
- [14] N.J. Jeon, J.H. Noh, Y.C. Kim, W.S. Yang, S. Ryu, S.I. Seok, Solvent engineering for high-performance inorganic–organic hybrid perovskite solar cells, *Nature Materials*. 13 (2014) 897.
- [15] M.A. Green, Y. Hishikawa, W. Warta, E.D. Dunlop, D.H. Levi, J. Hohl-Ebinger, A.W. Ho-Baillie, Solar cell efficiency tables (version 50), *Progress in Photovoltaics*. 25 (2017).
- [16] M. Saliba, T. Matsui, J.-Y. Seo, K. Domanski, J.-P. Correa-Baena, M.K. Nazeeruddin, S.M. Zakeeruddin, W. Tress, A. Abate, A. Hagfeldt, others, Cesium-containing triple cation perovskite solar cells: improved stability, reproducibility and high efficiency, *Energy & Environmental Science*. 9 (2016) 1989–1997.
- [17] McGehee, M. D. Materials science: Fast-track solar cells. *Nature* 501, 323–325 (2013).
Fan, P. et al. High-performance perovskite CH₃NH₃PbI₃ thin films for solar cells prepared by single-source physical vapour deposition. *Sci. Rep.* 6, 29910, (2016).
- [18] Nie W. et al. High-efficiency solution-processed perovskite solar cells with millimeter-scale grains. *Science* 347, 522–525 (2015).
- [19] W. Chen et al. Efficient and stable large-area perovskite solar cells with inorganic charge extraction layers. *Science* 35, 944–948 (2015).
- [20] S.P. Senanayak, B. Yang, T.H. Thomas, N. Giesbrecht, W. Huang, E. Gann, B. Nair, K. Goedel, S. Guha, X. Moya, others, Understanding charge transport in lead iodide perovskite thin-film field-effect transistors, *Science Advances*. 3 (2017) e1601935.
- [21] X.Y. Chin, D. Cortecchia, J. Yin, A. Bruno, C. Soci, Lead iodide perovskite light-emitting field-effect transistor, *Nature Communications*. 6 (2015) 7383.

- [22] Y. Mei, C. Zhang, Z. Vardeny, O. Jurchescu, Electrostatic gating of hybrid halide perovskite field-effect transistors: balanced ambipolar transport at room-temperature, *MRS Communications*. 5 (2015) 297–301.
- [23] F. Li, C. Ma, H. Wang, W. Hu, W. Yu, A.D. Sheikh, T. Wu, Ambipolar solution-processed hybrid perovskite phototransistors, *Nature Communications*. 6 (2015) 8238.
- [24] C.R. Kagan, D.B. Mitzi, C.D. Dimitrakopoulos, Organic-Inorganic Hybrid Materials as Semiconducting Channels in Thin-Film Field-Effect Transistors, *Science*. 286 (1999) 945–947. doi:10.1126/science.286.5441.945.
- [25] H. Wei, Y. Fang, P. Mulligan, W. Chuirazzi, H.-H. Fang, C. Wang, B.R. Ecker, Y. Gao, M.A. Loi, L. Cao, others, Sensitive X-ray detectors made of methylammonium lead tribromide perovskite single crystals, *Nature Photonics*. 10 (2016) 333.
- [26] Y. He, L. Matei, H.J. Jung, K.M. McCall, M. Chen, C.C. Stoumpos, Z. Liu, J.A. Peters, D.Y. Chung, B.W. Wessels, others, High spectral resolution of gamma-rays at room temperature by perovskite CsPbBr₃ single crystals, *Nature Communications*. 9 (2018) 1609.
- [27] Y. He, L. Matei, H.J. Jung, K.M. McCall, M. Chen, C.C. Stoumpos, Z. Liu, J.A. Peters, D.Y. Chung, B.W. Wessels, others, High spectral resolution of gamma-rays at room temperature by perovskite CsPbBr₃ single crystals, *Nature Communications*. 9 (2018) 1609.
- [28] Y. Ling, Z. Yuan, Y. Tian, X. Wang, J. Wang, Y. Xin, K. Hanson, B. Ma, H. Gao, Bright Light-Emitting Diodes Based on Organometal Halide Perovskite Nanoplatelets, *Advanced Materials* (Deerfield Beach, Fla.). 28 (2015).
- [29] S.A. Veldhuis, P. Boix, N. Yantara, M. Li, T.C. Sum, N. Mathews, S. Mhaisalkar, Perovskite Materials for Light-Emitting Diodes and Lasers, *Advanced Materials*. 28 (2016).
- [30] F. Koppens, T. Mueller, P. Avouris, A. Ferrari, M. Vitiello, M. Polini, Photodetectors based on graphene, other two-dimensional materials and hybrid systems, *Nature Nanotechnology*. 9 (2014) 780.
- [31] X. Liu, L. Gu, Q. Zhang, J. Wu, Y. Long, Z. Fan, All-printable band-edge modulated ZnO nanowire photodetectors with ultra-high detectivity, *Nature Communications*. 5 (2014) 4007.
- [32] S. Park, S.J. Kim, J.H. Nam, G. Pitner, T.H. Lee, A.L. Ayzner, H. Wang, S.W. Fong, M. Vosgueritchian, Y.J. Park, others, Significant Enhancement of Infrared Photodetector Sensitivity Using a Semiconducting Single-Walled Carbon Nanotube/C60 Phototransistor, *Advanced Materials*. 27 (2015) 759–765.
- [33] H. Yu, Z. Bao, J.H. Oh, High-performance phototransistors based on single-crystalline n-channel organic nanowires and photogenerated charge-carrier behaviors, *Advanced Functional Materials*. 23 (2013) 629–639.
- [34] L.M. Herz, Charge-carrier mobilities in metal halide perovskites: Fundamental mechanisms and limits, *ACS Energy Letters*. 2 (2017) 1539–1548.
- [35] K. Masuko, M. Shigematsu, T. Hashiguchi, D. Fujishima, M. Kai, N. Yoshimura, T. Yamaguchi, Y. Ichihashi, T. Mishima, N. Matsubara, others, Achievement of more than 25% conversion efficiency with crystalline silicon heterojunction solar cell, *IEEE Journal of Photovoltaics*. 4 (2014) 1433–1435.
- [36] A. Shah, P. Torres, R. Tscharnner, N. Wyrsh, H. Keppner, Photovoltaic technology: the case for thin-film solar cells, *Science*. 285 (1999) 692–698.
- [37] B. O’regan, M. Grätzel, A low-cost, high-efficiency solar cell based on dye-sensitized colloidal TiO₂ films, *Nature*. 353 (1991) 737.
- [38] C. Wehrenfennig, G.E. Eperon, M.B. Johnston, H.J. Snaith, L.M. Herz, High charge carrier mobilities and lifetimes in organolead trihalide perovskites, *Advanced Materials*. 26 (2014) 1584–1589.
- [39] M. De Bastiani, G. Dell’Erba, M. Gandini, V. D’Innocenzo, S. Neutzner, A.R.S. Kandada, G. Grancini, M. Binda, M. Prato, J.M. Ball, others, Ion migration and the role of preconditioning cycles in the stabilization of the J–V characteristics of inverted hybrid perovskite solar cells, *Advanced Energy Materials*. 6 (2016) 1501453.
- [40] J. Ma, L.-W. Wang, The nature of electron mobility in hybrid perovskite CH₃NH₃PbI₃, *Nano Letters*. 17 (2017) 3646–3654.
- [41] T. Zhao, W. Shi, J. Xi, D. Wang, Z. Shuai, Intrinsic and extrinsic charge transport in CH₃NH₃PbI₃ perovskites predicted from first-principles, *Scientific Reports*. 6 (2016) 19968.

- [42] M.K. Gangishetty, R.W. Scott, T.L. Kelly, Effect of relative humidity on crystal growth, device performance and hysteresis in planar heterojunction perovskite solar cells, *Nanoscale*. 8 (2016) 6300–6307.
- [43] F. Hao, C.C. Stoumpos, D.H. Cao, R.P. Chang, M.G. Kanatzidis, Lead-free solid-state organic–inorganic halide perovskite solar cells, *Nature Photonics*. 8 (2014) 489.
- [44] Q. Tai, P. You, H. Sang, Z. Liu, C. Hu, H.L. Chan, F. Yan, Efficient and stable perovskite solar cells prepared in ambient air irrespective of the humidity, *Nature Communications*. 7 (2016) 11105.
- [45] J. Troughton, K. Hooper, T.M. Watson, Humidity resistant fabrication of CH₃NH₃PbI₃ perovskite solar cells and modules, *Nano Energy*. 39 (2017) 60–68.
- [46] S. Kavadiya, D.M. Niedzwiedzki, S. Huang, P. Biswas, Electro-spray-Assisted Fabrication of Moisture-Resistant and Highly Stable Perovskite Solar Cells at Ambient Conditions, *Advanced Energy Materials*. 7 (2017) 1700210.
- [47] Chilvery, Ashwith et al. A Perspective on the Recent Progress in Solution-Processed Methods for Highly Efficient Perovskite Solar Cells. *Science and Technology of Advanced Materials* 17.1, 650–658 (2016).
- [48] McGehee, M. D. Materials science: Fast-track solar cells. *Nature* 501, 323–325 (2013).
Fan, P. et al. High-performance perovskite CH₃NH₃PbI₃ thin films for solar cells prepared by single-source physical vapour deposition. *Sci. Rep.* 6, 29910, (2016).
- [49] K. Tvingstedt, O. Malinkiewicz, A. Baumann, C. Deibel, H.J. Snaith, V. Dyakonov, H.J. Bolink, Radiative efficiency of lead iodide based perovskite solar cells, *Scientific Reports*. 4 (2014) 6071.
- [50] K. Chondroudis, D.B. Mitzi, Electroluminescence from an organic- inorganic perovskite incorporating a quaterthiophene dye within lead halide perovskite layers, *Chemistry of Materials*. 11 (1999) 3028–3030.
- [51] T. Hattori, T. Taira, M. Era, T. Tsutsui, S. Saito, Highly efficient electroluminescence from a heterostructure device combined with emissive layered-perovskite and an electron-transporting organic compound, *Chemical Physics Letters*. 254 (1996) 103–108.
- [52] L.C. Schmidt, A. Pertegás, S. González-Carrero, O. Malinkiewicz, S. Agouram, G. Mínguez Espallargas, H.J. Bolink, R.E. Galian, J. Pérez-Prieto, Nontemplate synthesis of CH₃NH₃PbBr₃ perovskite nanoparticles, *Journal of the American Chemical Society*. 136 (2014) 850–853.
- [53] Z.-K. Tan, R.S. Moghaddam, M.L. Lai, P. Docampo, R. Higler, F. Deschler, M. Price, A. Sadhanala, L.M. Pazos, D. Credgington, others, Bright light-emitting diodes based on organometal halide perovskite, *Nature Nanotechnology*. 9 (2014) 687–692.
- [54] Z. Xiao, R.A. Kerner, L. Zhao, N.L. Tran, K.M. Lee, T.-W. Koh, G.D. Scholes, B.P. Rand, Efficient perovskite light-emitting diodes featuring nanometre-sized crystallites, *Nature Photonics*. 11 (2017) 108.
- [55] J. Xing, Y. Zhao, M. Askerka, L.N. Quan, X. Gong, W. Zhao, J. Zhao, H. Tan, G. Long, L. Gao, others, Color-stable highly luminescent sky-blue perovskite light-emitting diodes, *Nature Communications*. 9 (2018) 3541.
- [56] D.R. Shearer, M. Bopaiah, Dose rate limitations of integrating survey meters for diagnostic x-ray surveys. *Health Physics*. 79 (2000) S20–1.
- [57] Z. Li, J. Moon, A. Gharajeh, R. Haroldson, R. Hawkins, W. Hu, A. Zakhidov, Q. Gu, Room-temperature continuous-wave operation of organometal halide perovskite lasers, *ArXiv Preprint ArXiv:1805.01092*. (2018).

CHAPTER 2. FABRICATION AND CHARACTERIZATION

This section describes the detailed information about the fabrication and characterization techniques used in this thesis for the development of perovskite based solar cells and field effect transistors.

It should be noted that the vast majority of the processes were done under a controlled atmosphere (Glove Box -P ~ 3.8 mBar, H₂O < 0.1 ppm, O₂ ~ 0.5 ppm).

2.1 Fabrication techniques

2.1.1 Solar cells

2.1.1.1 Perovskite preparation

For the fabrication of perovskite solar cells, we used a commercial perovskite precursor ink (Ossila, I101) composed by mixture of methyl ammonium iodide (MAI) and lead chloride (PbCl) with a molar ratio of 3:1 dissolved in dimethyl formamide (Table 2.1). The final product is a methylammonium lead iodide perovskite with trace amounts of chlorine given by the formula CH₃NH₃PbI_{3-x}Cl_x (Figure 2.1). This solution was preheated at 70°C during 2 hours previously to its deposition.

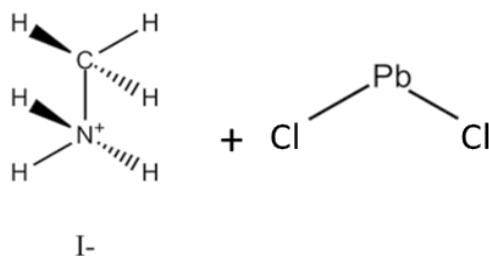


Figure 2.1. Combination of materials used for the preparation of methylammonium lead iodide perovskite with trace amounts of chlorine: MAI+PbCl₂.

Precursor Materials	Methyl Ammonium Iodide (99.9%) Lead Chloride (99.999%)
Precursor Ratio	3:1
Solvent	Dimethyl Formamide (99.8%)

Table 2.1. Precursor materials, ratio and solvent for the preparation of methylammonium lead iodide perovskite.

For the fabrication of perovskite solar cells under high relative humidity, we used a thermal technique for perovskite deposition as illustrated in Figure 2.2.

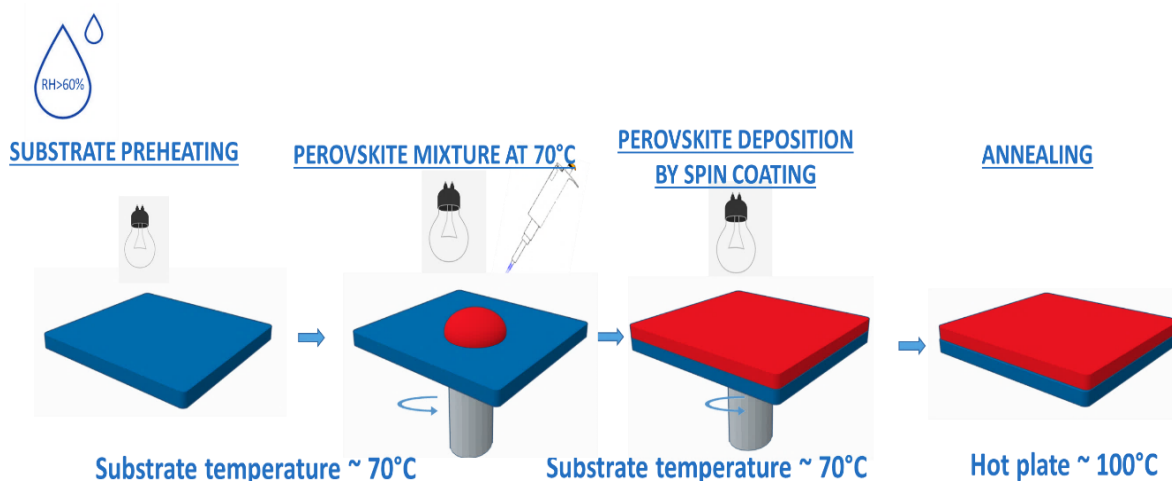


Figure 2.2. Processing scheme for perovskite thin-films deposition under humid conditions.

This technique consists in setting up an infrared lamp on top of the spin coater and hot plate to continuously heat the samples ($T \sim 70^\circ\text{C}$) in order to reduce the moisture in the local environment. The substrates are preheated during 5 minutes under the lamp, then transferred rapidly from the hot plate to the spin-coater where the rotation starts at 3000 rpm. Then, 100 μL of perovskite solution (previously heated at 70°C during 2 hours) is dynamically dispensed on the spinning substrates (time duration is 30 seconds). Finally, the substrates are placed on the hot plate at 100°C during 90 minutes to fully convert the perovskite precursor into the perovskite films.

On the other hand, the technique used in this thesis to deposit perovskite under nitrogen atmosphere conditions (Glove Box -P~3.8mBar, H₂O< 0.1ppm, O₂~0.5ppm), known as casting method, is illustrated in Figure 2.3.

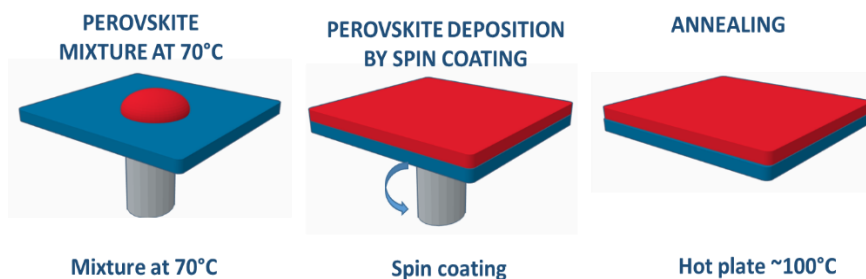


Figure 2.3. Processing scheme for perovskite thin-films deposition under nitrogen atmosphere conditions.

The perovskite solution (previously heated at 70°C during 2 hours) is deposited onto the substrates at room temperature by spin coating for 30 seconds at 3000 rpm. Then, the substrates are placed on the hot plate at 100 °C during 90 minutes.

2.1.1.2 Solar cells fabrication

The processing scheme used in this study to fabricate perovskite solar cells is illustrated in Figure 2.4.

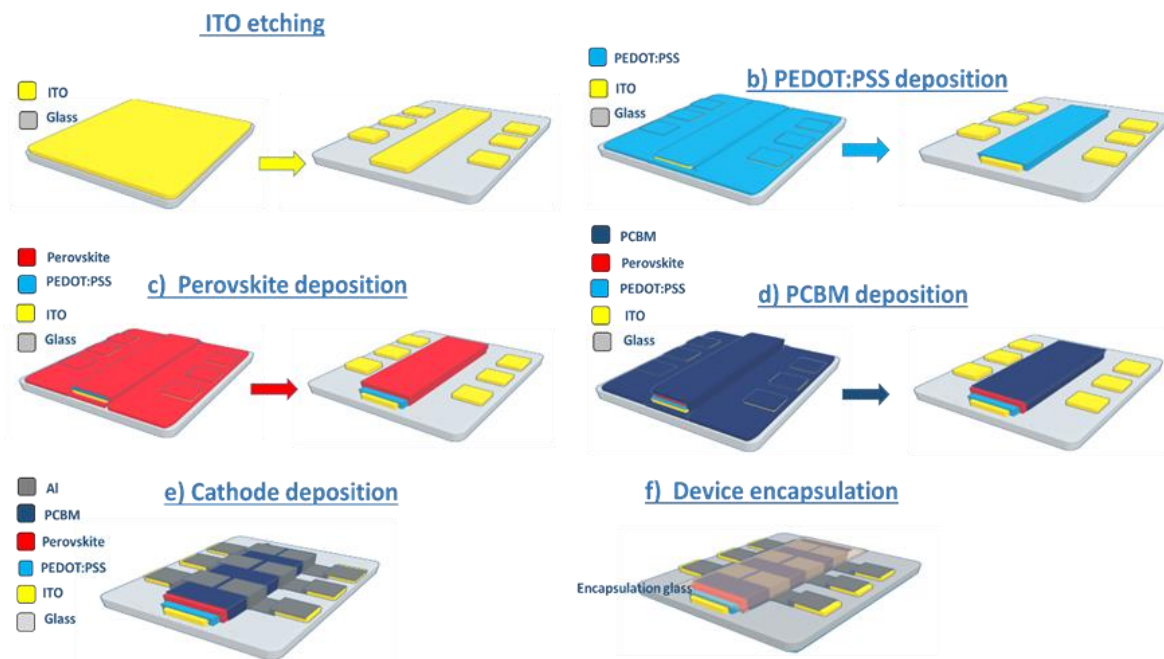


Figure 2.4. Processing scheme for perovskite solar cells fabrication used in this study.

The fabrication of perovskite based solar cells is described in the following steps:

a) ITO etching

The substrates were indium tin oxide (ITO) coated glasses (SOLEMS, thickness ~ 400 nm, sheet resistance $\sim 12 \Omega\text{sq}^{-1}$). This material has been extensively used as anode in perovskite solar cells thanks to its outstanding properties such as high electrical conductivity, high work function and high optical transmittance in visible area[1,2].

To proceed with the fabrication of solar cells, ITO-substrates were first partially etched by photolithography process (Figure 2.5).

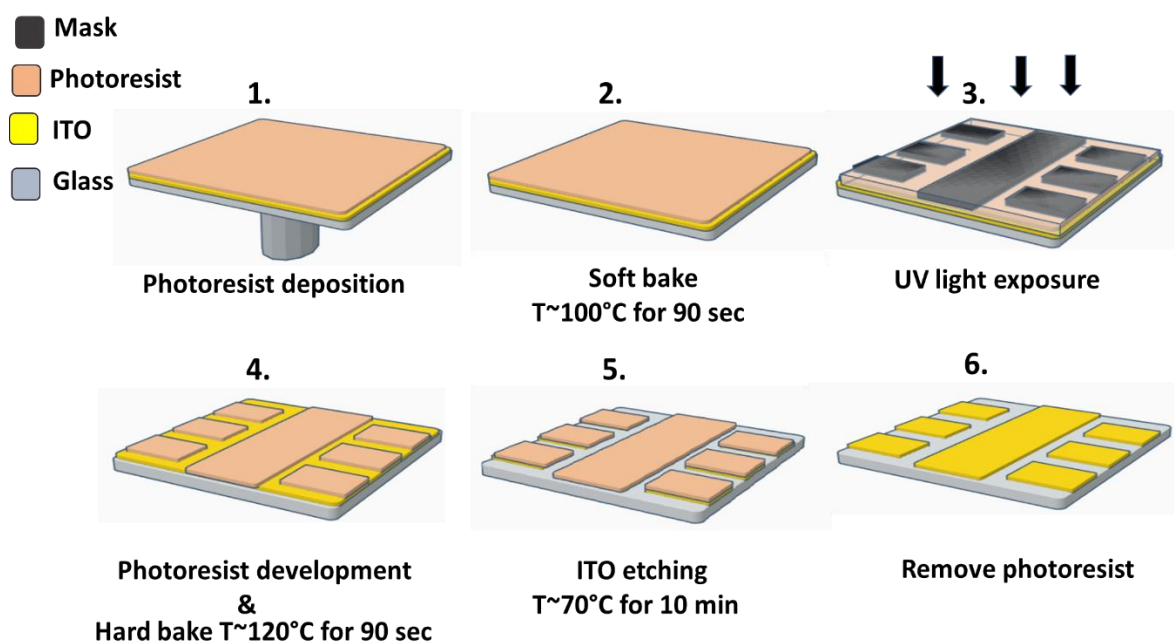


Figure 2.5. Photolithography steps for ITO-coated films

First, we deposited the S1818 photoresist (MicroChem S1818 Photoresist) by spin coating method using a speed of 4000 rpm, acceleration of 2000 rpm/s for 60 seconds to obtain $1.8 \mu\text{m}$ thick layer. The photo resist-coated film is then prebaked to drive off excess solvent at 100°C for 90 seconds on a hotplate, also known as soft bake step. The next step is the sample exposure to UV light with the desired mask to define the anode patterns. This exposure causes a chemical change (polymerization) allowing to remove the exposed photoresist by a special solution, called "developer"(MF CD26 Shipley). S1818 is a positive photoresist which becomes soluble in the developer for the UV exposed region. Then, samples are heated at 120°C for 90 seconds (also known as hard bake step), to improve the adhesion and hardens the

photoresist. Then, we used wet ITO etching technique to define anode contacts. Finally, we removed the S1818 photoresist by cleaning the substrates with acetone. After photolithography process, the patterned ITO substrates were sonicated for 10 minutes in 1% Hellmanex (at ~ 70°C) and rinsed in boiling deionized water, followed by an acetone and isopropyl alcohol sonication during 20 minutes respectively. Then, the substrates were subsequently exposed to UV-ozone treatment during 10 minutes in order to clean the ITO surface before the PEDOT: PSS deposition.

b) PEDOT: PSS deposition

After the UV – ozone treatment, poly 3, 4 –ethylenedioxythiophene: poly styrenesulfonic acid (Ossila, PEDOT: PSS 4083, thickness ~ 40nm) was deposited onto the ITO/glass substrates by spin coating for 60 seconds at 1500 rpm. Then, the substrates were dried at 120 °C during 20 minutes after wiping the cathode strip with a micro-precision cleanroom swab dampened with deionized water (Figure 2.4b).

c) Perovskite deposition

Perovskite films were deposited under air conditions or in nitrogen atmosphere according to details given in section 2.1.1.1.

After perovskite deposition, the cathode strip was wiped with a dry micro-precision cleanroom swab (Figure 2.4c).

d) PCBM deposition

To this step, the deposition parameters are the same for the air process and the glove box process. The perovskite films were covered by spin coating at 1000 rpm for 30 seconds with Phenyl-C₇₀-butyric acid methyl ester (PC₇₀BM, Ossila, thickness ~ 100 nm) in the glove box. Then, PCBM films were wiped with a micro-precision cleanroom swab dampened with chlorobenzene to define the cathode strip (Figure 2.4d).

e) Cathode deposition

Finally, 150 nm of aluminum (Al) contact electrode was deposited on the PC₇₀BM layer using a shadow mask (Figure 2.4e). The active area, which currently varies between 0.08 and 0.1 cm² due to uncontrolled processing misalignments, is defined by the ITO and Al contacts.

Thermal Evaporation under high vacuum ($\sim 10^{-7}$ Torr) was used to deposit aluminum electrodes. Briefly, this technique is performed by heating a material in a vacuum chamber until its surface atoms have sufficient energy to evaporate from the surface and then condensate at the substrate surface (Figure 2.6).

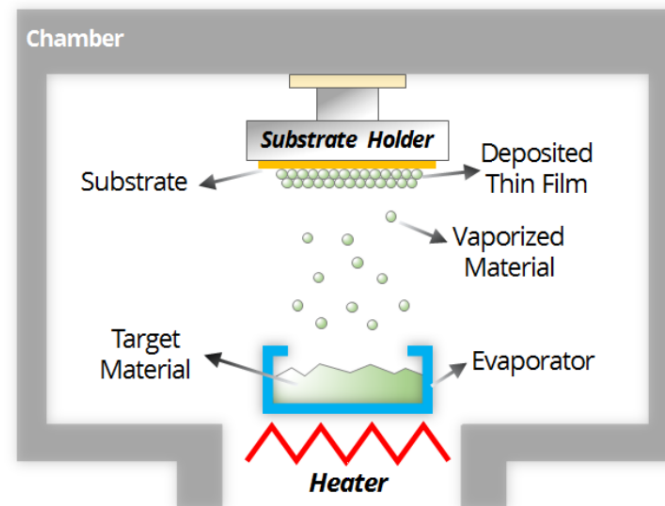


Figure 2.6. Processing scheme for thermal evaporation [30].

f) Device encapsulation

All devices were encapsulated to minimize the air degradation using a resin (E132 PV & LED Encapsulation Epoxy, Ossila) and covered with a soda-lime glass (Figure 2.4f).

2.1.1.3 Working principle

The working principle of a solar cell is based on the creation of voltage and electric current in a material submitted to light exposure: this effect is known as photovoltaic effect. The external and internal structure of the solar cell device are shown in the Figure 2.7a and Figure 2.7b respectively. Basically, the internal structure of solar cells is a p-n junction diode.

The operation of a photovoltaic cell follows different steps:

- i) The light is absorbed on the active layer and electron-hole pairs are generated.
- ii) Photo-carriers are separated by the internal electric field and create the internal current.
- iii) Extraction of those carriers to an external circuit is obtained by the contact electrodes.

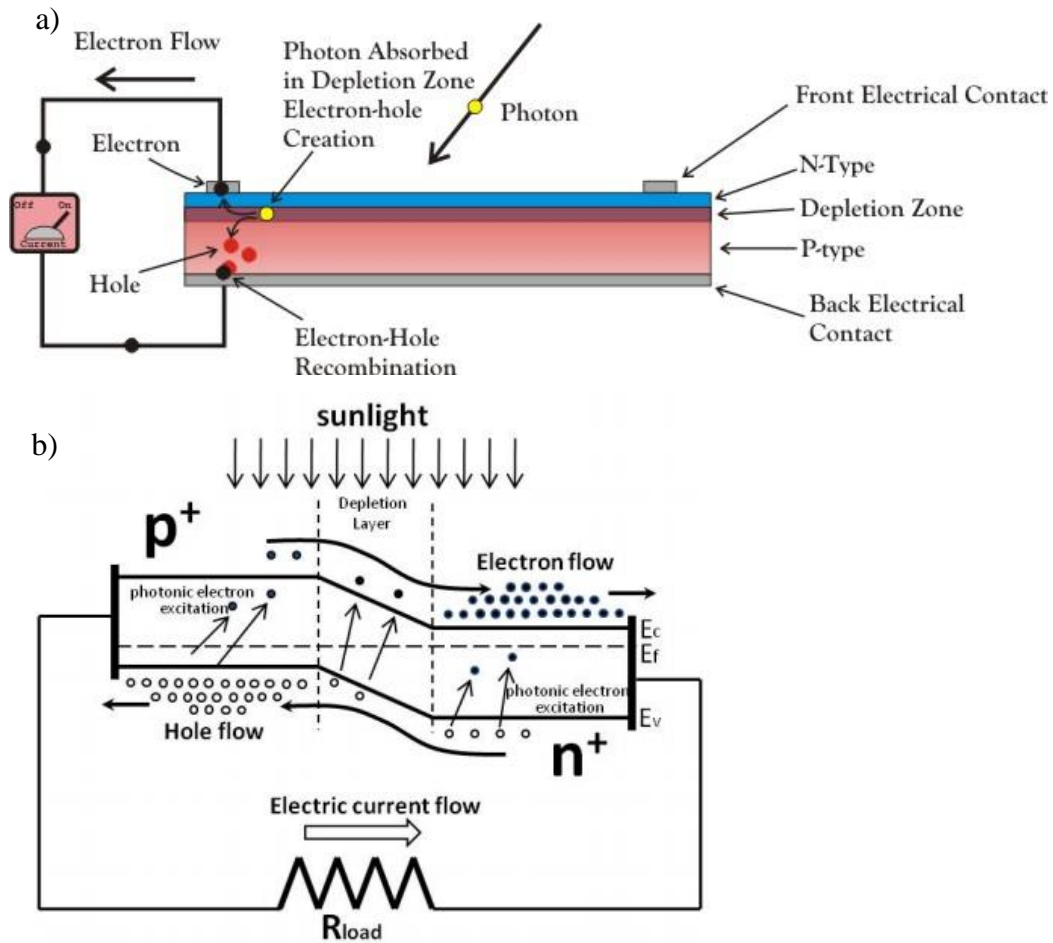


Figure 2.7. a) External and b) internal structure of a p-n junction solar cell [33].

2.1.1.4 Characterization and extraction of device performances

Figure 2.8 shows schematically an example of current density-voltage characteristics of a solar cell under dark and light illumination. The short-circuit current density and the open-circuit voltage, the maximum power point and the voltage and current density at the maximum power point are denoted by I_{sc} , V_{oc} , mpp , V_{mp} and I_{mp} , respectively.

The main parameters of a solar cell are the short-circuit current density (J_{sc}), the open-circuit voltage (V_{oc}), the fill factor (FF) and the solar energy conversion efficiency (η).

The short circuit current density, J_{sc} , is the maximum current density value at $V = 0$ V. This parameter strongly depends on several factors such as the number of absorbed photons, spectrum of the incident light, absorption and reflection coefficients...

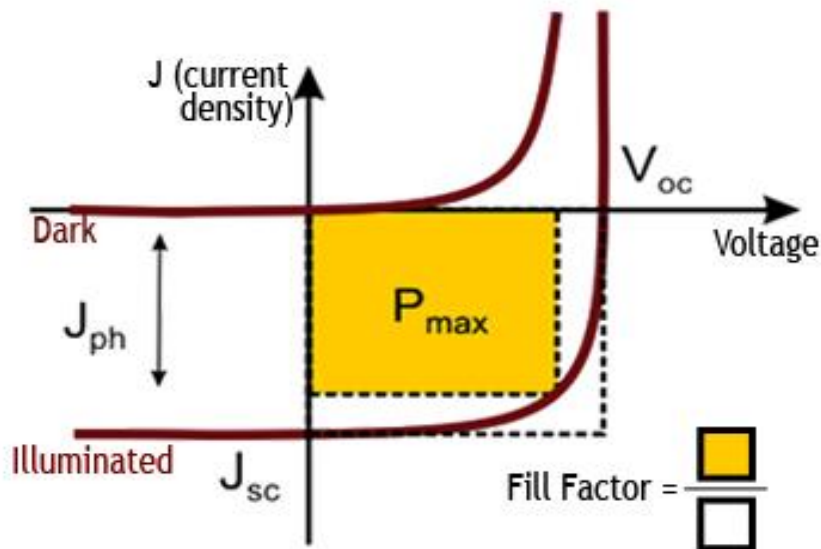


Figure 2.8. A generic J-V curve of a solar cell under sun illumination.

The open-circuit voltage, V_{oc} , is the maximum voltage from a solar cell when the net current through the device is zero.

There is one combination of current and voltage at which the power of the solar cell has its maximum (I_{mp} and V_{mp} , respectively). This point on the I–V characteristic of an illuminated solar cell is called the maximum power point

The maximum power density point (P_{max}) is the product of the cell current density (J_{max}) and the voltage (V_{max}) when the output power of the cell is at its maximum.

The fill factor (FF) is a measure of how far the obtained J-V characteristics differ from an ideal solar cell. In other words, FF is a geometrical parameter which measures the “squareness” of J-V curve. It is defined as the ratio of the maximum power density point to the product of the open circuit voltage and short circuit current density as illustrated in Equation 2.1.

$$FF = \frac{P_{max}}{V_{oc}J_{sc}} \quad (\text{Equation 2.1})$$

The power conversion efficiency is the most commonly used parameter to analyze the performance of one solar cell. It is defined as the ratio of energy output from the solar cell to the incident power density from the sun (Equation 2.2).

$$\eta = \frac{V_{oc} J_{sc} FF}{P_{incident}}$$

(Equation 2.2)

Resistive effects in solar cells could be resumed by two resistors which have a strong impact on the efficiency of the solar cell by dissipating power in the resistances. The equivalent circuit for modeling a solar cell is illustrated in Figure 2.9.

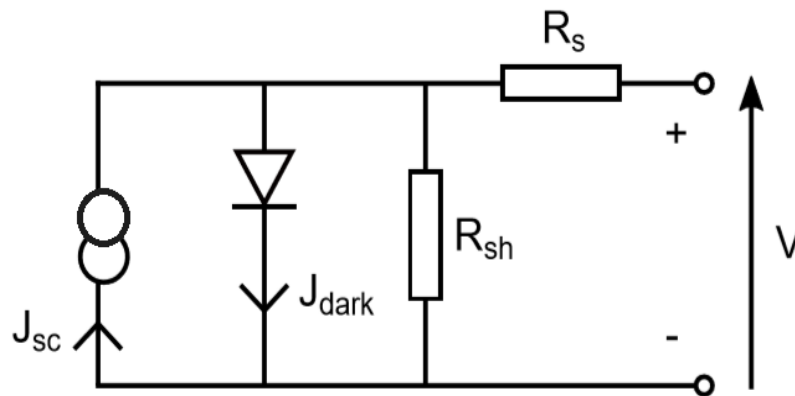


Figure 2.9. Equivalent circuit to model a solar cell with series and shunt resistances.

The most common parasitic resistances are series resistance and shunt resistance whose effects are illustrated in Figure 2.10.

The main impact of series resistance (R_s) is to reduce the fill factor (FF) and the short-circuit current (J_{sc}) at high R_s values (Figure 2.10a).

Low shunt resistance (R_{sh}) values provide a current path causing power losses in solar cells. Very low values of R_{sh} will produce a significant reduction in V_{oc} (Figure 2.10b).

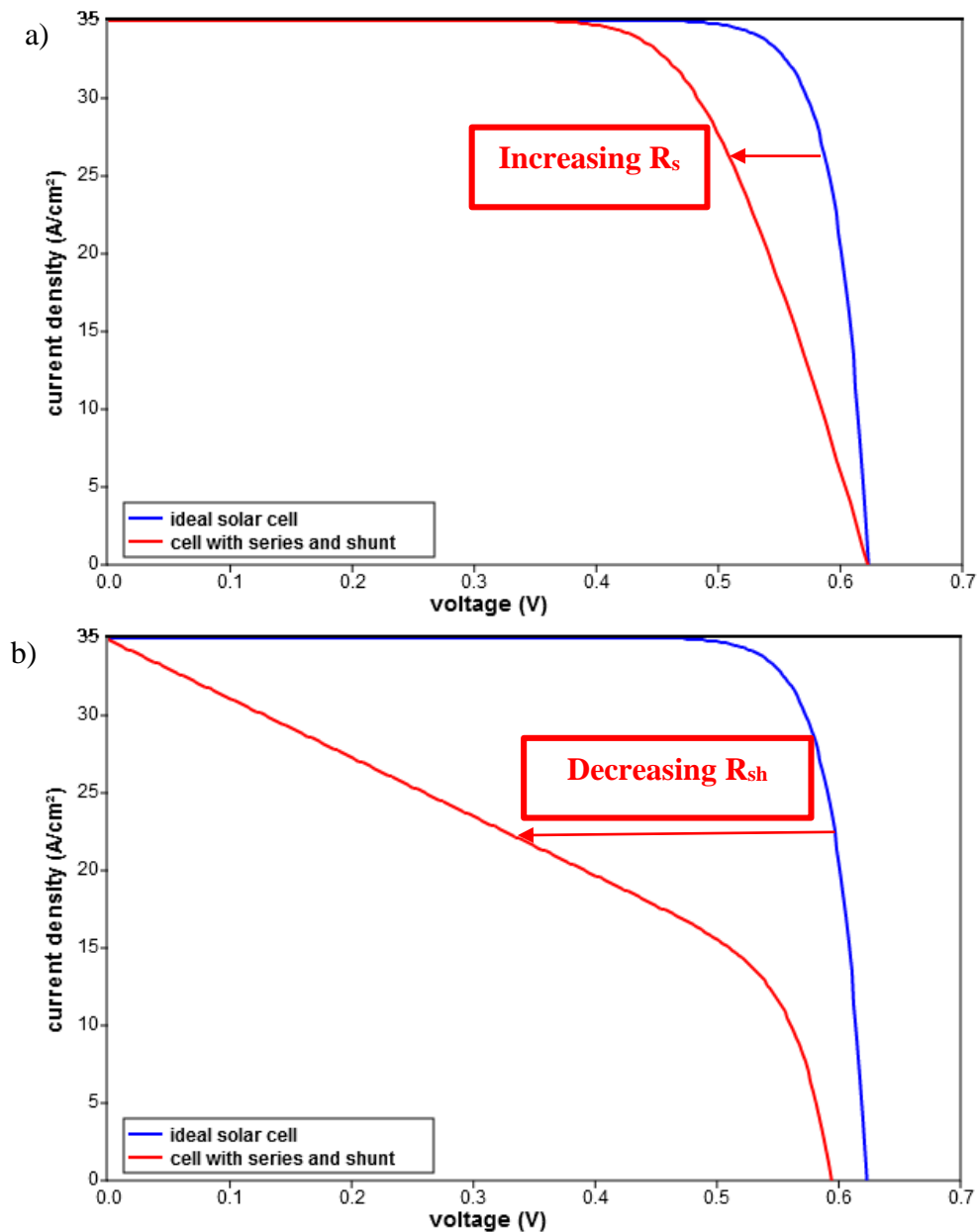


Figure 2.10. Parasitic resistances effects on the I-V characteristics of a solar cell. a) series resistance , b) shunt resistance.

2.1.2 Field effect transistors

2.1.2.1 Perovskite preparation

Perovskite based devices can exhibit very different performances depending on their precursor materials[3–6]. Thus, the identification of the required materials along with the corresponding molar proportion is one of the crucial steps in the fabrication of perovskite based devices.

Perovskite field effect transistors (FETs) were fabricated at Los Alamos National Laboratory and perovskite thin films were obtained from the hot-casting technique previously reported by Nie *et al.*[7].

MAPbI₃

Lead iodide perovskite solution was mix of lead iodide (PbI₂) and methyl ammonium iodide (CH₃NH₃I) with 1:1 molar ratio in a mixture of anhydrous DMSO and DMF (1:1) solvents (Figure 2.11).

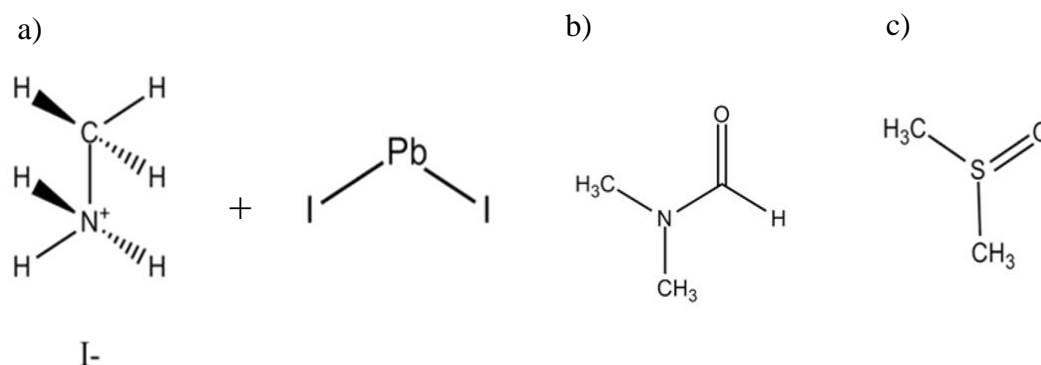


Figure 2.11. Combination of materials used for the preparation of methylammonium lead iodide perovskite. a) CH₃NH₃I + PbI₂, b) DMF solvent, c) DMSO solvent.

This solution was stirred for at least 48 hours at 70 °C before using. The final product is a methylammonium lead iodide perovskite given by the formula CH₃NH₃PbI₃.

Dimethyl sulfoxide (DMSO) was used as a solvent due to its dipolarity and higher boiling point which helps in dissolving and mixing compared to DMF.

MAFACsPbI₃

We also used mixed cation perovskite solution which was mix of lead iodide (PbI₂), formamidinium iodide (CH₅IN₂), methylammonium iodide (CH₃NH₃I) and cesium iodide (CsI) with a molar ratio of 1:0.7:0.25:0.05 respectively dissolved in anhydrous DMSO and DMF solvent (1:1). After mixing the materials in the solvents, the resulting solution was stirred for 24 hours at 70 °C before using. The final product is mixed cation perovskite given by the formula FA_{0.7}MA_{0.25}Cs_{0.05}PbI₃.

We studied the role of Cesium content on mixed cation perovskites by varying the concentration of Cesium to obtain 5%, 15% and 25% Cs on the solution. Consequently, the final products are

mixed cation perovskite given by the formulas $\text{FA}_{0.7}\text{MA}_{0.25}\text{Cs}_{0.05}\text{PbI}_3$, $\text{FA}_{0.6}\text{MA}_{0.25}\text{Cs}_{0.15}\text{PbI}_3$ and $\text{FA}_{0.5}\text{MA}_{0.25}\text{Cs}_{0.25}\text{PbI}_3$ (Figure 2.12).

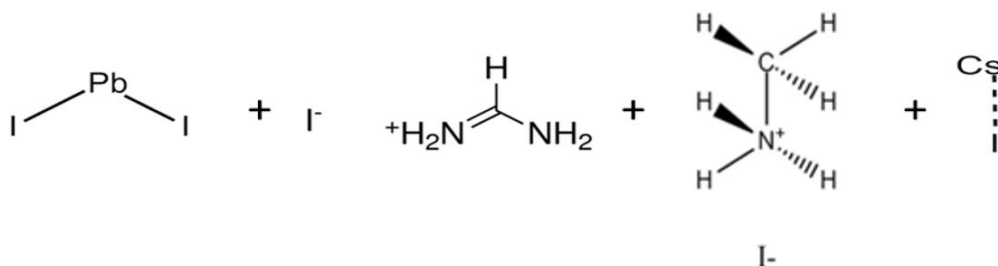


Figure 2.12. Combination of materials used for the preparation of mixed cation perovskite: $\text{PbI}_2 + \text{FAI} + \text{MAI} + \text{CsI}$.

All the materials used such as methylammonium iodide (MAI), lead iodide (PbI_2), formamidinium iodide (FAI), cesium iodide (CsI), dimethylsulfoxide (DMSO) and dimethylformamide (DMF) were purchased from Sigma Aldrich.

As previously said, we used the previously developed hot-casting method to grow perovskite thin films ($t \sim 400$ nm) as active layer for field effect transistors (chapter 3 and 4). This technique was revealed by Nie *et al.* [5] to grow continuous, pinhole-free and large grain-sized crystalline thin films of organometallic perovskites that enables the preparation of high-quality and large-area perovskite crystals.

Figure 2.13 illustrates the processing scheme for perovskite deposition by using such technique.

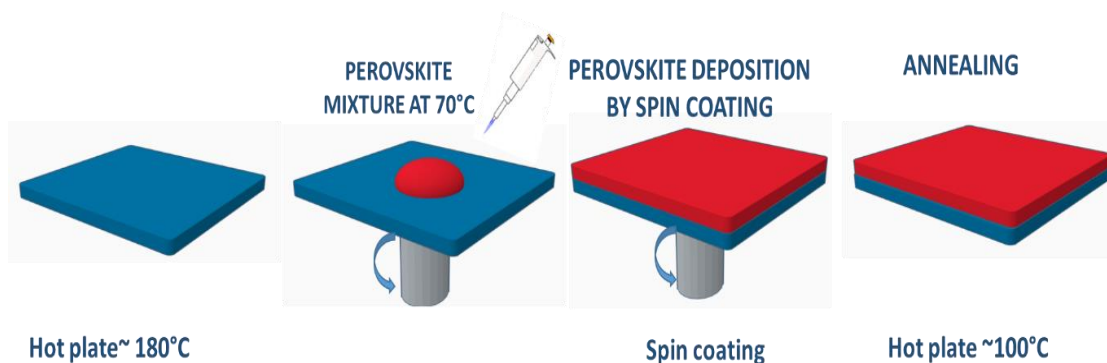


Figure 2.13. Processing scheme for perovskite thin-films deposition using the hot casting technique.

For this approach, we used a hot (70 °C) perovskite precursor ink (MAI: PbI_2 (1:1)) casted onto a preheated and spinning (180 °C) substrates (rotation time 30 seconds). After perovskite spin

coating (thickness ~ 400 nm), the substrates were placed on the hot plate at 100 °C during 10 minutes to fully convert the perovskite precursor into the $\text{CH}_3\text{NH}_3\text{PbI}_3$ perovskite films.

2.1.2.2 FET fabrication

The processing scheme used to fabricate perovskite FETs is illustrated in Figure 2.14.

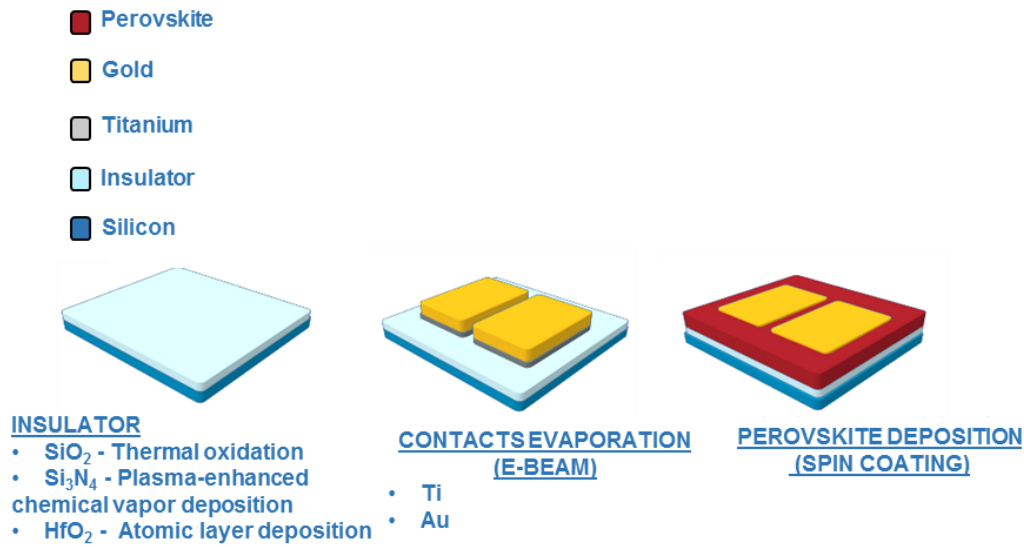


Figure 2.14. Processing scheme for perovskite field effect transistors fabrication.

The substrates used were commercial doped silicon wafers (MTI Corp., Si Wafer (100), N Type Resistivities: 0.1-0.5 ohm-cm). These substrates were first cleaned by RCA process. The RCA (Radio Corporation of America) clean is a standard set of wafer cleaning step. This process allows to obtain a clean silicon surface. For the dielectric layer, we used three types of insulators on heavily n-doped Si wafer (more details are given in chapter 2):

- The first one is a 100 nm-thick thermally grown silicon dioxide layer.
- The second one is a 100 nm-thick silicon nitride deposited by PECVD (plasma-enhanced chemical vapor deposition).
- The last one is a 30 nm-thick hafnium oxide deposited by ALD (atomic layer deposition).

After the dielectric deposition or growth, the substrates were cleaned in an ultrasonic acetone bath, followed by alcohol cleaning during 20 minutes.

30 nm-thick titanium and 180 nm-thick gold electrodes ($100\ \mu\text{m} \times 100\ \mu\text{m}$) were deposited using a shadow mask to define channel dimensions: $W = 100\ \mu\text{m}$ and $L = 70\ \mu\text{m}$.

Subsequently, the patterned-substrates were exposed to oxygen-plasma cleaning treatment for 6 minutes to improve the wetting of the surface and obtain uniform perovskite layers (otherwise perovskite solution does not stick on the insulating layer after its deposition) to proceed with perovskite deposition.

Then, the substrates were rapidly transferred from the glovebox to the probe station (Janis Research ST-500) under vacuum conditions to proceed with the device characterization.

2.1.2.2.1 Insulator deposition/growth

➤ Silicon dioxide growth : Thermal oxidation

Thermal oxidation is a very common technique performed in furnaces to produce oxide layers (Figure 2.15) which can be applied to different materials, but most commonly involves the oxidation of silicon substrates to produce silicon dioxide[11].

Briefly, this technique consists in forcing an oxidizing agent into a silicon wafer at high temperature to produce a chemical reaction and create an oxide layer on the top of the wafer.

In this thesis, 100 nm-thick silicon dioxide films were grown on the top of silicon wafer by thermal oxidation at $1000\ ^\circ\text{C}$.

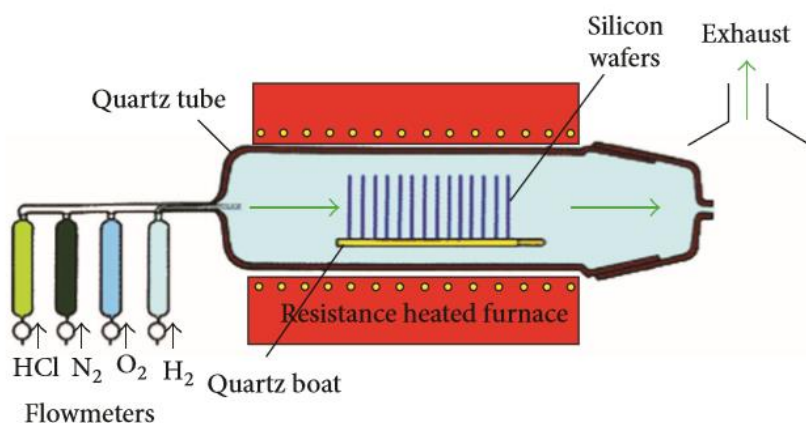


Figure 2.15. Schematic of thermal oxidation technique [32].

Thermally grown silicon dioxide thin films exhibit outstanding advantages such as:

- i) excellent electrical insulator with resistivity values higher than 10^{16} Ωcm and $E_g \sim 9$ eV;
- ii) high breakdown electric field (> 10 MV/cm);
- iii) stable and reproducible Si/SiO₂ interface;
- iv) conformal oxide growth on exposed Si surface ;
- v) good diffusion mask for common dopants and
- vi) good etching selectivity between Si and SiO₂ [11,12].

➤ Silicon nitride deposition: Plasma-enhanced chemical vapor deposition

Plasma-deposited silicon nitride films have been widely used in microelectronics as passivation layers and more recently as gate insulator thanks to their outstanding properties such as high density and dielectric constant, good insulating properties and excellent Na⁺ resistance, excellent mechanical properties , low deposition temperature, high growth rate and good uniformity[13,14].

Plasma-Enhanced Chemical Vapor Deposition (PECVD) is a chemical vapor deposition process commonly used to deposit thin films from a gas state to a solid state on a substrate. Briefly, PECVD deposition consists in introducing reacting gases and creating a plasma by radio frequency excitation. We used two parallel electrodes, one of them being grounded and the other one being a RF-energized electrode (Figure 2.16). The plasma allows the formation of numerous reactive species such as radicals or atomic species. The result of those radicals is principally chemical reactions at the substrate surface which lead to a film deposition. In order to enhance the chemical reaction and the film quality the substrate is heated from 250 °C to 350 °C, depending on the film requirements.

In this thesis, we deposited 100 nm-thick silicon nitride films by PECVD at 250 °C (Oxford PECVD system) by using silane and ammonia as reactant gases and nitrogen as diluent.

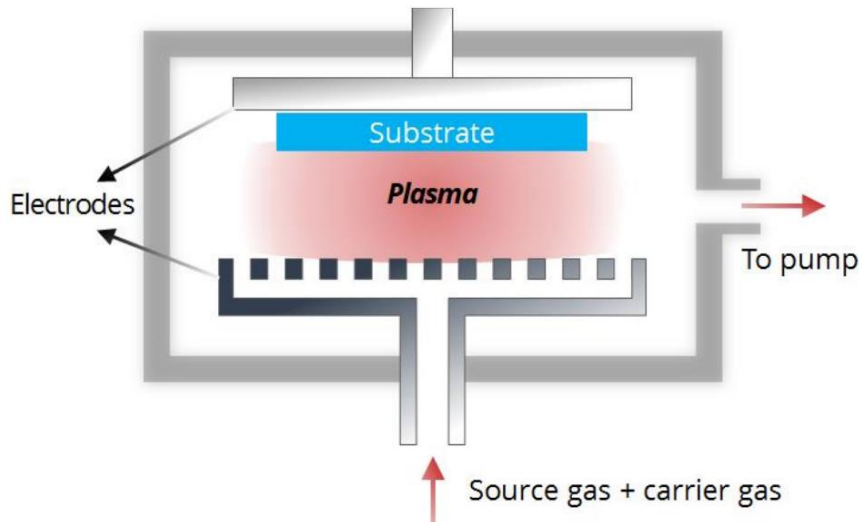


Figure 2.16. Schematic of plasma enhanced chemical vapor deposition (PECVD) process [30].

➤ Hafnium dioxide deposition: Atomic layer deposition

Hafnium dioxide (HfO_2) layers deposited by atomic layer deposition (ALD) are used as high-k materials for replacing silicon dioxide as gate dielectric in MIS devices[15–17].

Atomic layer deposition (ALD) is considered as a subclass of chemical vapor deposition to obtain a thin film on a substrate, using a gas cycle.

The principle is similar to chemical vapor deposition (CVD), except that ALD involves the use of two precursors which react sequentially on the substrate surface to produce a solid thin film (Figure 2.17). In other words, it is based on the sequential use of self-terminating gas-solid reactions. Thus, since ALD film growth is self-limited and based on surface reactions, the film thickness deposited can be as fine as one monolayer. Subsequently, the chamber is purged with an inert carrier gas (typically N_2 or Ar) to remove any unreacted precursor or reaction by-products.

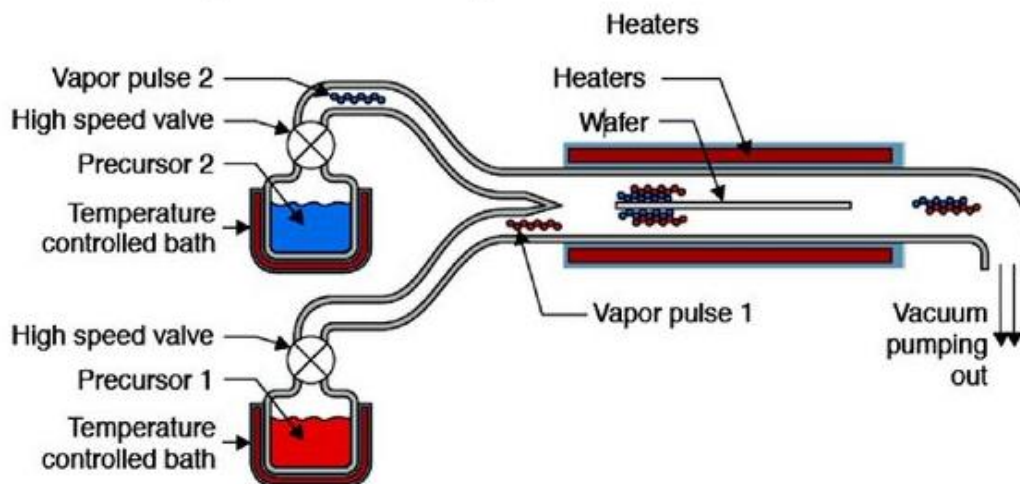


Figure 2.17. Schematic of atomic layer deposition process [18].

In this thesis, we deposited 30 nm-thick hafnium dioxide layer by ALD (The PICOSUN R-200 Advanced ALD system) with Tetrakis(dimethylamido) hafnium (TDMAH) and water as precursors at 250 °C.

2.1.2.2.2 Metal electrodes deposition

Electron beam deposition was used to obtain 30 nm-thick titanium and 180 nm-thick gold electrodes. The electron beam scans the surface of the target material which evaporates and condensates at the substrate surface as illustrated in Figure 2.18.

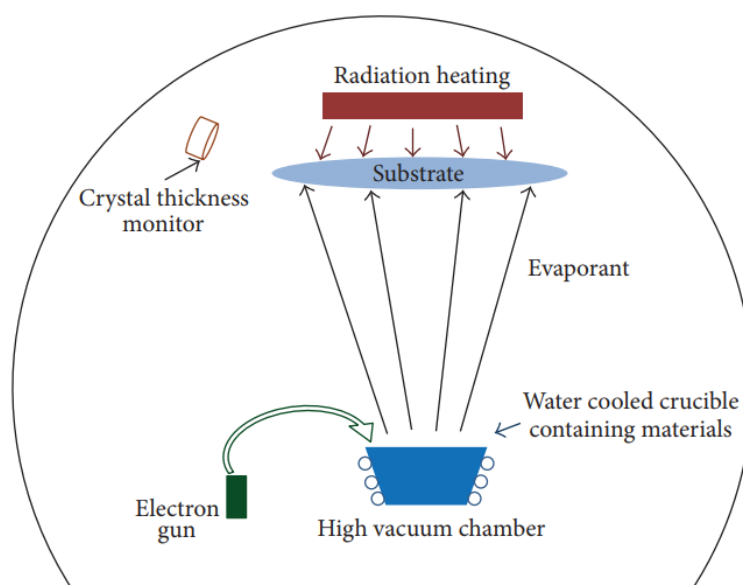


Figure 2.18. Processing scheme for electron beam evaporation [30].

2.1.2.3 Working principle

According to the adopted device configuration, several geometries can be employed for the fabrication of field effect transistors: bottom gate/ bottom contact (Figure 2.19a), bottom gate/ top contact (Figure 2.19b), top gate/ top contact (Figure 2.19c) and top gate/ bottom contact (Figure 2.19d) structures.

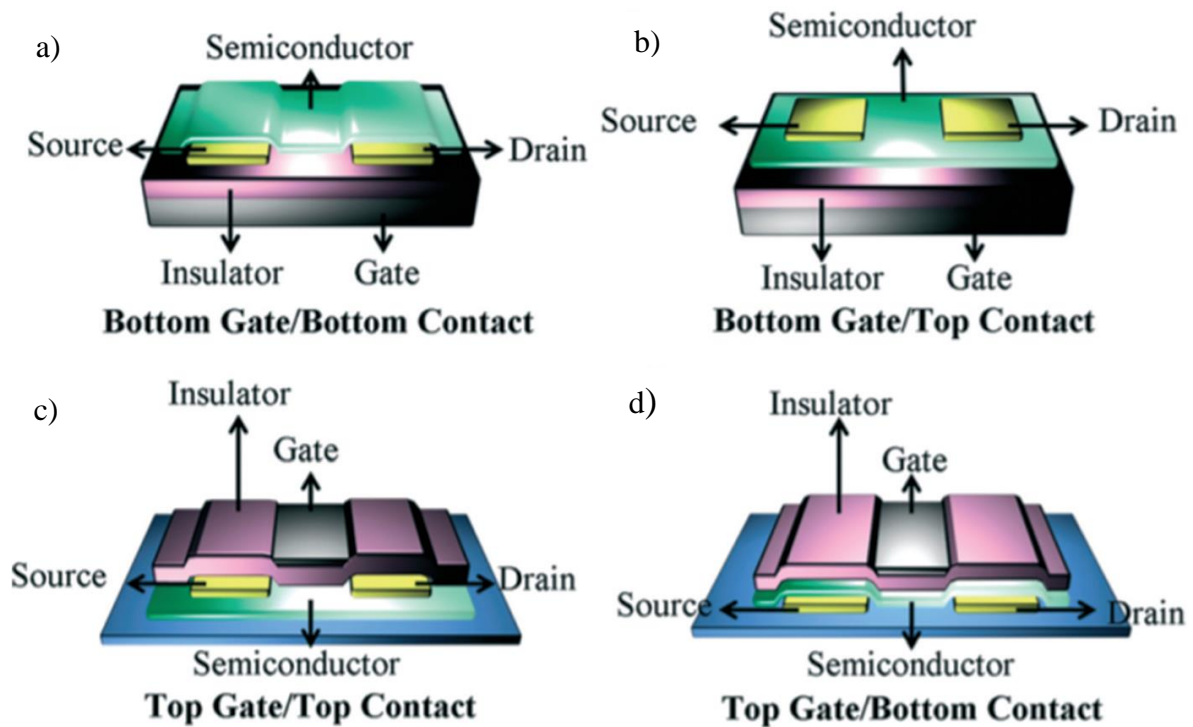


Figure 2.19. Schematic representative of top and bottom contact FETs. a) Bottom Gate/ Bottom Contact; b) Bottom Gate/ Top Contact; c) Top Gate/ Top Contact; d) Top Gate/ Bottom Contact [34].

The working principle of FET can be explained by a metal-insulator-semiconductor (MIS) structure. When a MIS structure is biased with positive or negative voltages, three regimes of operation can be observed: accumulation, depletion and inversion with two characteristics voltages, V_{FB} (Flat band voltage) and V_T (threshold voltage) (Figure 2.20).

Briefly, for p-type semiconductors for example, when a voltage with lower value to the flat band voltage is applied on the metal gate ($V_{GS} < V_{FB}$), the majority charges (holes) are accumulated at the semiconductor-dielectric interface (accumulation mode). The top of the

valence band bends upward getting closer to the Fermi energy. When the applied gate voltage is higher than the flat band voltage ($V_{GS} > V_{FB}$), the semiconductor is depleted by the minority charges and consequently the transistor is switched off (depletion mode). The top of the valence band moves away and causes an empty carrier zone (Space Charge Zone). In the case of a larger positive voltage applied ($V_{GS} \gg V_{FB}$) the band bends further downward so that the intrinsic level E_i at the surface crosses over the Fermi level E_f . The minority charges (electrons) are induced at the gate dielectric/semiconductor interface. This condition is called inversion because the number of electrons (minority carriers) at the surface is larger than that of the holes, so the surface is inverted. The minority carriers (electrons) are accumulated at the semiconductor-dielectric interface forming a conducting path between the source and drain electrodes allowing a current to flow.

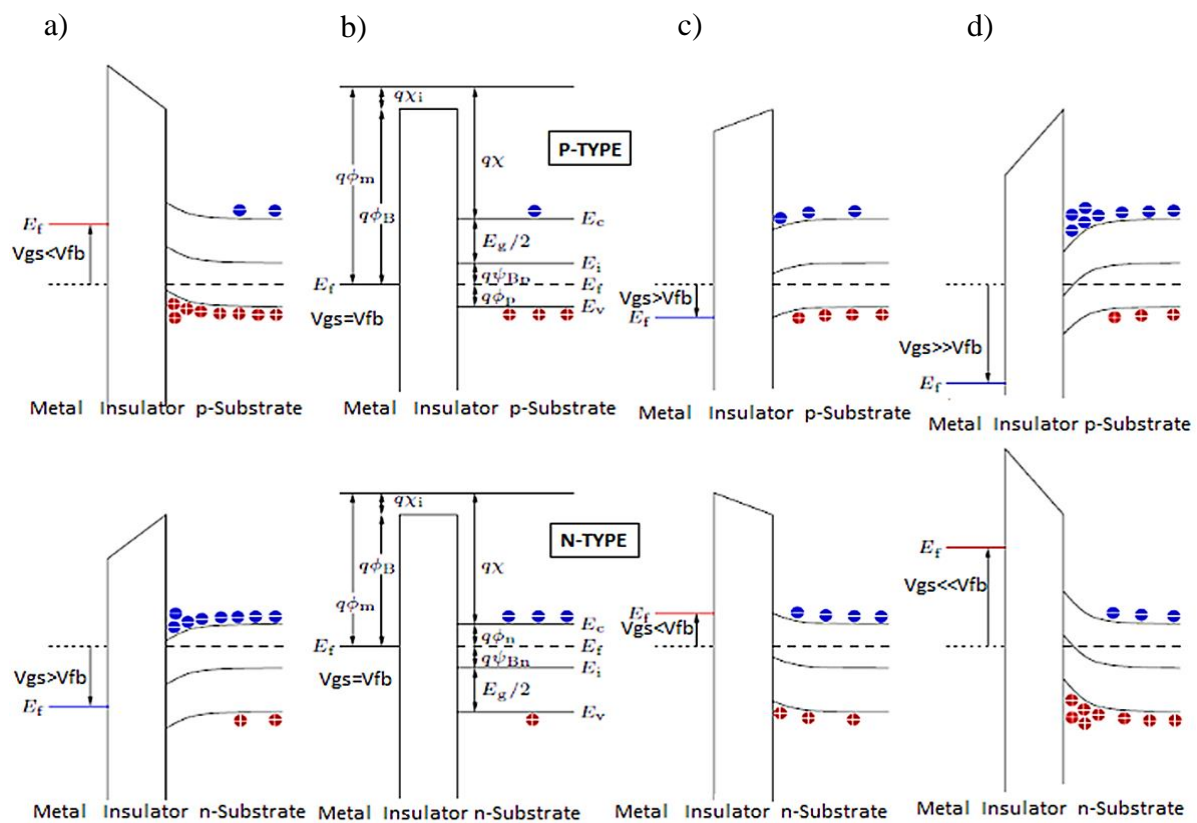


Figure 2.20. The energy band diagrams for ideal MIS-capacitors under different bias conditions: (a) accumulation, (b) flatband, (c) depletion, and (d) inversion.

The above information helps to understand the field effect operation in terms of energy level diagrams.

Figure 2.21 illustrates the relative position of the top of the valence band (E_v) and the bottom of the conduction band (E_c) with the work function of the source/drain electrodes for different V_G and V_{DS} voltages. If there is no gate voltage applied (V_G), a semiconductor intrinsically undoped will not show any disequilibrium of charge carriers (Figure 2.21a). Direct injection from source/drain electrodes is the only way to create flowing current in the semiconductor. When a negative voltage is applied ($V_G < 0$), for p-type semiconductors for example, positive charges are attracted to the interface between the semiconductor and the gate dielectric to create an accumulation layer. Consequently, due to electrical field created the fermi level along with the E_v and E_c of the semiconductor are displaced towards the highest energy of the system (Figure 2.21b). Thus, if the Fermi level of source/drain metal is close to the E_v of the p-type semiconductor for instance, the positive charges can be extracted by the electrodes by applying a voltage V_{DS} , between drain and source (Figure 2.21c).

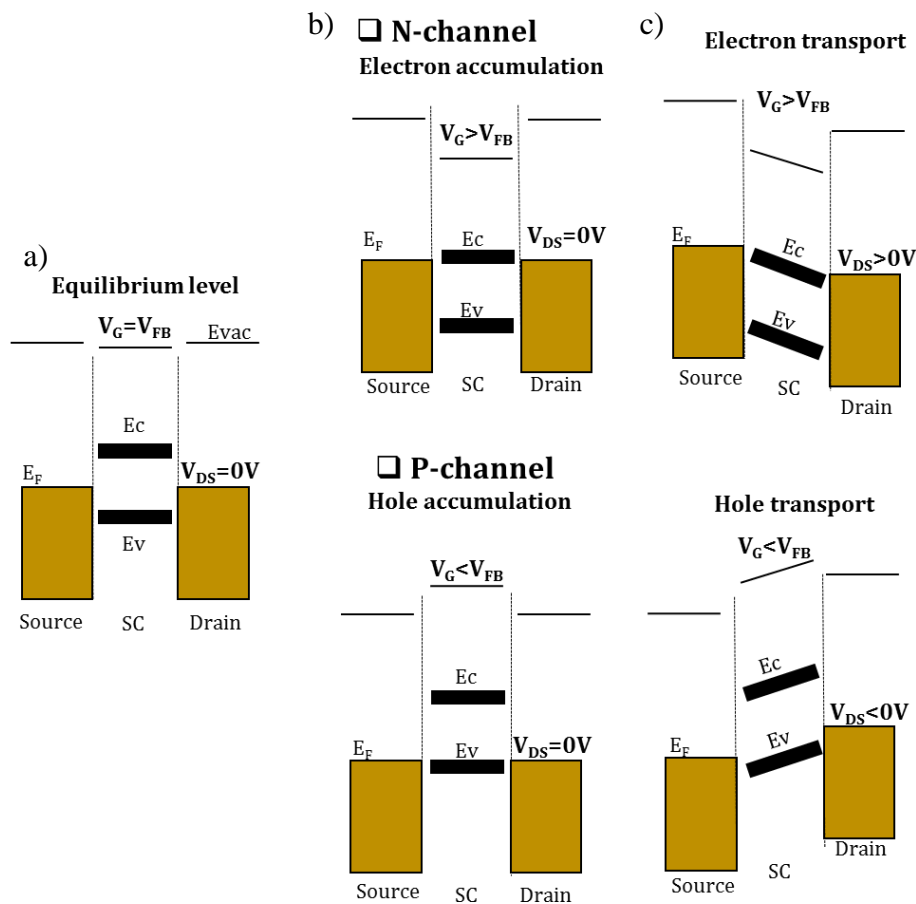


Figure 2.21. Illustration of working principle of a FET in terms of energy level diagrams.

Several factors play a key role in FETs device performance for example:

- interface and energy alignments between the semiconductor and the electrodes
- dielectric thickness and permittivity
- the device configuration ...

2.1.2.4 Characterization and extraction of devices parameters

Typical transfer (I_D as a function of V_{DS} at fixed V_{GS}) and output characteristics (I_D as a function of V_{GS} at fixed V_{DS} bias) of a FET are illustrated in Figure 2.22.

Three different operating regimes can be distinguished in FETs which are: off state, linear and saturation regime. When the applied gate voltage is lower than the threshold voltage V_{TH} , which represents the on-set for the conducting channel formation, the transistor is turned off which is known as cut off region. When $V_{GS} > V_{TH}$ and $V_{DS} \ll V_{GS} - V_{TH}$ the channel has a behavior of an ohmic resistance where the drain current increases linearly with V_{DS} : this is known as linear regime. When $V_{DS} > V_{GS} - V_{TH}$, the drain current remains constant reaching the saturation value: this is known as saturation region.

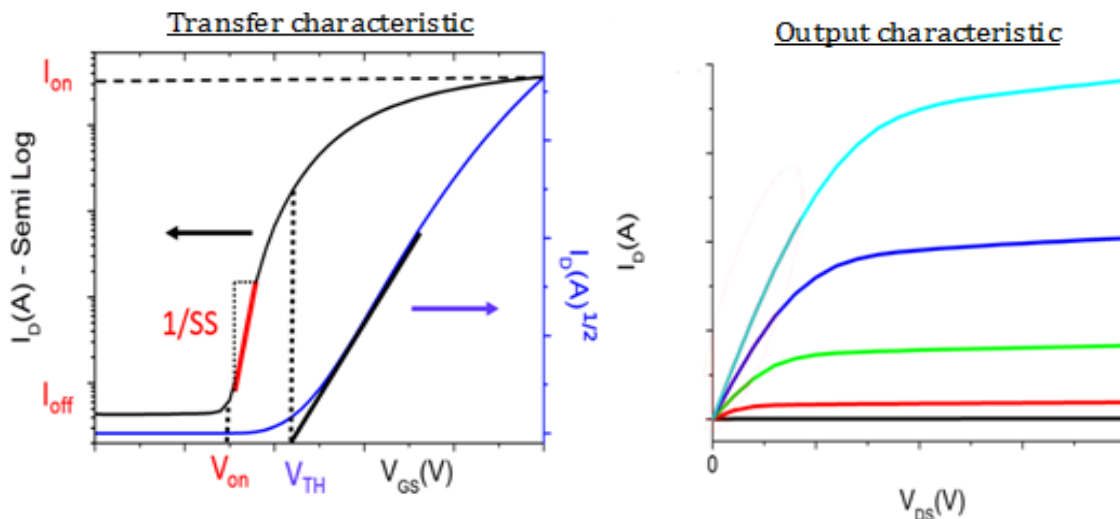


Figure 2.22. Typical transfer and output characteristics of field effect transistors [35].

I_{on}/I_{off} ratio is used to determine the difference between the off state and on state. These two current I_{on} and I_{off} are extracted from the curve in logarithmic scale in the linear region. I_{on} is the maximum observed current in the transfer characteristic and I_{off} represents the lowest one.

V_{ON} is the V_G required to turn the device on where the channel current starts to flow due to field-induced charge accumulation at the dielectric/semiconductor interface.

The transconductance g_m (equation 2.3), corresponds to the slope of the transistors curves $I_{DS}=f(V_{GS})$.

$$g_m = \frac{dI_{DS}}{dV_{GS}} \quad (\text{Equation 2.3})$$

The threshold voltage (V_{TH}) is the gate voltage necessary to turn on and create the conduction channel at the oxide/semiconductor interface. This value can be calculated from the intercept of the line drawn through the linear region of the $I_{DSat}^{1/2}$ versus V_G .

The FET mobility (μ) can be estimated either from linear or from the gate field dependence of the saturation current where I_D values are:

$$I_{DSlinear} = \frac{\mu C_i W}{L} [(V_{GS} - V_{TH})V_{DS} - \frac{V_{DS}^2}{2}] \quad (\text{Equation 2.4})$$

$$I_{DSsaturation} = \frac{\mu C_i W}{2L} (V_{GS} - V_{TH})^2 \quad (\text{Equation 2.5})$$

where W is the channel width, L source-drain channel length and C_i is the insulator capacitance per unit area.

There is a strong impact on the mobility values when the structural and interface defects are important. This model presents the ideal case, based on silicon transistor theory. We used this model to extract the MOS parameters in this thesis.

2.2 Characterization techniques

2.2.1 Microscope techniques

In this thesis, optical, scanning and atomic force microscopes were used to analyze the perovskite thin films morphology and quality.

2.2.1.1 Optical microscope measurement

The optical microscope images of perovskite films were collected using an optical bright-field microscope (Model: Olympus BX51M) with 5X and 10X focal lengths under Olympus U-DICR prism at room temperature.

2.2.1.2 Scanning electron microscope

Scanning electron microscopy imaging was obtained on a field emission scanning electron microscope (JSM-7100 Thermal field emission electron microscope) at an electron energy of 15.0 kV in order to obtain high resolution images of perovskite thin films[21,22].

Figure 2.23 illustrates the processing scheme of the working principle of scanning electron microscope.

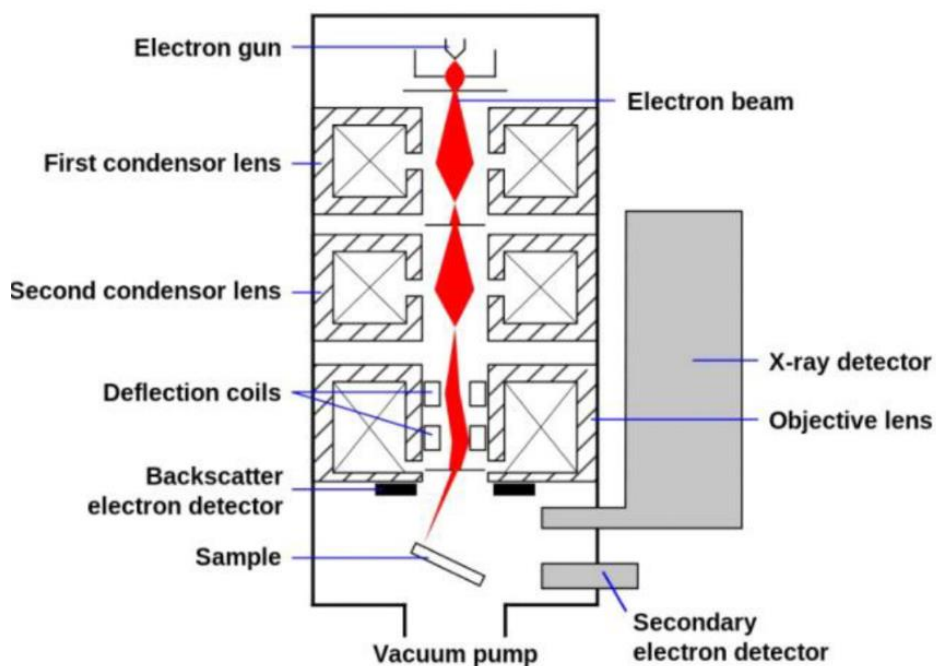


Figure 2.23. Processing scheme for scanning electron microscope [28].

A beam of energetic electrons is generated by an electron gun and goes through a column and onto a series of electromagnetic lenses which are wrapped in coil (referred as solenoids) as illustrated in Figure 2.23.

Briefly, this technique consists in scanning a focused electron beam over a surface to create an image. The interaction between the electron beam with the sample results in different types of electron signals emitted at or near the specimen surface which are collected and processed by an electron detector to obtain the desired information about the surface topography and composition. Different signals can be captured using different detectors to generate an image: low-energy secondary electrons, high-energy backscattered electrons, transmitted electrons and characteristic X-rays....

2.2.1.3 Atomic force microscope

AFM imaging was obtained on an atomic force microscope (Veeco DiCaliber) in order to obtain high resolution images of perovskite thin films. This technique shows different advantages:

- i) it can be performed in different environments from ultra-high vacuum to fluids
- ii) it is capable of producing 3D images with height information
- iii) Mean roughness, coverage and crystal size could be obtained by statistical treatment [23,24].

This technique is based on the interaction of a sharp tip (typically of Si or Si₃N₄ located at the end of the microscope cantilever) with the sample surface. The forces caused by this interaction lead to a deflection of the cantilever which can be modeled with Hooke's law (Equation 2.6):

$$F = kx \quad \text{(Equation 2.6)}$$

where k is a constant factor characteristic of the spring, and x is the total possible deformation of the spring.

This deflection is measured by using a laser spot reflected from the top of the surface of the cantilever into a four quadrant photodiodes as illustrated in Figure 2.24.

According to the nature of the tip motion, AFM operation can be described as contact mode and non-contact mode (tapping). In the last case, piezoelectric oscillations can be obtained at a wide range of frequencies.

In this thesis, we used the contact mode where the force between the tip and the sample during the scanning is kept constant to analyze the perovskite morphology.

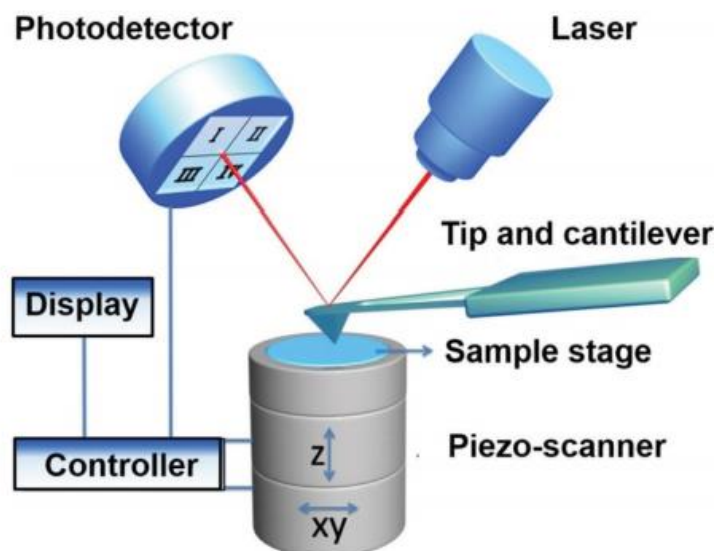


Figure 2.24. Schematic representation of an atomic force microscope [29].

2.2.2 Crystallinity analysis

In this thesis, X-ray diffraction (XRD) and Grazing-Incidence Wide-Angle X-ray Scattering (GIWAXS) were used to analyze the structural quality and crystallinity of hybrid perovskite thin films[25–28].

X-ray diffraction (XRD) is one of the most used tools to analyze the orientation and crystal structure of materials and thin films. The X-ray beam is directed to the film surface and diffracts into many specific directions. By measuring the angles and the intensity of the diffracted beam the crystal structure and orientation can be produced according to Bragg's law (Figure 2.25).

The diffracted X-rays are detected when conditions satisfy Bragg's Law (Equation 2.7) which describes the condition on θ for the constructive interference:

$$2d\sin\theta = n\lambda \quad (\text{Equation 2.7})$$

where d is the lattice spacing of the crystal planes and λ is the wavelength of the incident beam and n is a positive integer.

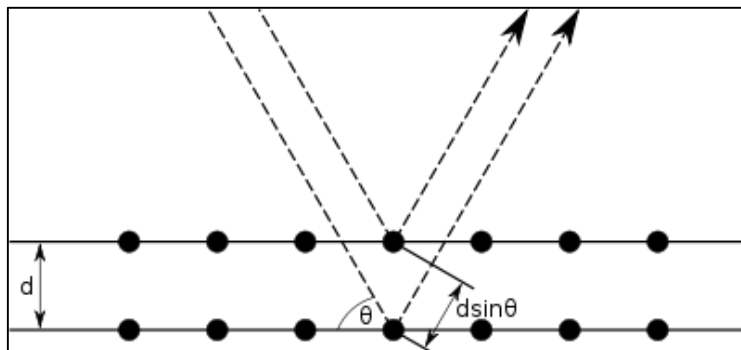


Figure 2.25. Basic diffraction pattern from two planes in crystal structure.

Thus, the identification of the material can be done by the conversion of the diffraction peaks to d-spacing which is unique for each crystal.

In this thesis, XRD (X-Ray Diffraction) spectrum analysis was carried out in a Rigaku Ultima III X-Ray Diffractometer with θ - 2θ configuration and scanning interval between 5° - 50° . The scanning rate used for the measurements was $5^\circ/\text{min}$. All the samples were prepared with perovskites solutions on ITO/glass substrates.

Grazing-Incidence Wide-Angle X-ray Scattering (GIWAXS) is another X-ray-diffraction technique wherein wide-angle scattering is collected. We used GIWAXS measurements to compare the perovskite film morphologies obtained with the hot casting and standard techniques respectively.

For synchrotron GIWAXS measurements, all the samples were prepared with perovskites solutions on ITO/glass substrates. The samples were placed on a programmable temperature control stage (temperature set at 25°C) inside a vacuum chamber pumped down to 10^{-5} Torr. The two-dimensional GIWAXS maps were obtained with incident angle of 0.25° and 10 s exposures for every 10 minutes interval. GIWAXS data were processing with GIXSGUI package for Matlab (Mathworks) with correction for detector sensitivity, X-ray polarization and geometrical solid-angle. The line-cut analysis of GIWAXS maps for perovskite thin-films were compared and indexed with peaks from regular GIXRD spectra with well-resolved peaks.

2.2.3 Optical absorption spectroscopy

Optical absorbance spectrum was used to analyze the quality of perovskite thin films. This technique is based on applying a light beam on the sample to measure the intensity of the radiation that passes through it (I_t) and by comparison to the initial intensity of light (I_0), we determine the amount of light absorbed by the sample. Transmittance is the fraction of light that passes through the sample calculated using the Equation 2.8:

$$\text{Transmittance} = \frac{I_t}{I_0} \quad (\text{Equation 2.8})$$

Absorption of the material can be extracted from the transmittance by using the Equation 2.9.

$$\text{Absorbance (A)} = -\log(T) \quad (\text{Equation 2.9})$$

When a photon carrying an energy E_x falls onto the film, it can be absorbed if E_x (photon) > E_g (material) and it will be transmitted if E_x (photon) < E_g (material).

In terms of wavelength,

$$E_g (eV) = \frac{1.24}{\lambda(\mu m)} \quad (\text{Equation 2.10})$$

In this thesis UV-Visible absorption spectra were acquired on a JASCO V-730 UV visible Spectrophotometer. We recorded the transmission and reflection of light in the wavelength regime 300-900 nm on perovskite thin films deposited on glass substrates.

2.2.4 Current voltage curves

2.2.4.1 Solar cells characterization

The Current - voltage characteristics of the perovskite solar cells were obtained by using Keithley 2636B SourceMeter under ambient conditions. These measurements were performed at room temperature under simulated AM 1.5 G irradiation (100 mW/cm^2) using a xenon-lamp-based solar simulator (Solar Simulator Oriel Sol1A). The output power of the lamp was calibrated by a reference cell.

2.2.4.2 Field effect transistor characterization

The characteristics of perovskite field effect transistors were analyzed by YOKOGAWA 7562 Digital Multimeters along with a current amplifier under vacuum conditions (Pressure $\leq 10^{-4}$ Torr). The maximum input voltage is about ± 1000 V (peak) continuously in a DC voltage range of 200 V to 1000 V. Whereas, the maximum input current is ± 2 A (DC+AC peaks).

In chapter 3, we performed capacitance measurements to quantify the charge density on perovskite based FETs. These measurements were carried out in the frequency range 100 Hz- 10^5 Hz at room temperature under vacuum conditions (Pressure $\leq 10^{-4}$ Torr) on Hewlett-Packard Precision LCR meter (Model 4248A).

In this chapter, we focused on describing the techniques of fabrication and characterization of perovskite based field effect transistors and solar cells. The next chapter describes the characterization at room temperature of methylammonium lead iodide (MAPbI₃) perovskite based field effect transistors

2.3 References

- [1] S. Tombe, G. Adam, H. Heilbrunner, C. Yumusak, D.H. Apaydin, B. Hailegnaw, C. Ulbricht, C.J. Arendse, H. Langhals, E. Iwuohaa, others, The influence of perovskite precursor composition on the morphology and photovoltaic performance of mixed halide MAPbI_{3-x}Cl_x solar cells, *Solar Energy*. 163 (2018) 215–223.
- [2] N. Setter, L. Cross, The role of B-site cation disorder in diffuse phase transition behavior of perovskite ferroelectrics, *Journal of Applied Physics*. 51 (1980) 4356–4360.
- [3] M. Saliba, T. Matsui, J.-Y. Seo, K. Domanski, J.-P. Correa-Baena, M.K. Nazeeruddin, S.M. Zakeeruddin, W. Tress, A. Abate, A. Hagfeldt, others, Cesium-containing triple cation perovskite solar cells: improved stability, reproducibility and high efficiency, *Energy & Environmental Science*. 9 (2016) 1989–1997.
- [4] F.K. Aldibaja, L. Badia, E. Mas-Marzá, R.S. Sánchez, E.M. Barea, I. Mora-Sero, Effect of different lead precursors on perovskite solar cell performance and stability, *Journal of Materials Chemistry A*. 3 (2015) 9194–9200.
- [5] W. Nie, H. Tsai, R. Asadpour, J.-C. Blancon, A.J. Neukirch, G. Gupta, J.J. Crochet, M. Chhowalla, S. Tretiak, M.A. Alam, others, High-efficiency solution-processed perovskite solar cells with millimeter-scale grains, *Science*. 347 (2015) 522–525.
- [6] W. Nie, H. Tsai, J.-C. Blancon, F. Liu, C.C. Stoumpos, B. Traore, M. Kepenekian, O. Durand, C. Katan, S. Tretiak, others, Critical role of interface and crystallinity on the performance and photostability of perovskite solar cell on nickel oxide, *Advanced Materials*. 30 (2018) 1703879.
- [7] W. Nie, J.-C. Blancon, A.J. Neukirch, K. Appavoo, H. Tsai, M. Chhowalla, M.A. Alam, M.Y. Sfeir, C. Katan, J. Even, others, Light-activated photocurrent degradation and self-healing in perovskite solar cells, *Nature Communications*. 7 (2016) 11574.
- [8] H. Tsai, R. Asadpour, J.-C. Blancon, C.C. Stoumpos, O. Durand, J.W. Strzalka, B. Chen, R. Verduzco, P.M. Ajayan, S. Tretiak, J. Even, M.A. Alam, M.G. Kanatzidis, W. Nie, A.D. Mohite, Light-induced lattice expansion leads to high-efficiency perovskite solar cells, *Science*. 360 (2018) 67–70. doi:10.1126/science.aap8671.
- [9] M. Mizuhashi, Electrical properties of vacuum-deposited indium oxide and indium tin oxide films, *Thin Solid Films*. 70 (1980) 91–100.
- [10] H. Kim, C. Gilmore, A. Pique, J. Horwitz, H. Mattoussi, H. Murata, Z. Kafafi, D. Chrisey, Electrical, optical, and structural properties of indium–tin–oxide thin films for organic light-emitting devices, *Journal of Applied Physics*. 86 (1999) 6451–6461.
- [11] B.E. Deal, A. Grove, General relationship for the thermal oxidation of silicon, *Journal of Applied Physics*. 36 (1965) 3770–3778.
- [12] C. Herzinger, B. Johs, W. McGahan, J.A. Woollam, W. Paulson, Ellipsometric determination of optical constants for silicon and thermally grown silicon dioxide via a multi-sample, multi-wavelength, multi-angle investigation, *Journal of Applied Physics*. 83 (1998) 3323–3336.
- [13] Y. Kuo, Plasma enhanced chemical vapor deposited silicon nitride as a gate dielectric film for amorphous silicon thin film transistors—A critical review, *Vacuum*. 51 (1998) 741–745.
- [14] L. Liu, W. Liu, N. Cao, C. Cai, Study on The Performance of PECVD Silicon Nitride Thin Films, *Defence Technology*. 9 (2013) 121–126. doi:https://doi.org/10.1016/j.dt.2013.10.004.
- [15] P.J. Cowdery-Corvan, D.H. Levy, S.F. Nelson, D.C. Freeman, T.D. Pawlik, Process for atomic layer deposition, Google Patents, 2012.
- [16] M. Leskelä, M. Ritala, Atomic layer deposition (ALD): from precursors to thin film structures, *Thin Solid Films*. 409 (2002) 138–146.
- [17] M. Ritala, M. Leskelä, Atomic layer deposition, in: *Handbook of Thin Films*, Elsevier, 2002: pp. 103–159.
- [18] L. ICKnowledge, Technology Backgrounder: Atomic Layer Deposition, ICKnowledge. Com. (2004) 1–7.
- [19] W. Nie, H. Tsai, R. Asadpour, J.-C. Blancon, A.J. Neukirch, G. Gupta, J.J. Crochet, M. Chhowalla, S. Tretiak, M.A. Alam, H.-L. Wang, A.D. Mohite, High-efficiency solution-processed perovskite solar cells with millimeter-scale grains, *Science*. 347 (2015) 522–525. doi:10.1126/science.aaa0472.

- [20] J.I. Goldstein, D.E. Newbury, J.R. Michael, N.W. Ritchie, J.H.J. Scott, D.C. Joy, Scanning electron microscopy and X-ray microanalysis, Springer, 2017.
- [21] L. Reimer, Scanning electron microscopy: physics of image formation and microanalysis, Springer, 2013.
- [22] H.-J. Butt, B. Cappella, M. Kappl, Force measurements with the atomic force microscope: Technique, interpretation and applications, *Surface Science Reports*. 59 (2005) 1–152.
- [23] T. Okada, S. Mishima, T. Takase, H. Miyamoto, H. Ohta, Y. Satoh, Y. Enomoto, T. Matsuzawa, Y. Nakamura, H. Kajimura, others, Atomic force microscope, Google Patents, 1993.
- [24] B. Borie, X-Ray Diffraction in Crystals, Imperfect Crystals, and Amorphous Bodies., *Journal of the American Chemical Society*. 87 (1965) 140–141.
- [25] B.D. Cullity, S.R. Stock, *Elements of X-ray Diffraction*, Pearson Education, 2014.
- [26] H.P. Klug, L.E. Alexander, *X-ray diffraction procedures: for polycrystalline and amorphous materials*, *X-Ray Diffraction Procedures: For Polycrystalline and Amorphous Materials*, 2nd Edition, by Harold P. Klug, Leroy E. Alexander, Pp. 992. ISBN 0-471-49369-4. Wiley-VCH, May 1974. (1974) 992.
- [27] J. Kreisel, A. Glazer, G. Jones, P. Thomas, L. Abello, G. Lucazeau, An x-ray diffraction and Raman spectroscopy investigation of A-site substituted perovskite compounds: the (Na_{1-x}K_x)_{0.5}Bi_{0.5}TiO₃ (0 x1) solid solution, *Journal of Physics: Condensed Matter*. 12 (2000) 3267.
- [28] Om Prakash Choudhary and Priyanka. 2017. Scanning Electron Microscope: Advantages and Disadvantages in Imaging Components *Int.J.Curr.Microbiol.App.Sci*. 6(5): 1877-1882.
- [29] Y. Shan, H. Wang, The structure and function of cell membranes examined by atomic force microscopy and single-molecule force spectroscopy, *Chemical Society Reviews*. 44 (2015) 3617–3638.
- [30] S.-I. Park, Y.-J. Quan, S.-H. Kim, H. Kim, S. Kim, D.-M. Chun, C.S. Lee, M. Taya, W.-S. Chu, S.-H. Ahn, A review on fabrication processes for electrochromic devices, *International Journal of Precision Engineering and Manufacturing-Green Technology*. 3 (2016) 397–421.
- [31] N. Xu, S.E. Huq, Novel cold cathode materials and applications, *Materials Science and Engineering: R: Reports*. 48 (2005) 47–189.
- [32] N. Asim, S. Ahmadi, M. Alghoul, F. Hammadi, K. Saeedfar, K. Sopian, Research and development aspects on chemical preparation techniques of photoanodes for dye sensitized solar cells, *International Journal of Photoenergy*. 2014 (2014).
- [33] P.S. Priambodo, N.R. Poespawati, D. Hartanto, Solar Cell, in: *Solar Cells-Silicon Wafer-Based Technologies*, InTech, 2011.
- [34] X. Chen, R. Zhou, S. Mao, J. Chen, Rapid detection of nutrients with electronic sensors: A review, *Environmental Science: Nano*. 5 (2018).
- [35] S.R. Thomas, P. Pattanasattayavong, T.D. Anthopoulos, Solution-processable metal oxide semiconductors for thin-film transistor applications, *Chemical Society Reviews*. 42 (2013) 6910–6923.

CHAPTER 3. HYBRID PEROVSKITE BASED FIELD EFFECT TRANSISTORS

3.1 Introduction

Field effect transistor (FET) is a fundamental component in the modern digital integrated circuits. For the traditional silicon based FET, the fabrication cost, operational energy consumption and heat dissipation are the main bottlenecks. The research for novel materials with better properties and lower fabrication cost is always a key challenge [1–3]. The emergence of hybrid organic-inorganic perovskites as solution-processed semiconductors with outstanding properties have raised wide spread interest in the exploration for optoelectronic devices such as solar cells[4–7] , radiation detectors (Gamma and X-rays) and optically pumped lasers [8–10]. Despite such unprecedented progress, several riddles remain in understanding charge transport mechanisms in hybrid perovskite thin-films which were mostly deduced from photovoltaic devices[11–13]. Field-effect transistors are an excellent platform for the elucidation of such physical properties.

3.2 Motivation

Despite the intrinsic character and excellent charge transport properties of hybrid perovskites[11–13], the demonstration of room temperature operating FETs using 3D hybrid perovskite has remained elusive (more details are given in chapter 1). The ability to modulate the conductance of hybrid perovskites using a FET geometry remains a key bottleneck.

In this study, by using high quality perovskite films in combination with high k-dielectric material we developed a hybrid perovskite based FET (PFET), working at room temperature without need of illumination. Device simulations were used to better understand the performances of PFETs.

We investigated the impact of several parameters as active layer quality, channel dimension, scan rate and gate dielectric material on FET characteristics. In order to investigate the

perovskite-based FETs properties as a function of the different dielectrics materials, we measured the FET static characteristics and the capacitance values on specific devices.

3.3 Experimental section

Field effect transistors developed in this study were fabricated using the bottom-gate bottom-contact structure as illustrated in Figure 3.1 with a thin active layer of Methyl Ammonium Lead Iodide ($\text{CH}_3\text{NH}_3\text{PbI}_3$). The different steps of the process are explained in the chapter 2.

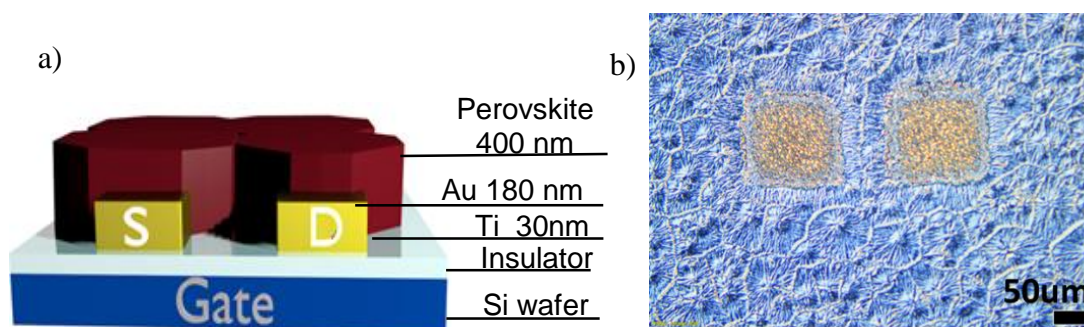


Figure 3.1. a) Schematic illustration of field effect transistor architecture. b) Optical image illustrating top view of perovskite field effect transistor. The gold electrode dimensions are $100 \mu\text{m} * 100 \mu\text{m}$.

For the dielectric layer, we used three types of insulator on heavily n-doped Si wafer:

- The first one is a 100 nm-thick thermally grown silicon dioxide layer (SiO_2 , $\epsilon_r \sim 3.9$).
- The second one is a 100 nm-thick silicon nitride (Si_3N_4 , $\epsilon_r \sim 7.5$) deposited by PECVD (plasma-enhanced chemical vapor deposition).
- The last one is a 30 nm-thick hafnium oxide (HfO_2 , $\epsilon_r \sim 23.4$) deposited by ALD (atomic layer deposition).

3.4 Characterization and analysis of structural and optical properties for large grain size perovskite based films

We characterized the properties of perovskite thin films using optical imaging and X-ray diffraction.

Optical micrographs were used to compare the morphologies between the hot-casted and as-casted perovskite thin films deposited on glass substrates (Figure 3.2). For the as-casted films, perovskite precursor was spin-coated at room temperature and then post-annealed at 100 °C for 20 min. Experimental details are given in chapter 2.

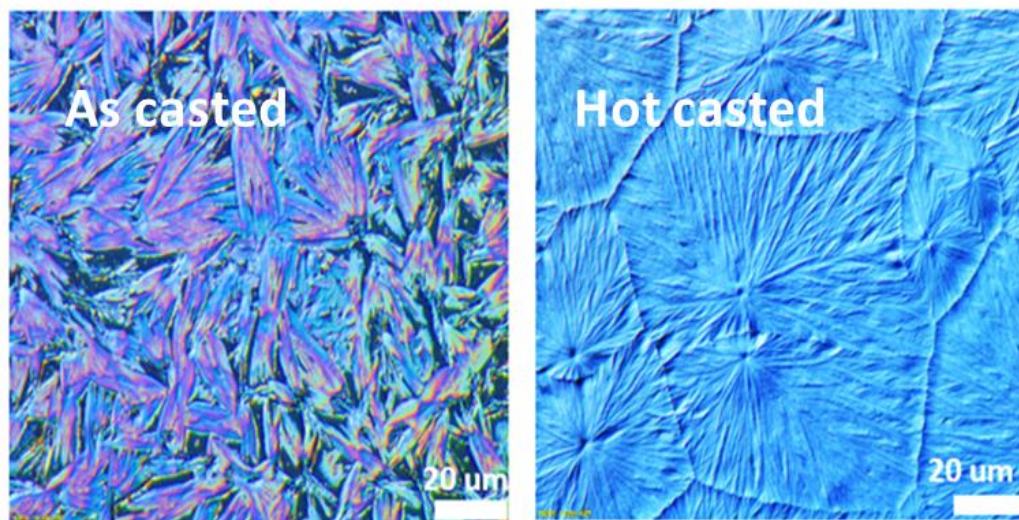


Figure 3.2. Optical micrographs of hybrid perovskite thin films deposited on glass substrates using a) as casting and b) hot casting method.

From the images, we can observe that hot-casted films exhibit larger grain size (average grain size $\sim 80 \mu\text{m}$) in comparison to the as-casted films whose morphology is totally different.

The as casted films exhibit grains with a rod-like morphology. Such films look like a network of disoriented high aspect ratio structures with bad uniformity and higher density of voids and pinholes (average length of the grain size $\sim 20 \mu\text{m}$). In contrast, the hot casted films show uniform and large grains.

We further studied the perovskite orientation in the as-casted and hot-casted thin films by performing a grazing incidence wide-angle X-ray scattering GIWAXs analysis using synchrotron wavelength as illustrated in Figure 3.3. The resulting scattering patterns reveal that similar diffraction patterns with bright rings were obtained at $q_y (\text{\AA}^{-1}) = 1$ and $q_y (\text{\AA}^{-1}) = 2$ corresponding to the (110) and (220) crystal planes.

These results are consistent with previous reports in the literature on $\text{CH}_3\text{NH}_3\text{PbI}_3$ perovskite crystal structure[14–16] indicating a crystal structure with a good crystallinity for both conditions. However, we also observed that the corresponding GIWAXS pattern of the as-casted thin films show a set of scattering spots at q_y values lower than 1 which are practically

insignificant in the hot-casted films. Moreover, these films also exhibit certain bright rings between $q_y(\text{\AA}^{-1}) = 1$ and $q_y(\text{\AA}^{-1}) = 2$ with intensities values higher than the obtained with the hot-casted films.

Thus, the above observations suggest that as-casted perovskite films provide a stronger randomness in the orientation of the crystal domains in comparison to the hot-casted perovskite thin films.

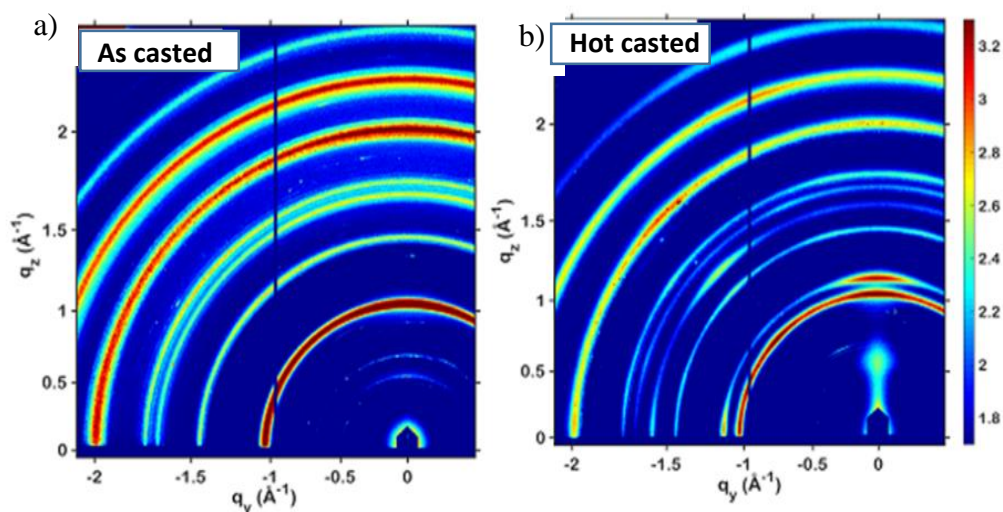


Figure 3.3. Two dimensional GIWAXS patterns corresponding to the as casted and hot casted $\text{CH}_3\text{NH}_3\text{PbI}_3$ perovskite thin films.

In order to obtain further information about the hot-casted perovskite thin films, we performed X-ray diffraction and absorbance measurements as illustrated in Figure 3.4.

The X-ray diffraction (XRD) patterns (Figure 3.4a) show sharp and strong diffraction peaks at 2θ equals to 14.1° and 28.3° corresponding to the (110) and (220) planes of the perovskite crystalline structure being in good agreement with the above observations in Figure 3.3.

Figure 3.4.b) shows the energy-dependence absorbance spectra of $\text{CH}_3\text{NH}_3\text{PbI}_3$ perovskite thin films. The band-edge absorption was observed at 1.61eV (absorption onset at 773nm) being in good agreements with previous reports [17,18].

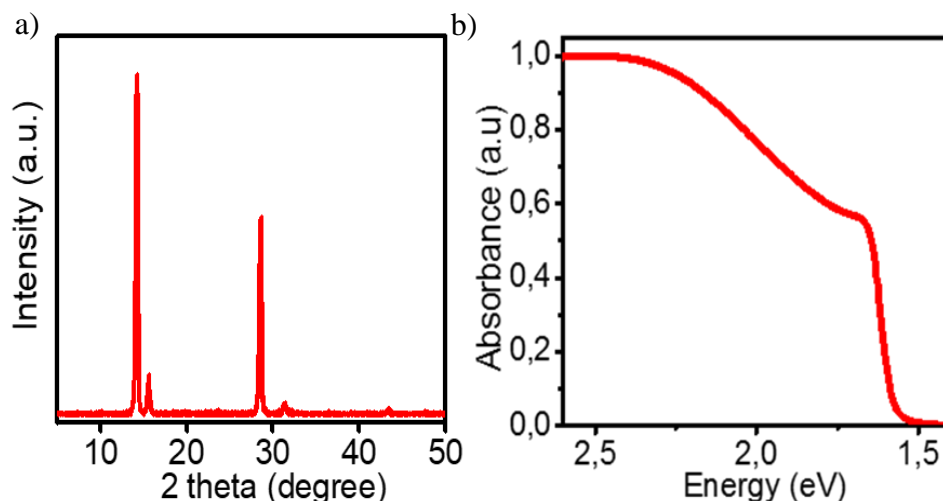


Figure 3.4. a) XRD patterns of $\text{CH}_3\text{NH}_3\text{PbI}_3$ perovskite thin films on glass substrates deposited using the hot casting technique. b) The absorbance spectra of $\text{CH}_3\text{NH}_3\text{PbI}_3$ perovskite thin films

To conclude, from the morphological analysis of hot-casted perovskite thin films we can state that such technique provides large grain-size and uniform films. From the XRD measurements, we confirm a full perovskite crystallization where PbI_2 peak (normally observed in the literature at 12.6°) was not observed. Absorbance measurements indicate a band-edge absorption at 1.61 eV.

3.5 Perovskite based FETs operating at room temperature

3.5.1 Perovskite based FETs characterization using HfO_2 as dielectric

In this study, we first fabricated field effect transistors in bottom contact geometry with a channel length (L) = 100 μm and width (W) = 100 μm using methylammonium lead iodide (MAPbI_3) thin film and hafnium dioxide (HfO_2) film as gate insulator.

The FETs characteristics and performances at room temperature in the dark are illustrated in Figure 3.5 and Table 3.1 respectively. The scan rate used for these measurements is 1V/s.

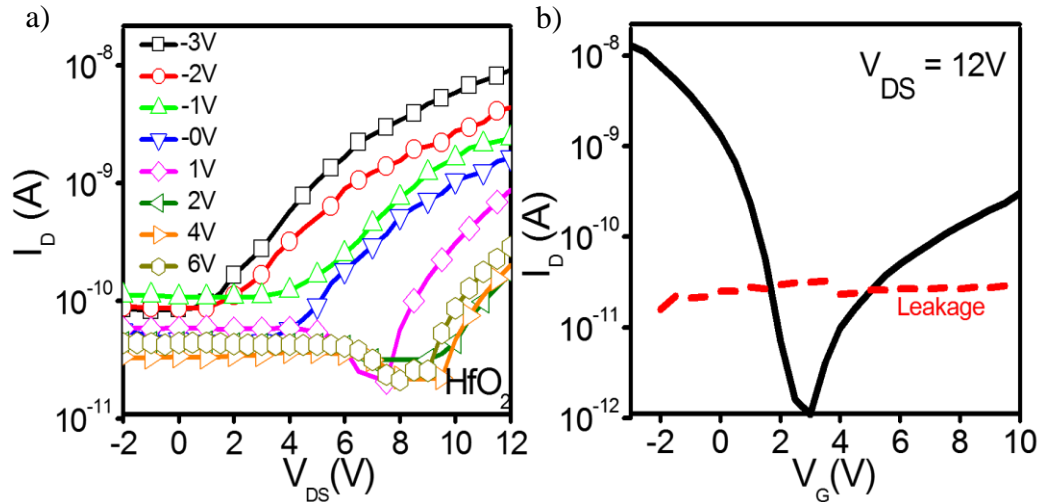


Figure 3.5. Perovskite field effect transistors fabricated using HfO_2 as gate insulator layer with a channel length (L) = 100 μm and width (W) = 100 μm . a) Output characteristics, b) Transfer characteristics (solid black line), leakage current (red dashed line).

Transport characteristics	Hole transport
μ (cm^2/Vs)	$1.6 \cdot 10^{-3}$
g_m (nA/V)	5
I_{on}/I_{off}	$1.4 \cdot 10^4$
V_{th} (V)	0.9

Table 3.1. Device parameters of perovskite-based FETs using hafnium dioxide as dielectric with a channel length (L) = 100 μm and channel width (W) = 100 μm .

The transfer characteristics, illustrated in Figure. 3.5b, clearly show a field effect modulation with a gate dependence for p type carriers with a mobility and conductance values of $1.6 \cdot 10^{-3} \text{ cm}^2/\text{Vs}$ and 5 nA/V respectively. The level of current for the n type carriers is 2 order of magnitude below, so we only analyze the holes transport.

The gate leakage current was measured and remained around 20 pA (red dashed line in Fig. 3.5a). These devices also exhibit an I_{on}/I_{off} ratio with values up to 10^4 in their transfer characteristics along with a very low threshold voltage of 0.9 V.

Figure 3.5a shows the I_D as a function of V_{DS} for different applied gate voltages ($V_G = -3V, -2V, -1V, 0V, 1V, 2V, 4V$ and $6V$). We can observe a modulation of the drain current. We could also observe a marked shift on the turn on of the I_D - V_{DS} curves with the gate voltage, however further analysis would be needed to find the origin of such interesting observation.

Even if the transistor characteristics are not good, we show that by using high quality perovskite layer in combination with a high k-dielectric as gate insulator, such as HfO_2 , we obtain a gate modulation for p-type carriers. Note that such perovskite-FET operating at room temperature has not been reported up to-date [31-33].

In order to further understand the device characteristics of perovskite based field effect transistors, device simulations were performed by Nicolò Zagni and Muhammad A. Alam. From LANL.

The device structure implemented in the simulator is schematically represented in Figure 3.6.

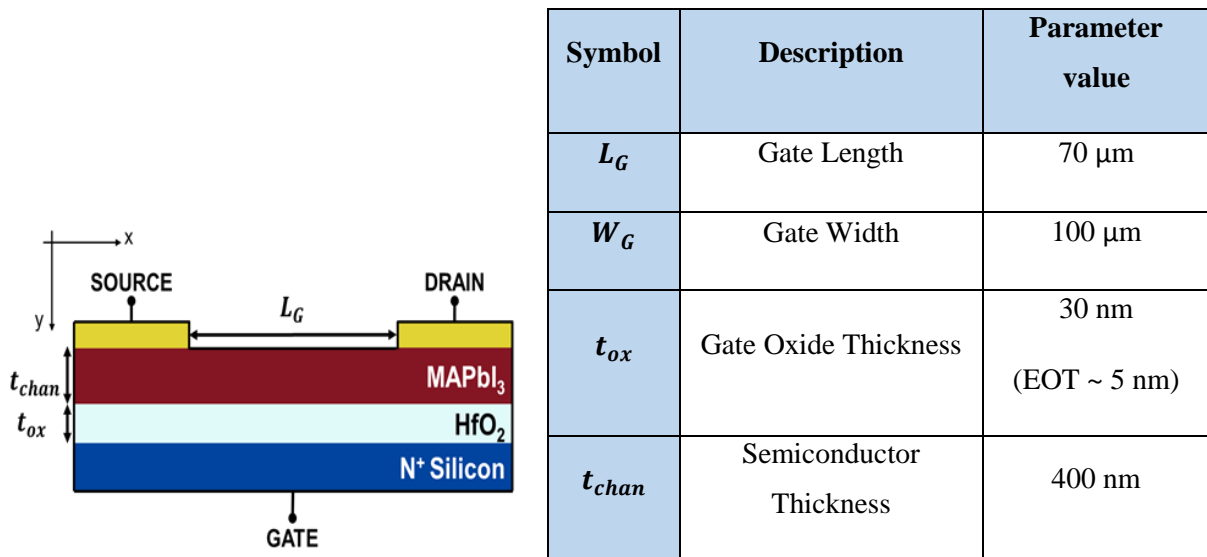


Figure 3.6. Device schematic cross-section implemented in the simulations.

Figure 3.7a shows the I_D - V_{GS} transfer characteristics for the device with a constant drain bias V_{DS} set to 6 V. The simulations predict a dominant hole current in the channel, with a threshold voltage of 4.93 V (calculated at the point of maximum transconductance g_m).

Figure 3.7b shows the I_D - V_{DS} output characteristics for the device with four different gate bias V_{GS} (see plot legend). The output characteristics are in agreement with the previous transfer characteristic, predicting no considerable change in the device behavior because the gate bias are all well below threshold.

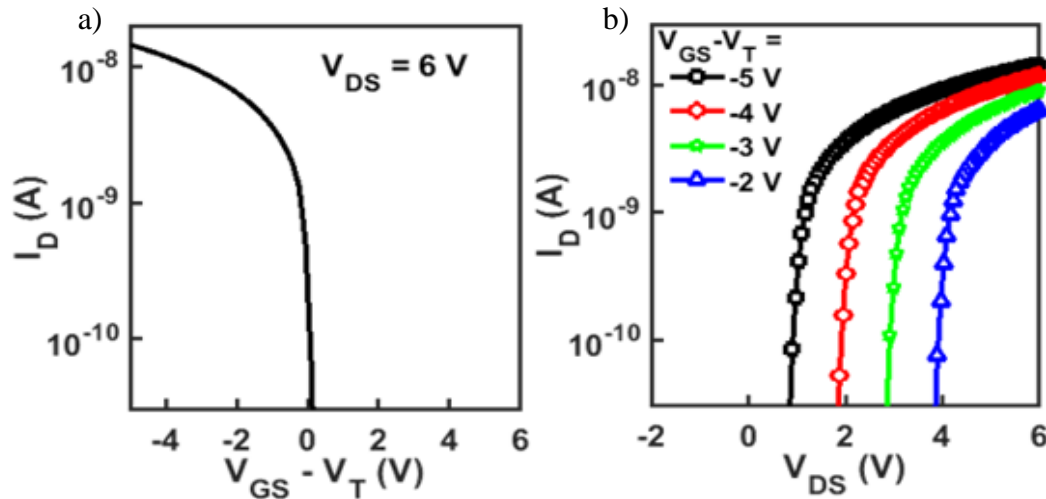


Figure 3.7. Simulation of a) transfer (I_D - V_{GS}) and b) output (I_D - V_{DS}) characteristics.

To interpret the previous results more in details, we analyze the band diagrams in Figure 3.8 plotted for three different gate bias. The band diagrams are plotted in the MaPbI_3 layer close to the source and drain contacts (on the opposite side of the gate) as illustrated in Figure 3.8a. From these band diagrams we see that the holes quasi-Fermi level (E_{FP}) is below or very near the valence band edge (E_V) at V_{GS} set to -6 V and 0 V, respectively. Conversely, at V_{GS} set to 6 V, the E_{FP} is well above the valence band thereby impeding the flow of holes in the channel. In this latter case, although the electron quasi-Fermi level (E_{FN}) is close to the conduction band edge (E_C), given the relative high Schottky barrier with E_C at the S/D contacts, no flow of electrons in the channel is observed even at high positive gate bias. Similar considerations apply for the band diagram in Figure 3.8b, plotted in in the MaPbI_3 layer close to the interface with the HfO_2 layer.

Figure 3.8c shows the band diagram at equilibrium conditions in the middle of the device, crossing all the regions. Given the relatively thin semiconductor body (400 nm), the electrostatic potential that builds up as a consequence of the work function difference between the silicon substrate and the perovskite layer depletes the semiconductor region. This leads to a free hole density much lower than the doping (10^{16} cm^{-3}) indicating that the device is fully depleted.

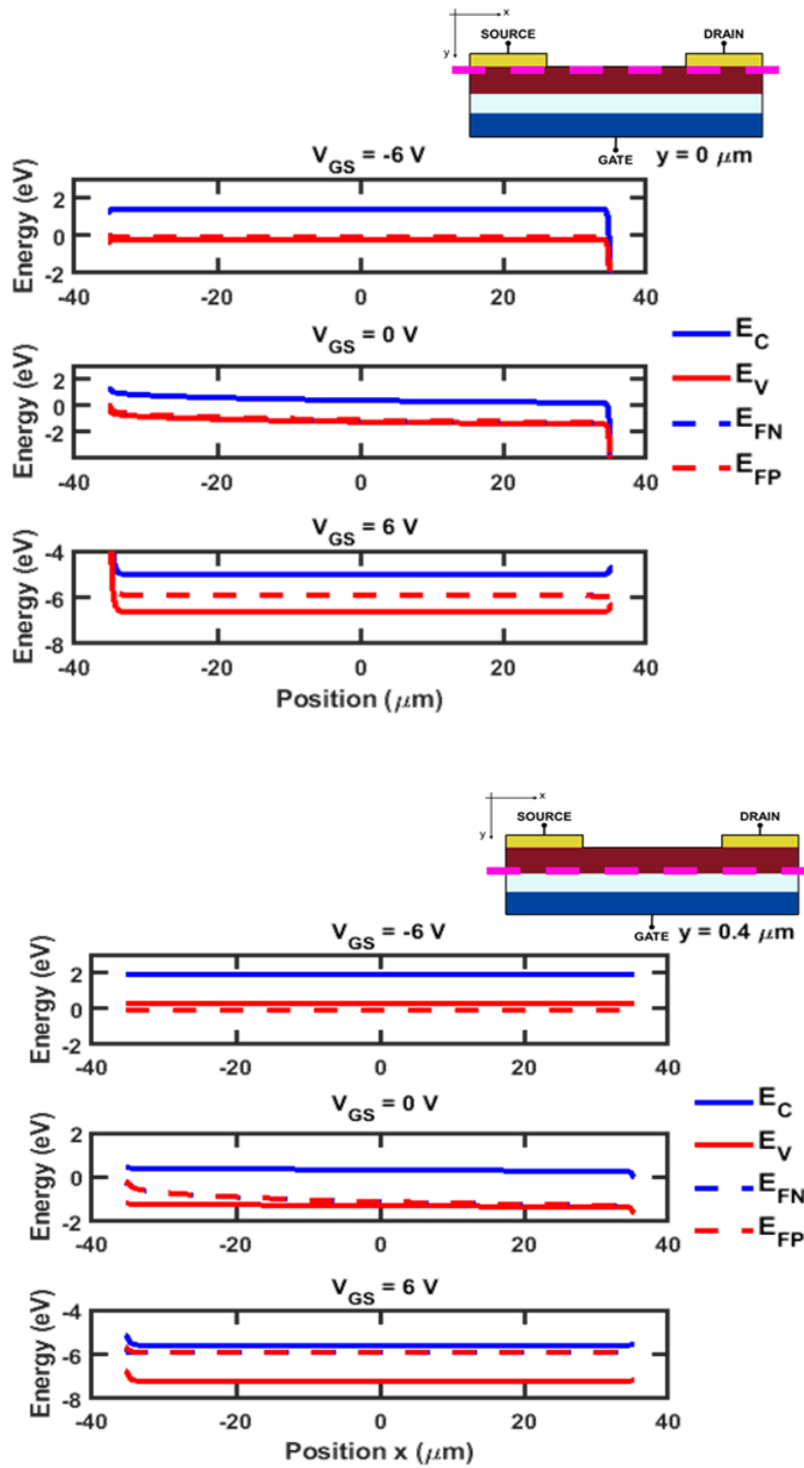


Figure 3.8. a) Band diagram close to the source and drain contacts (on the opposite side of the gate). b) Band diagram close to the interface between the perovskite and the HfO_2 layer.

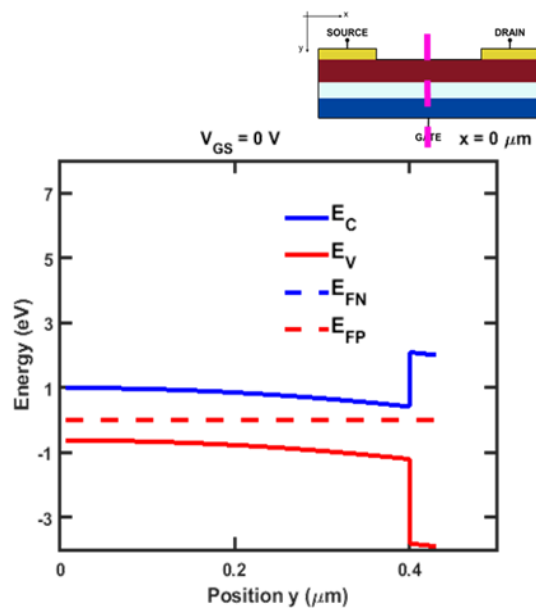


Figure 3.8. c) Band diagram at equilibrium in the middle of the device.

Thus, the device simulations can help to explain the characteristics obtained in Figure 3.5 with perovskite as active layer in field effect transistors.

In this section, by growing highly crystalline thin film perovskite with high k -dielectric such HfO_2 we demonstrated operational perovskite based FETs at room temperature [29-31]. Device simulations have been developed to show the gate modulation in this device. The experimental transfer characteristics show a p-type transport like in the simulation. The final level of current I_D is in the same range. The evolution of the current and the threshold voltage are dependent on the interface charges, traps which are not taken into account in the simulation.

In the next section, we illustrated the performances obtained with PFETs after consecutive measurements on these devices.

3.5.2 Perovskite based FETs characteristics after consecutive cycles of measurements

In order to further analyze the device performances of perovskite based FETs, we carried out stability tests by performing consecutive I_D - V_G measurement cycles (aging bias) at room temperature in the dark.

Figure 3.9a shows the transfer characteristics of perovskite based FET before and after aging. The values of the source and drain current at $V_G = 10\text{V}$ ($V_{DS} = 12\text{V}$) for each cycle of

measurement are illustrated in Figure 3.9b. Table 3.2 provides the devices performances of perovskite-based FETs obtained before and after aging.

Such aging experiment consists in continuously biasing the transistor, scanning V_G from -3 V to 10 V for $V_{DS} = 12$ V until getting reproducible characteristics. Such aging lasts around 20 minutes.

Observation and comparison of transfer curves after consecutive measurements cycles leads to the following observations; (i) after aging, the maximum drain current increases then remains quasi constant. (ii) comparable electrons and holes currents for the transfer characteristics are measured (iii) slight decrease in the maximum hole current (iv) much weaker gate modulation.

The transfer characteristics of perovskite FETs after consecutive cycles of measurements illustrated in Figure 3.9a, clearly show a dramatic enhancement in the gate modulation for n-type carriers leading to an ambipolar FETs characteristics with gate dependence for n and p-type carriers.

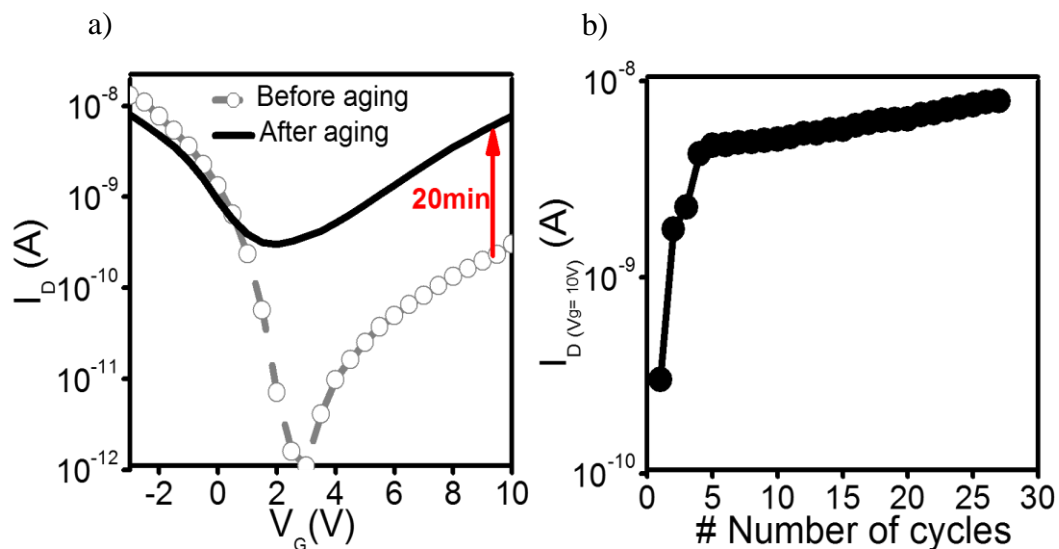


Figure 3.9. a) Transfer characteristics of perovskite-based FETs before and after consecutive measurements cycles ($V_{DS} = 12$ V). b) Drain current at $V_G = 10$ V and $V_{DS} = 12$ V as a function of measurement cycles.

Transport characteristics	Before aging		After aging	
	Hole transport	Electron transport	Hole transport	Electron transport
μ (cm ² /Vs)	1.6*10 ⁻³	1*10 ⁻⁵	8*10 ⁻⁴	3.38*10 ⁻⁴
G _m (nA/V)	5	0.014	2.4	1
I _{on} /I _{off}	1.4*10 ⁴	2.3*10 ²	25	5*10 ¹
V _{th} (V)	3	3	5.7	2.7

Table 3.2. Device parameters of perovskite-based field effect transistors before and after aging.

The conductance and mobility values for n-type carriers were drastically increased from 0.014 nA/V to 1 nA/V and from 1*10⁻⁵ cm²/Vs to 3.38*10⁻⁴ cm²/Vs respectively. This observation is the result of the rapid increase of the maximum drain current at V_G = 10 V after 5 cycles and then slowly increases during 25 cycles as illustrated in Figure 3.9b.

The enhancement for electrons carriers could be explained by the interface trap/defects which may induce the electron current contributing to the gate modulation for n-type carriers. As our structure is based on Schottky barriers, it is sensitive to the difference of work function between the channel and source/drain electrodes. If there is a mismatch between these work function, we can get transistor with unipolar behavior. By aging the devices, we get ambipolar behavior indicating a better matching in the work functions. Such phenomenon is not obtained in literature for perovskite transistors operating at room temperature in dark conditions. It should be noted that it is possible to get back to the starting point, FET with p-type transport characteristics by leaving the device at rest for at least 1 hour.

We observed a decrease on the gate modulation for p-type carriers. The conductance and mobility values for p-type carriers was slightly decreased from 5 nA/V to 2.4 nA/V and from 1.6*10⁻³ cm²/Vs to 8*10⁻⁴ cm²/Vs respectively. The I_{ON}/ I_{OFF} ratio is also decreased up to three orders of magnitude leading to very low values around 25.

The hysteresis of our devices was examined by analyzing the I_D-V_G curves with scan from negative to positive ([1.], solid line) and then from positive to negative ([2.], dashed-line) using different scan rates (3 V/s, 1 V/s, 0.3 V/s and 0.1 V/s) as illustrated in Figure 3.10 (these measurements were extracted after consecutive cycles of biasing/measurements).

The observed “butterfly” hysteresis between forward and reverse characteristics can be attributed to the gate voltage induced migration of ions or charged defects in the perovskite [27-28].

In contrast, at slower scan speeds conditions, such 0.1 V/s, we observed a slight decrease in the hysteresis area but however the measured drain current is also decreased suggesting a weaker gate modulation (Figure 3.10).

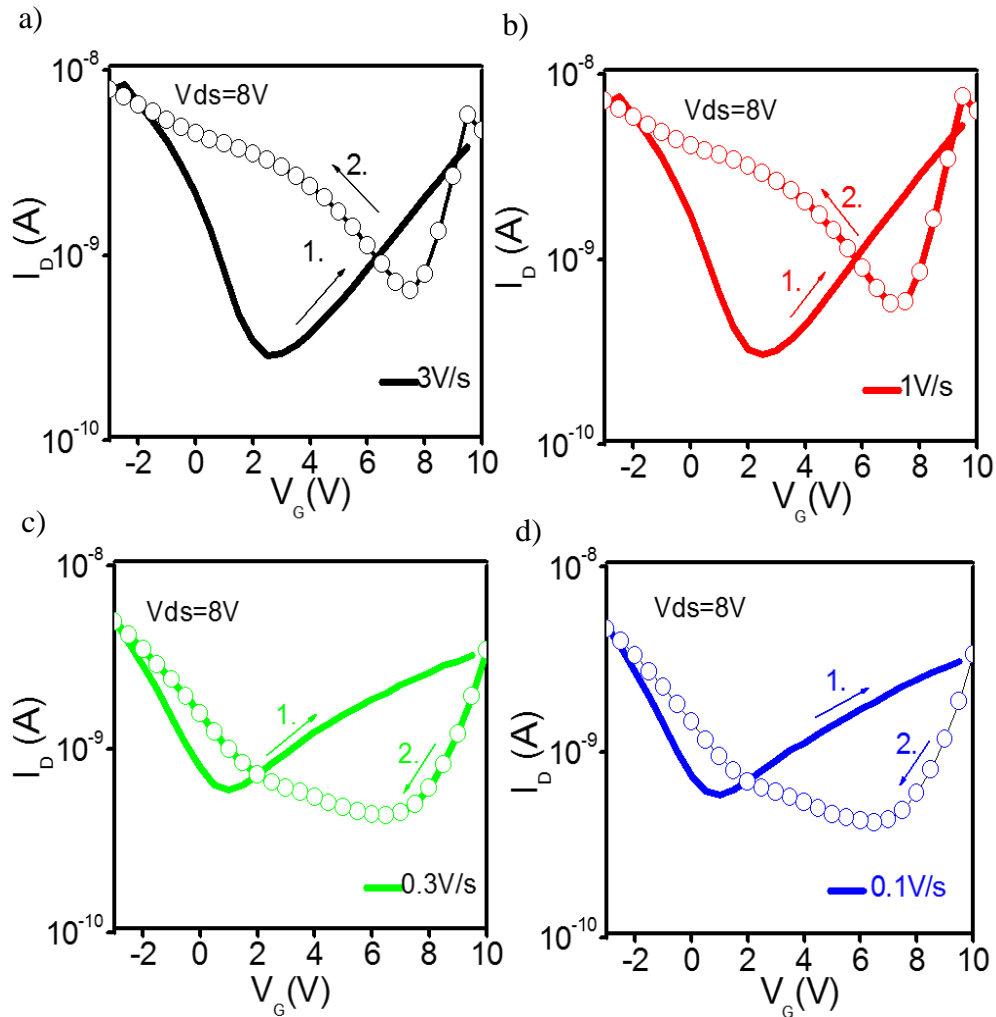


Figure 3. 10. Transfer characteristics of perovskite field effect transistors as a function of scan speed in the dark at room temperature.

To quantify the above observations, we plotted the p and n-type current (Fig. 3.11a), Ion/Ioff ratio (Fig. 3.11b), threshold voltage (Fig. 3.11c-d), maximum transconductance value for holes and electrons carriers (Fig. 3.11e-f), hysteresis loop area (Fig. 3.11g) as a function of scan speed for the the forward and reverse scan.

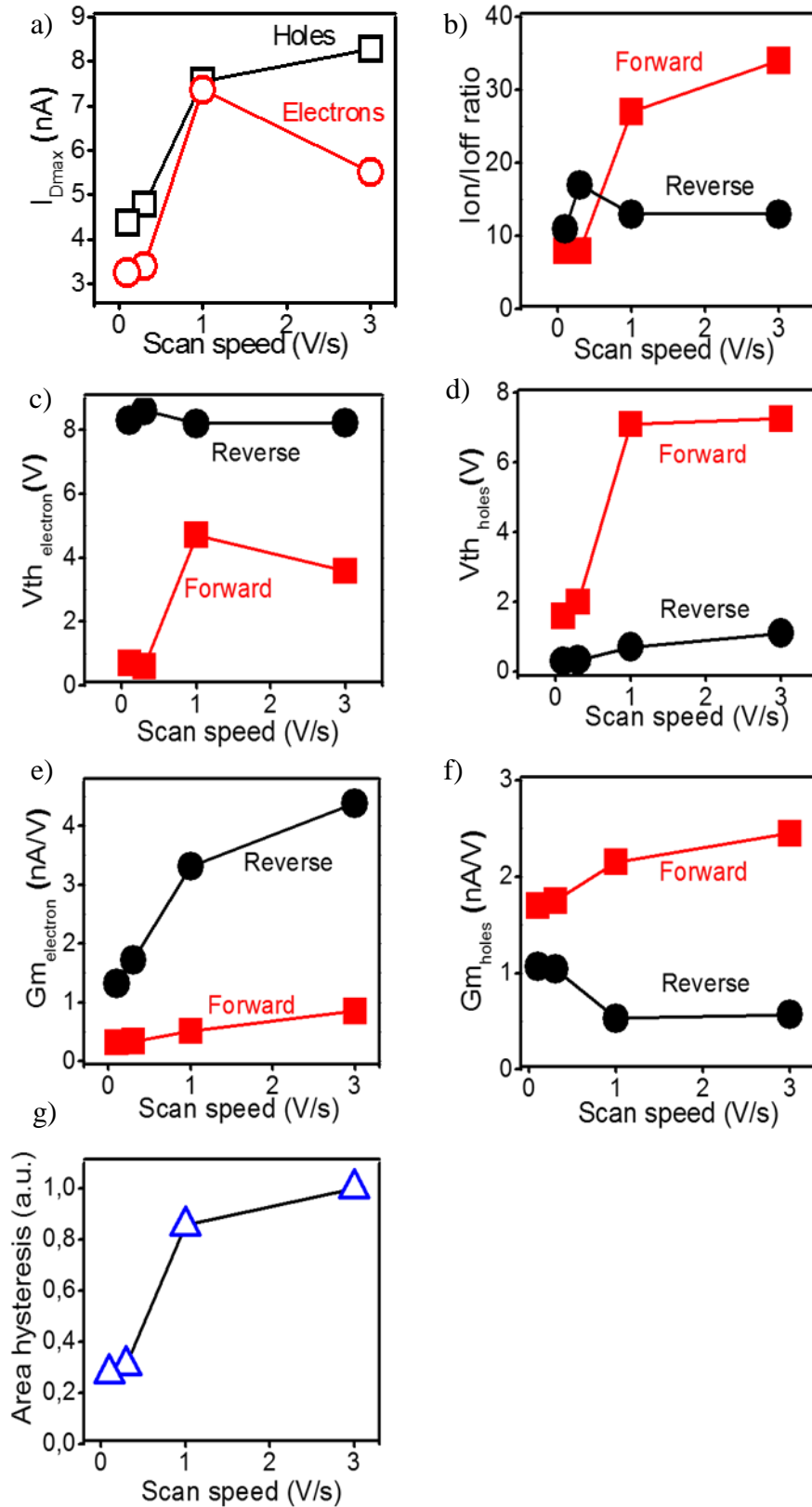


Figure 3.11. Effect of scan speed on different parameters for perovskite field effect transistor a) Drain current at $V_G = -3$ V (holes) and $V_G = 10$ V (electrons), b) Ion-Ioff ratio, c-d) Threshold voltage, e-f) Transconductance for electron/hole carriers and g) Area hysteresis.

The understanding of the transport properties in perovskite films are clearly difficult to analyze due to the device instabilities and the frequency domain is small due to low current acquisition. By measuring the area under the loop on the I_D - V_G curves to extract the hysteresis area, we observed a significant increase in the area of the loop as a function of the scan rate.

Thus, faster scan gives better performances than slower scans in the device performances of perovskite based FETs being in good agreement with previous reports of perovskite solar cells in the literature [19–21]. This observation can be interpreted as the reduction of the ionic screening with the faster scan rates. As the scan rate is slow, more the ion displacement is important and consequently the screening effect which reduces the total current. Although, more research is needed to explain this phenomenon, our hypothesis is that the contribution of the interface trap defects, excess ions or interstitial defects (iodide or methylammonium) is higher at low scans leading to a reduction on the device performances.

To conclude, in this section, by growing highly crystalline thin film perovskite with high k -dielectric such as HfO_2 we demonstrated operational perovskite based FETs at room temperature [31-33]. After consecutive cycles of measurements, we obtained ambipolar transport where the perovskite's fermi energy can be successfully modulated by gate voltage allowing both electron and hole transport in the conduction band and valence band respectively.

3.5.3 Channel length variation effect on lead iodide perovskite FETs

Here, we study the channel length variation effect on the performances of perovskite based field effect transistors.

First, we fabricated a field effect transistor in bottom contact geometry with different channel lengths (L) = 70 μm , 100 μm and 150 μm using MAPbI_3 thin films and HfO_2 as dielectric. The devices are in the same configuration with the same perovskite film thickness, comparable crystalline quality and identical channel width (W) = 100 μm .

The transfer and output characteristics at room temperature in the dark after consecutive cycles of measurements are illustrated in Figure 3.12 (scan rate ~ 1 V/s).

As previously observed, these measurements clearly show a field effect modulation with comparable drain current values for both p and n-type carriers exhibiting ambipolar transport characteristics regardless the channel length.

Observation and comparison of transfer characteristics with different channel lengths (Figure 3.12) indicate that perovskite-based FETs with shorter channel length, such as $L \sim 70 \mu\text{m}$ (Figure 3.12a-b), exhibit stronger gate dependence with very low hysteresis. The output characteristics obtained do not respect the classical behavior, we don't obtain a saturation. If we increase the V_{DS} polarization above 8 V the device is damaged.

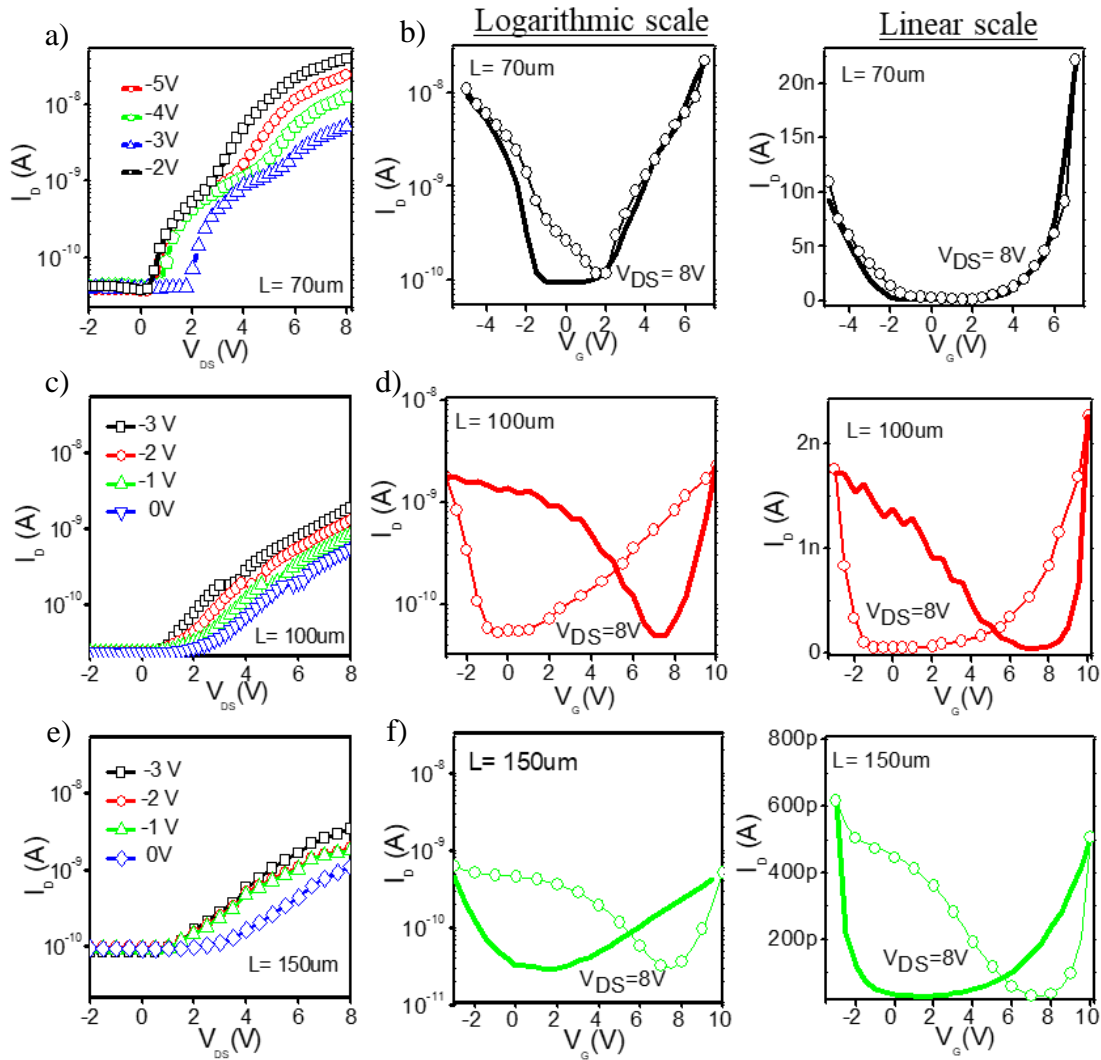


Figure 3.12. Output (for p -type carriers) and transfer characteristics (logarithmic and linear scale) of perovskite field effect transistors with different length channels. Solid and dotted lines in the I_D - V_G curves illustrate the forward and reverse scans. a-b) $70 \mu\text{m}$; c-d) $100 \mu\text{m}$ and e-f) $150 \mu\text{m}$.

However, by increasing the channel length from $70 \mu\text{m}$ to $150 \mu\text{m}$, a significant deterioration is observed in the transfer characteristics as well as for output characteristics. Larger channel length induce a strong “butterfly” hysteresis as illustrated in Figure 3.12c-f. This hysteresis is

a major barrier for using such devices in practical applications. Moreover, the maximum drain current measured is considerably decreased in comparison to shorter lengths (Figure 3.12).

The above observations highlight that the modulation of carriers strongly depends on the channel area as previously reported in FETs [29]. By increasing the channel length, the charge trapping/recombination rate is increased due to the higher number of defects across the channel resulting in a smaller gate modulation.

As previously reported, film surface, bulk of the grain and the boundary between are considered as the three primary spatial locations of defects on perovskite thin films. It has been reported that this fact plays a critical role on the perovskite devices performances [5,6,15]. Thus, by increasing the channel length dimension on FETs the number of these defects and grain boundaries across the channel will be increased inducing higher charge recombination rate resulting in lower device performances.

It should be noted that in order to further optimize the device performances, we tried to use smaller channel length ($L \leq 50 \mu\text{m}$). However, due to the high wettability between perovskite solution and the gold electrodes, we did not succeed in obtaining operational devices due to the limitation on the fabrication process.

Finally, by using a relatively small channel length ($L = 70 \mu\text{m}$) and HfO_2 as dielectric, we succeed in obtaining a gate modulation for 3D perovskite-FET at room temperature with a very low hysteresis. Transfer characteristics plotted in linear scale (Figure 3.12b) highlight the relative small hysteresis for ($L = 70 \mu\text{m}$). Such behavior for perovskite transistor has not been reported up to-date.

In the next section, in order to understand the dielectric role on perovskite based field effect transistors we use three different materials as gate insulators.

3.5.4 Impact of gate insulator on lead iodide perovskite based FETs

Here, we study the effect of the dielectric material on perovskite-based FETs by using: silicon dioxide (SiO_2 , $\epsilon \sim 3.9$, $t \sim 100 \text{ nm}$, thermal growth), silicon nitride (Si_3N_4 , $\epsilon \sim 7.5$, $t \sim 100 \text{ nm}$, PECVD), and hafnium dioxide (HfO_2 , $\epsilon \sim 23.5$, $t \sim 30 \text{ nm}$, ALD) respectively.

These devices were fabricated in bottom contact geometry with the same perovskite films thicknesses and comparable crystalline quality. Channel dimensions were chosen according to last results: $L = 70 \mu\text{m}$ and $W = 100 \mu\text{m}$.

The transfer and output characteristics of perovskite-based FETs with different dielectrics are illustrated in Figure 3.13. These measurements were carried out in the dark at room temperature (scan rate $\sim 1 \text{ V/s}$). These measurements were performed after consecutive cycles / aging which are needed to reach a stable regime where the device performances remain stable without any appreciable degradation or variation.

As shown on figure 3.13, main results highlight:

- no transistor effect could be obtained by using SiO_2 as dielectrics. The SiO_2 /perovskite system looks like a memory device with a huge hysteresis [30].
- Unipolar transistor could be obtained by using Si_3N_4 . Only a weak n-type channel was formed by tuning the gate voltage with a low hysteresis.
- Ambipolar transistor could be obtained using HfO_2 as previously shown. We measured a balanced electron and hole transport for the HfO_2 based FETs represented by the fairly symmetric transfer characteristics with comparable I_D value for both n- and p-type carrier with a very low hysteresis.

Such observations show that dielectric material is fundamental to get functional devices. As perovskite layers deposited on these dielectrics show comparable crystalline quality, one can suppose that defects interface play a critical role to get working transistors. For the same source-drain voltage ($V_{DS} = 8\text{V}$), we observed an increase in the source and drain current by up to an order of magnitude as a function of the gate for HfO_2 -based FETs.

To quantify and to better understand the above measurements, we calculate the EOT, maximum transconductance reverse and forward, threshold voltage and relative maximum hysteresis (Table 3.3).

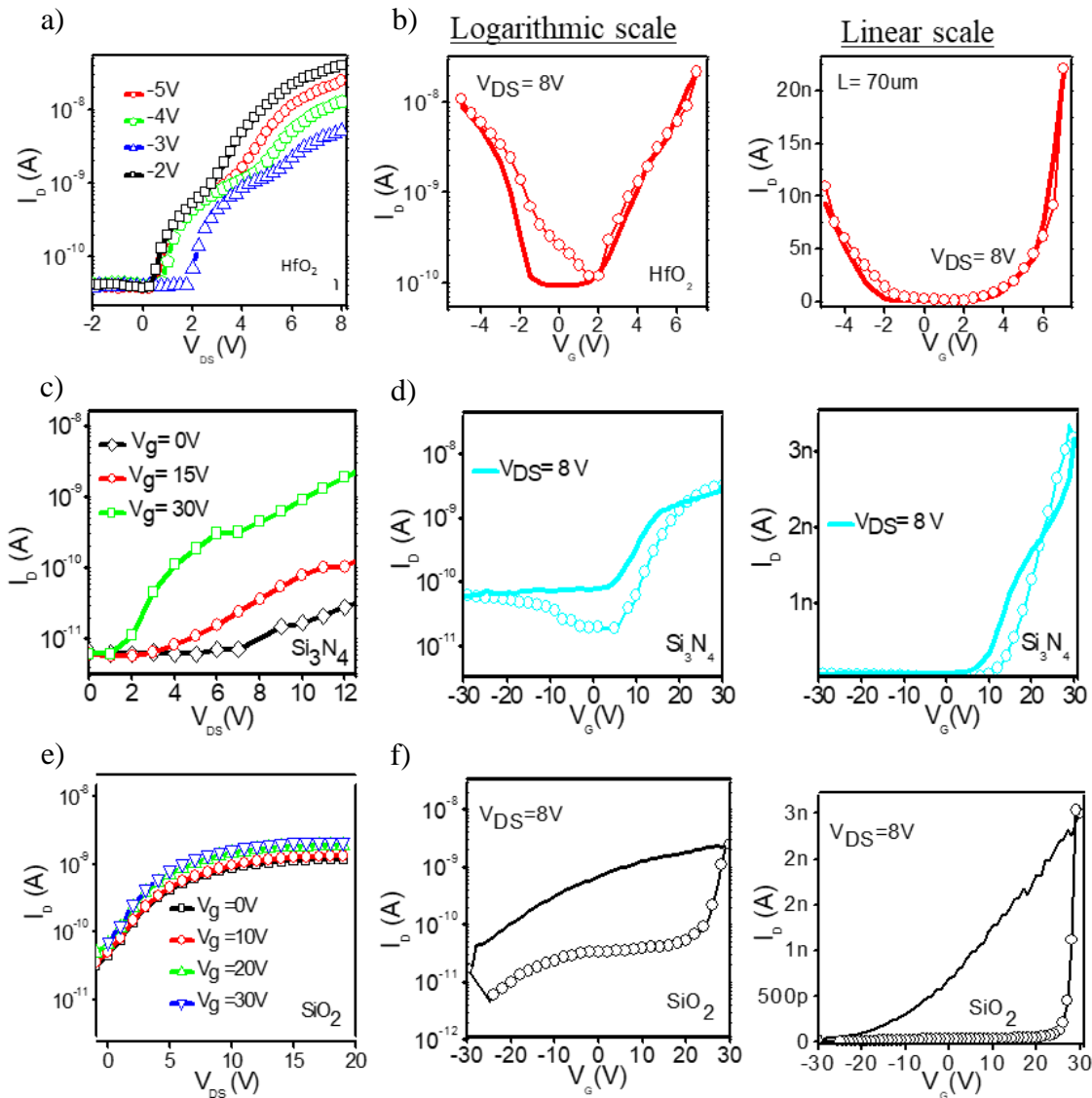


Figure 3.13. Output (for *p*-type carriers) and transfer (logarithmic and linear scale) characteristics of a perovskite field effect transistor using different dielectrics as insulators. a-b) HfO₂; c-d) Si₃N₄ e-f) SiO₂.

EOT (equivalent oxide thickness) is an indicator of how thick a silicon oxide film would need to be to produce the same effect as the corresponding high- κ material described as follows in Equation 3.1

$$EOT = t_{HfO_2} \frac{\kappa_{SiO_2}}{\kappa_{HfO_2}} \quad (\text{Equation 3.1})$$

Dielectric	SiO₂	Si₃N₄	HfO₂
EOT	100	52	5
G_m (nA/V) Forward	Non relevant	0.13	Hole transport – 3.4 Electron transport – 2.6
G_m (nA/V) Reverse	Non relevant	0.19	Hole transport – 2.6 Electron transport – 3
μ(cm²/Vs) Forward	Non relevant	1.3x10 ⁻⁴	Hole transport – 1x10 ⁻³ Electron transport – 6.6x10 ⁻⁴
μ(cm²/Vs) Reverse	Non relevant	1.3x10 ⁻⁴	Hole transport – 1x10 ⁻³ Electron transport – 1x10 ⁻³
V_{th} (V) Forward	Non relevant	8.2	Hole transport – 2.3 Electron transport – 3.2
V_{th}(V) Reverse	Non relevant	13.3	Hole transport – 1.8 Electron transport – 1.8

Table 3.3. Device parameters of perovskite field effect transistor using different dielectrics as insulators: SiO₂, Si₃N₄ and HfO₂.

From the analysis of the device parameters illustrated in the above table, we observed an enhanced gate-induced modulation as the value of the equivalent oxide thickness was decreased. By using high-k dielectrics, such as HfO₂, the conductance and mobility values were dramatically improved by up to one order of magnitude. We could also observed a huge difference on the threshold voltage, where high-k dielectrics as gate insulators on PFETs allows to obtain very low threshold voltages of ~ 1.8 V.

By contrast, low-K dielectrics such as Si₃N₄, did not lead to any appreciable field effect modulation for the p-type carriers exhibiting only a relatively weak n-type transport characteristics suggesting that the technique used to deposit gate insulator may play an important role in terms of interface defects leading to a defect-induced carriers. This is in good agreement with previous reports in the literature confirming that the energy level of perovskites strongly depends on the nature of the substrates which can introduce gap states and consequently the perovskite film formation and morphology [34].

We also examined the hysteresis by analyzing the I_D-V_G curves (Figure 3.13) by using the next formula (Equation 3.2):

$$\text{Relative hysteresis} = \frac{\text{maximum ID curve} - \text{minimum ID curve}}{\text{minimum ID curve}} \quad (\text{Equation 3.2})$$

The curves obtained for each insulator, SiO₂, Si₃N₄ and HfO₂ are illustrated in Figure 3.14.

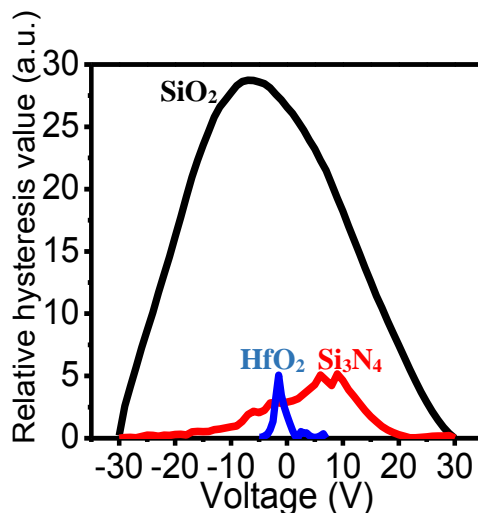


Figure 3.14. Relative hysteresis value as a function of voltage for different dielectrics.

From these measurements, we observed a significant decrease in the relative hysteresis values by using hafnium dioxide as insulator exhibiting a very low value in comparison to silicon nitride or silicon dioxide (Figure 3.13). This observation is also visible in Figure 3.13b where I_D-V_G curve does not show any appreciable change between the forward and reverse scan.

Charge density on the system is increased by using high-K dielectric. In order to understand the behavior of the devices, we have investigated the static capacitance of perovskite-based FETs by using low and high-k dielectrics as gate insulator. Here, we employ metal-insulator-semiconductor (MIS) configuration (Figure 3.15a) using n-type silicon as contact, perovskite layer as the semiconductor body and compared SiO₂ and HfO₂ as dielectrics.

First, we measured the capacitance-frequency spectra (C-f) for these devices (Figure 3.15b). From the spectra, we observed that the capacitance values obtained show negligible change with the input frequency, suggesting that the devices are well-behaved capacitors with negligible leakage current (shunt resistance) through the gate regardless the dielectric.

The total capacitance in the system (C_{perovskite}+ C_{oxide}) was calculated using the Equation 3.3:

$$C_{total} = \frac{C_{perovskite} * C_{oxide}}{C_{perovskite} + C_{oxide}} \quad (\text{Equation 3.3})$$

where C is determined by

$$C = \varepsilon * \varepsilon_0 \frac{A}{d} \quad (\text{Equation 3.4})$$

With the geometry used, we found: $C_{SiO_2} = 8.85 * 10^{-10}$ F, $C_{HfO_2} = 2.77 * 10^{-8}$ F and $C_{perovskite} = 2.21 * 10^{-9}$ F. Note that for $C_{perovskite}$ dielectric constant was chosen to 25 according to the literature.

Following the above equations, we found that the total capacitance in the system ($C_{perovskite} + C_{oxide}$) using HfO_2 as insulator is dominated by the $C_{perovskite}$:

$$C_{totalSiO_2system} = \frac{2.21 * 10^{-9} F * 8.85 * 10^{-10} F}{2.21 * 10^{-9} F + 8.85 * 10^{-10} F} = 6.32 * 10^{-10} F$$

$$C_{totalHfO_2system} = \frac{2.21 * 10^{-9} F * 2.77 * 10^{-8} F}{2.21 * 10^{-9} F + 2.77 * 10^{-8} F} = 2.05 * 10^{-9} F$$

Thus, we found that the total capacitance in the system ($C_{perovskite} + C_{oxide}$) is dominated by the $C_{perovskite}$ by using high-k dielectric constant.

Next, we measure the capacitance-DC voltage (C-V) at high frequency $f=100$ KHz (overplayed after resistance correction) to examine the carrier density in the perovskite layer using SiO_2 and HfO_2 as dielectric (Figure 3.15c).

In SiO_2 device, we observed that the capacitance spectra do not show any modulation, which is consistent with the absence of gate modulation in fabricated device (Figure 3.13e-f).

In sharp contrast, with HfO_2 as the dielectric in the MOS capacitor, we observe a capacitance change with gate voltage in classical regimes for a FET: accumulation, depletion and inversion. The results indicate that the MOS capacitor fabricated with HfO_2 as dielectric can successfully accumulate electrostatic p-type charge in the perovskite channel ($V_G < -4$ V), which can attain strong inverse region by doping n-type carrier in the perovskite with large positive gate voltage.

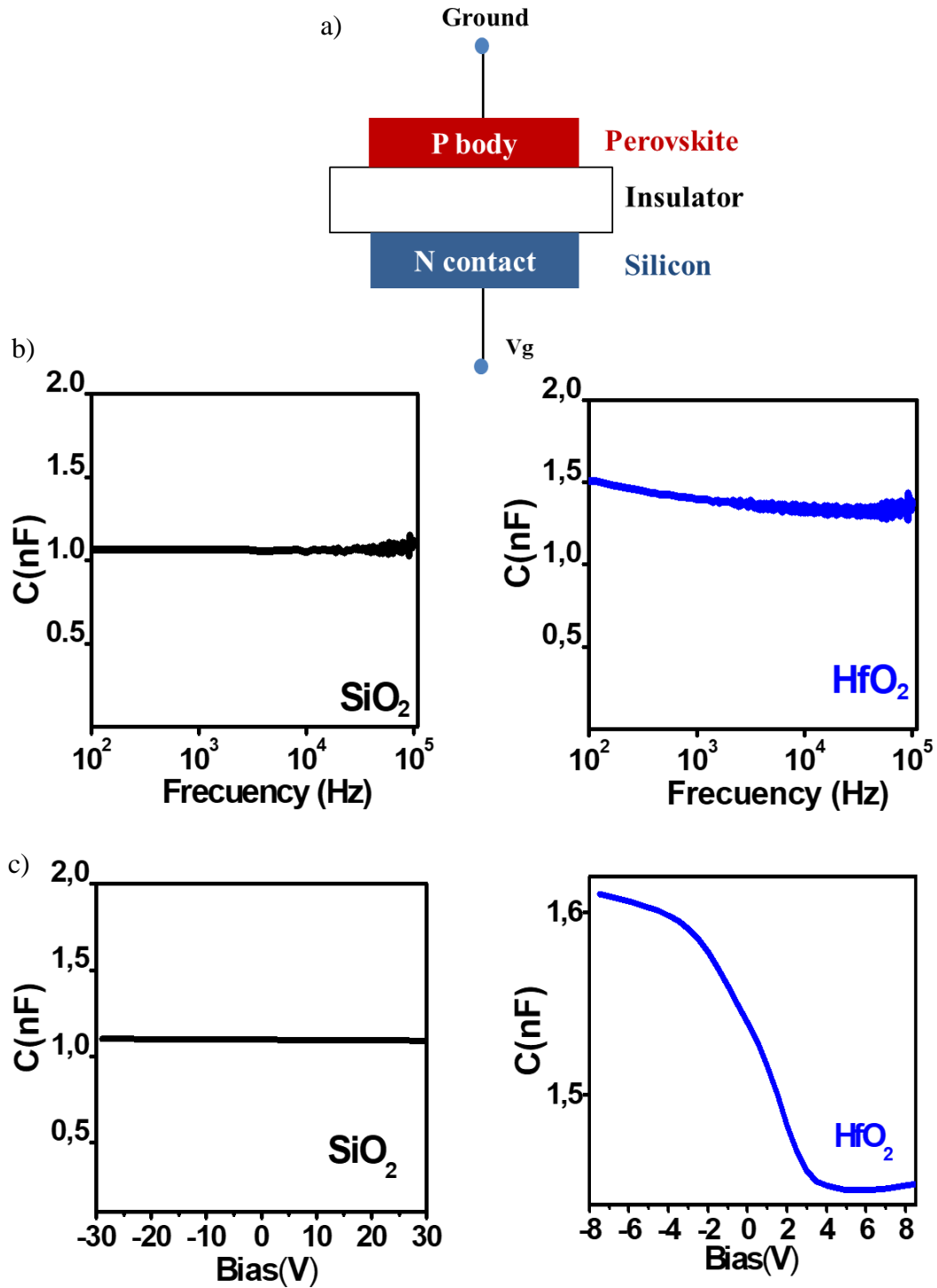


Figure 3.15. a) MIS capacitance structure used in this study. b) capacitance-frequency and c) capacitance-voltage characteristics using SiO_2 and HfO_2 as dielectrics.

Finally, the charge density (Q) values for each insulator (SiO_2 , HfO_2) were extracted from the capacitance-voltage measurements. The charge density value was obtained from the C-V characteristics in Figure 3.15 using the Equation 3.5.

$$Q_{ACC} = \int_0^1 C dv \quad (\text{Equation 3.5})$$

The calculation shows an increase in the charge density with the dielectric constant with values of $\approx 1.6 \times 10^{11}$ for silicon dioxide and 2.5×10^{11} for hafnium dioxide respectively.

As charge density on the system is increased by using high-K dielectric, the charged site vacancies can be passivated and consequently ambipolar field effect transistors could be achieved. It should be noted that the charge density values obtained are a rough estimation of the actual charges in the system which is strongly affected and reduced by the defects in the channel.

To conclude this section, high k-dielectric as gate insulator was required to enhance the charge density and thereby the channel conductance which effectively increases the capacitance of the device leading to higher electrostatic charge density for a small applied gate voltage.

We emphasize that high quality perovskite films along with high-K materials as insulator were the key parameters in this work to obtain operational hybrid perovskite FETs.

3.6 Conclusion

By growing highly crystalline perovskite thin film with proper choice of gate dielectric layer, we obtain perovskite based field effect transistors operating at room temperature, in the dark. Such results are not discussed in the literature.

Moreover, we obtain ambipolar transport where the p and n-type carriers can be successfully modulated with the gate by using HfO_2 as dielectric. Analysis of the FET characteristics and correlated capacitance measurements as a function of different dielectrics, reveal that the fundamental challenge for perovskite-based FETs was the screening of the gate electric-field by ionic vacancies. Thus, by using high-k dielectric as gate insulator we were able to increase the charge density on the system which can easily the charged site vacancies, which hindering the charge modulation, contributing thus to an enhance in the carrier modulation achieving p-type field effect transistors.

Our results contribute to overcome a key issue that had prevented the demonstration of hybrid perovskite-based FETs. However, deep investigations are still needed to fully understand and control main phenomena highlighted in this chapter:

- All fabricated transistors show hysteresis. Even if this latter can be very low, one has to investigate a way to suppress it.
- Continuous cycling of biasing leads to ambipolar transistor with HfO₂ insulator. This phenomenon, not fully explained, is a barrier to overcome to get stable transistors.
- The devices do not show a classical FET behavior: no saturation is observed in the output characteristics. The transfer characteristics using HfO₂ show an exponential increase of the current before breakdown.

In the next chapter, we used mixed cation perovskite as active layer in FETs. This material has been recently used in the literature as a promising alternative to improve the thermal stability of 3D perovskite materials.

3.7 References

- [1] F. Meillaud, M. Boccard, G. Bugnon, M. Despeisse, S. Hänni, F.-J. Haug, J. Persoz, J.-W. Schüttauf, M. Stuckelberger, C. Ballif, Recent advances and remaining challenges in thin-film silicon photovoltaic technology, *Materials Today*. 18 (2015) 378–384.
- [2] J. Werner, R. Bergmann, R. Brendel, The challenge of crystalline thin film silicon solar cells, in: *Festkörperprobleme 34*, Springer, 1995: pp. 115–146.
- [3] S. Almosni, A. Delamarre, Z. Jehl, D. Suchet, L. Cojocaru, M. Giteau, B. Behaghel, A. Julian, C. Ibrahim, L. Taty, others, Material challenges for solar cells in the twenty-first century: directions in emerging technologies, *Science and Technology of Advanced Materials*. 19 (2018) 336–369.
- [4] M.M. Lee, J. Teuscher, T. Miyasaka, T.N. Murakami, H.J. Snaith, Efficient hybrid solar cells based on meso-superstructured organometal halide perovskites, *Science*. (2012) 1228604.
- [5] H. Zhou, Q. Chen, G. Li, S. Luo, T. Song, H.-S. Duan, Z. Hong, J. You, Y. Liu, Y. Yang, Interface engineering of highly efficient perovskite solar cells, *Science*. 345 (2014) 542–546.
- [6] W. Nie, H. Tsai, R. Asadpour, J.-C. Blancon, A.J. Neukirch, G. Gupta, J.J. Crochet, M. Chhowalla, S. Tretiak, M.A. Alam, H.-L. Wang, A.D. Mohite, High-efficiency solution-processed perovskite solar cells with millimeter-scale grains, *Science*. 347 (2015) 522–525. doi:10.1126/science.aaa0472.
- [7] A. Chilvery, S. Das, P. Guggilla, C. Brantley, A. Sunda-Meya, A perspective on the recent progress in solution-processed methods for highly efficient perovskite solar cells, *Science and Technology of Advanced Materials*. 17 (2016) 650–658.
- [8] Y. Ling, Z. Yuan, Y. Tian, X. Wang, J.C. Wang, Y. Xin, K. Hanson, B. Ma, H. Gao, Bright light-emitting diodes based on organometal halide perovskite nanoplatelets, *Advanced Materials*. 28 (2016) 305–311.
- [9] H. Tsai, W. Nie, J.-C. Blancon, C.C. Stoumpos, C.M.M. Soe, J. Yoo, J. Crochet, S. Tretiak, J. Even, A. Sadhanala, others, Stable Light-Emitting Diodes Using Phase-Pure Ruddlesden–Popper Layered Perovskites, *Advanced Materials*. 30 (2018) 1704217.
- [10] S.A. Veldhuis, P.P. Boix, N. Yantara, M. Li, T.C. Sum, N. Mathews, S.G. Mhaisalkar, Perovskite materials for light-emitting diodes and lasers, *Advanced Materials*. 28 (2016) 6804–6834.
- [11] D. Shi, V. Adinolfi, R. Comin, M. Yuan, E. Alarousu, A. Buin, Y. Chen, S. Hoogland, A. Rothenberger, K. Katsiev, others, Low trap-state density and long carrier diffusion in organolead trihalide perovskite single crystals, *Science*. 347 (2015) 519–522.
- [12] C. Eames, J.M. Frost, P.R. Barnes, B.C. O’regan, A. Walsh, M.S. Islam, Ionic transport in hybrid lead iodide perovskite solar cells, *Nature Communications*. 6 (2015) 7497.
- [13] J. Ma, L.-W. Wang, The nature of electron mobility in hybrid perovskite CH₃NH₃PbI₃, *Nano Letters*. 17 (2017) 3646–3654.
- [14] Y.-C. Huang, C.-S. Tsao, Y.-J. Cho, K.-C. Chen, K.-M. Chiang, S.-Y. Hsiao, C.-W. Chen, C.-J. Su, U.-S. Jeng, H.-W. Lin, Insight into evolution, processing and performance of multi-length-scale structures in planar heterojunction perovskite solar cells, *Scientific Reports*. 5 (2015) 13657.
- [15] B. Wang, K.Y. Wong, S. Yang, T. Chen, Crystallinity and defect state engineering in organo-lead halide perovskite for high-efficiency solar cells, *Journal of Materials Chemistry A*. 4 (2016) 3806–3812.
- [16] J. Schlipf, P. Müller-Buschbaum, Structure of Organometal Halide Perovskite Films as Determined with Grazing-Incidence X-Ray Scattering Methods, *Advanced Energy Materials*. 7 (2017) 1700131.
- [17] M. Shirayama, H. Kadowaki, T. Miyadera, T. Sugita, M. Tamakoshi, M. Kato, T. Fujiseki, D. Murata, S. Hara, T.N. Murakami, others, Optical transitions in hybrid perovskite solar cells: ellipsometry, density functional theory, and quantum efficiency analyses for CH₃NH₃PbI₃, *Physical Review Applied*. 5 (2016) 014012.
- [18] I. Montes-Valenzuela, F. Pérez-Sánchez, A. Morales-Acevedo, Structural, optical and photoluminescence properties of hybrid metal–organic halide perovskite thin films prepared by a single step solution method, *Journal of Materials Science: Materials in Electronics*. (2018) 1–7.
- [19] S. Zhang, Welcome to the Nanoscience and Nanotechnology Letters, *Nanoscience and Nanotechnology Letters*. 1 (2009) 1–2.

- [20] H.J. Snaith, A. Abate, J.M. Ball, G.E. Eperon, T. Leijtens, N.K. Noel, S.D. Stranks, J.T.-W. Wang, K. Wojciechowski, W. Zhang, Anomalous hysteresis in perovskite solar cells, *The Journal of Physical Chemistry Letters*. 5 (2014) 1511–1515.
- [21] W. Tress, N. Marinova, T. Moehl, S.M. Zakeeruddin, M.K. Nazeeruddin, M. Grätzel, Understanding the rate-dependent J–V hysteresis, slow time component, and aging in CH₃NH₃PbI₃ perovskite solar cells: the role of a compensated electric field, *Energy & Environmental Science*. 8 (2015) 995–1004.
- [22] S. Matsuda, E. Kikuchi, Y. Yamane, Y. Okazaki, S. Yamazaki, Channel length dependence of field-effect mobility of c-axis-aligned crystalline In–Ga–Zn–O field-effect transistors, *Japanese Journal of Applied Physics*. 54 (2015) 041103.
- [23] G. Jo, J. Maeng, T.-W. Kim, W.-K. Hong, B.-S. Choi, T. Lee, Channel-length and gate-bias dependence of contact resistance and mobility for In₂O₃ nanowire field effect transistors, *Journal of Applied Physics*. 102 (2007) 084508.
- [24] P. Mittal, B. Kumar, Y.S. Negi, B.K. Kaushik, R. Singh, Channel length variation effect on performance parameters of organic field effect transistors, *Microelectronics Journal*. 43 (2012) 985–994.
- [25] Z. Chu, M. Yang, P. Schulz, D. Wu, X. Ma, E. Seifert, L. Sun, X. Li, K. Zhu, K. Lai, Impact of grain boundaries on efficiency and stability of organic-inorganic trihalide perovskites, *Nature Communications*. 8 (2017) 2230.
- [26] S. Haile, G. Staneff, K. Ryu, Non-stoichiometry, grain boundary transport and chemical stability of proton conducting perovskites, *Journal of Materials Science*. 36 (2001) 1149–1160.
- [27] Y. Shao, Y. Fang, T. Li, Q. Wang, Q. Dong, Y. Deng, Y. Yuan, H. Wei, M. Wang, A. Gruverman, others, Grain boundary dominated ion migration in polycrystalline organic–inorganic halide perovskite films, *Energy & Environmental Science*. 9 (2016) 1752–1759.
- [28] S.M. Vorpahl, S.D. Stranks, H. Nagaoka, G.E. Eperon, M.E. Ziffer, H.J. Snaith, D.S. Ginger, others, Impact of microstructure on local carrier lifetime in perovskite solar cells, *Science*. (2015) aaa5333.
- [29] G. Jo, J. Maeng, T.-W. Kim, W.-K. Hong, B.-S. Choi, T. Lee, Channel-length and gate-bias dependence of contact resistance and mobility for In₂O₃ nanowire field effect transistors, *Journal of Applied Physics*. 102 (2007) 084508.
- [30] M.S. Choi, G.-H. Lee, Y.-J. Yu, D.-Y. Lee, S.H. Lee, P. Kim, J. Hone, W.J. Yoo, Controlled charge trapping by molybdenum disulphide and graphene in ultrathin heterostructured memory devices, *Nature Communications*. 4 (2013) 1624.
- [31] Goedel, S. Guha, X. Moya, others, Understanding charge transport in lead iodide perovskite thin-film field-effect transistors, *Science Advances*. 3 (2017) e1601935.
- [32] X.Y. Chin, D. Cortecchia, J. Yin, A. Bruno, C. Soci, Lead iodide perovskite light-emitting field-effect transistor, *Nature Communications*. 6 (2015) 7383.
- [33] S.P. Senanayak, B. Yang, T.H. Thomas, N. Giesbrecht, W. Huang, E. Gann, B. Nair, K. Goedel, S. Guha, X. Moya, others, Understanding charge transport in lead iodide perovskite thin-film field-effect transistors, *Science Advances*. 3 (2017) e1601935.
- [34] S. Olthof, K. Meerholz, Substrate-dependent electronic structure and film formation of MAPbI₃ perovskites, *Scientific Reports*. 7 (2017) 40267.

CHAPTER 4. MIXED CATION PEROVSKITE BASED FIELD EFFECT TRANSISTORS

4.1. Introduction

Recent efforts in the field of perovskite have been focused in the composition optimization as a promising approach for metal halide perovskite to further tune the band gap and enhance the stability. Approach such as the replacement of MA (methylAmmonium) by FA (formamidinium) in the perovskite composition offers improved thermal stability and a reduced band gap close to the single junction optimum[1]. However, the crystallization process exhibits two structural final states at room temperature: it can crystallize either into a photoinactive, non-perovskite hexagonal δ -phase (“yellow phase”); or a photoactive perovskite α -phase (“black phase”)[2,3].

It has also been reported that the partial replacement of FA by Cs improved photo and moisture stabilities[4,5]. The first FA/MA/Cs triple cation $(\text{FAPbI}_3)_{0.83}(\text{MAPbBr}_3)_{0.17}$ has been reported by Saliba *et al.*[5] where the addition of Cs has suppressed non-perovskite hexagonal phase resulting in an enhanced crystallization, high quality, thermally and structurally stable perovskite films with a bandgap of 1.6 eV.

4.2. Motivation

In this study, we replaced MAPbI_3 in field effect transistors (chapter 3) with the recently discovered mixed cation (Cs/MA/FA) perovskite in order to enhance the device performances of PFETs and to analyze their stability. We first investigate the role of Cs on mixed cation MA/FA perovskites by measuring the crystallinity and the morphology of the films. These results are correlated to the PFETs performances obtained with each composition.

Indeed stability and reproducibility tests were performed on field effect transistors with mixed cation and MAPbI_3 as active layers respectively.

4.3. Characterization and analysis of structural and optical properties for large grain sized perovskite based thin films

First, we studied the crystallographic structure of triple cation (MA/FA/Cs) perovskite thin films by performing X-ray diffraction. The stoichiometric ratio used for mixed cation

perovskite was $\text{FA}_{0.75-x}\text{MA}_{0.25}\text{Cs}_x\text{PbI}_3$ where x is the molar fraction of Cs used to respect the total amount of cations $\text{FA/MA/Cs} = 1$ (in our case $x = 0.05, 0.15$ and 0.25). These films were spin-coated by using the previously developed hot casting method [6]. More details about the perovskite films deposition are given in chapter 2.

The stoichiometric ratio used for $\text{FA}_{0.70}\text{MA}_{0.25}\text{Cs}_{0.05}\text{PbI}_3$ ($\text{FA}_{0.75-x}\text{MA}_{0.25}\text{Cs}_{0.05}\text{PbI}_3$ perovskite with $x = 0.05$) was the previously optimized by Tsai *et al.* [13] where 70% FA was incorporated within the lattice to form the cubic structure, 25% of MA was added to stabilize the α phase of the FA/MA alloy whereas the addition of 5% Cs was required to stabilize the cubic phase which otherwise undergoes phase segregation at room temperature.

Figure 4.1 illustrates the X-ray diffraction (XRD) for $\text{FA}_{0.75-x}\text{MA}_{0.25}\text{Cs}_x\text{PbI}_3$ with $x = 0.05, 0.15$ and 0.25 .

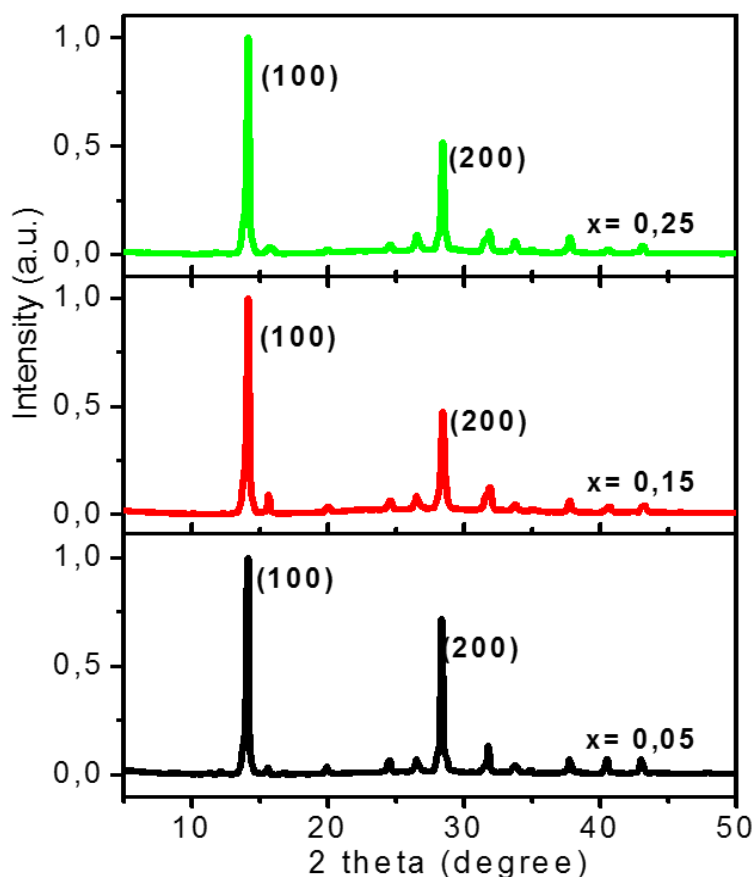


Figure 4.1. XRD patterns of cesium-containing triple cation $\text{FA}_{0.75-x}\text{MA}_{0.25}\text{Cs}_x\text{PbI}_3$ perovskite thin films with $x = 0.05, 0.15$ and 0.25 on glass substrates. (These graphs were plotted in linear scale).

These measurements exhibit a pure perovskite phase with sharp and strong diffraction peaks at 2θ equals to 14.1° and 28.3° corresponding to the (100) and (200) planes of the perovskite crystalline structure for all three perovskite films.

As previously reported [3–5,7], the absence or too high amount of Cs on FA/MA cations leads to an incomplete conversion of FA perovskite into the photoactive black phase. This is a very typical observation for mixed cation, commonly noted at 11.6° and 12.7° corresponding to the photoinactive hexagonal δ -phase of FAPbI_3 and the cubic PbI_2 , respectively[3–5,7].

Here, by analyzing the XRD of mixed cation perovskite $\text{FA}_{0.75-x}\text{MA}_{0.25}\text{Cs}_x\text{PbI}_3$ with different Cs content (Figure 4.1) we confirm that those peaks at 11.6° and 12.7° are negligible for all the cases. This observation demonstrates the correct formation of the black perovskite phase and the stabilization of the perovskite phase for $\text{FA}_{0.75-x}\text{MA}_{0.25}\text{Cs}_x\text{PbI}_3$ with $x = 0.05, 0.15$ and 0.25 . In order to obtain further information about the cesium content in triple cation perovskite we perform absorbance measurements.

Figure 4.2a shows the energy-dependence absorbance spectra of mixed cation perovskite thin films with different Cs concentration. The optical energy gap (E_g) for $\text{FA}_{0.75-x}\text{MA}_{0.25}\text{Cs}_x\text{PbI}_3$ thin films was extracted from the $(\alpha h\nu)^{1/2}$ versus the photon energy ($h\nu$) graph as illustrated in Figure 4.2b. The interception of the linear region (dotted lines) with the x-axis gives the value of the optical energy gap (E_g). The measurements exhibit a shift when Cs is added to the FA/MA cations from 1.50 to 1.56 with $x = 0.05$ and $x = 0.25$ respectively. These observations are in good agreement with previous reports in the literature[8,9].

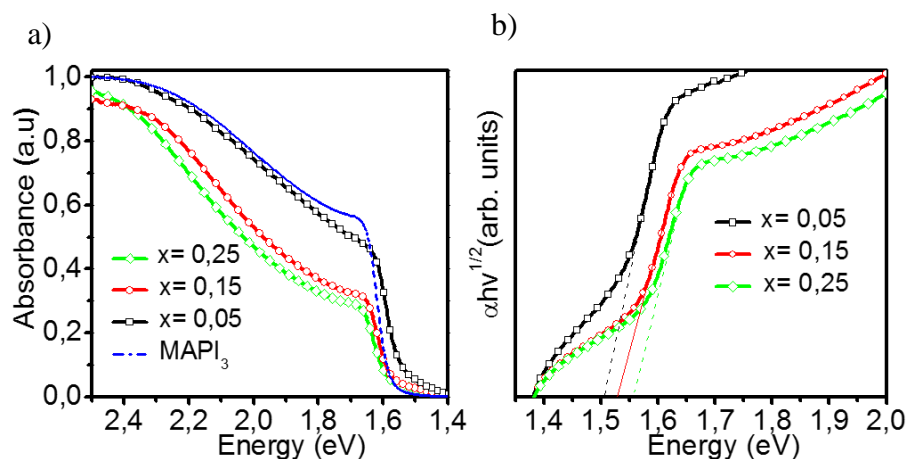


Figure 4.2. Optical analysis of $\text{FA}_{0.75-x}\text{MA}_{0.25}\text{Cs}_x\text{PbI}_3$ with $x = 0.05, 0.15$ and 0.25 thin films deposited on glass substrates. a) The energy – dependent absorbance spectra b) $(\alpha h\nu)^{1/2}$ versus the photon energy ($h\nu$).

Optical micrographs were used to compare the morphologies of mixed cation $\text{FA}_{0.75-x}\text{MA}_{0.25}\text{Cs}_x\text{PbI}_3$ perovskite films prepared from different Cs concentrations deposited on glass substrates (Figure 4.3).

$\text{FA}_{0.75-x}\text{MA}_{0.25}\text{Cs}_x\text{PbI}_3$ films deposited on glass substrates

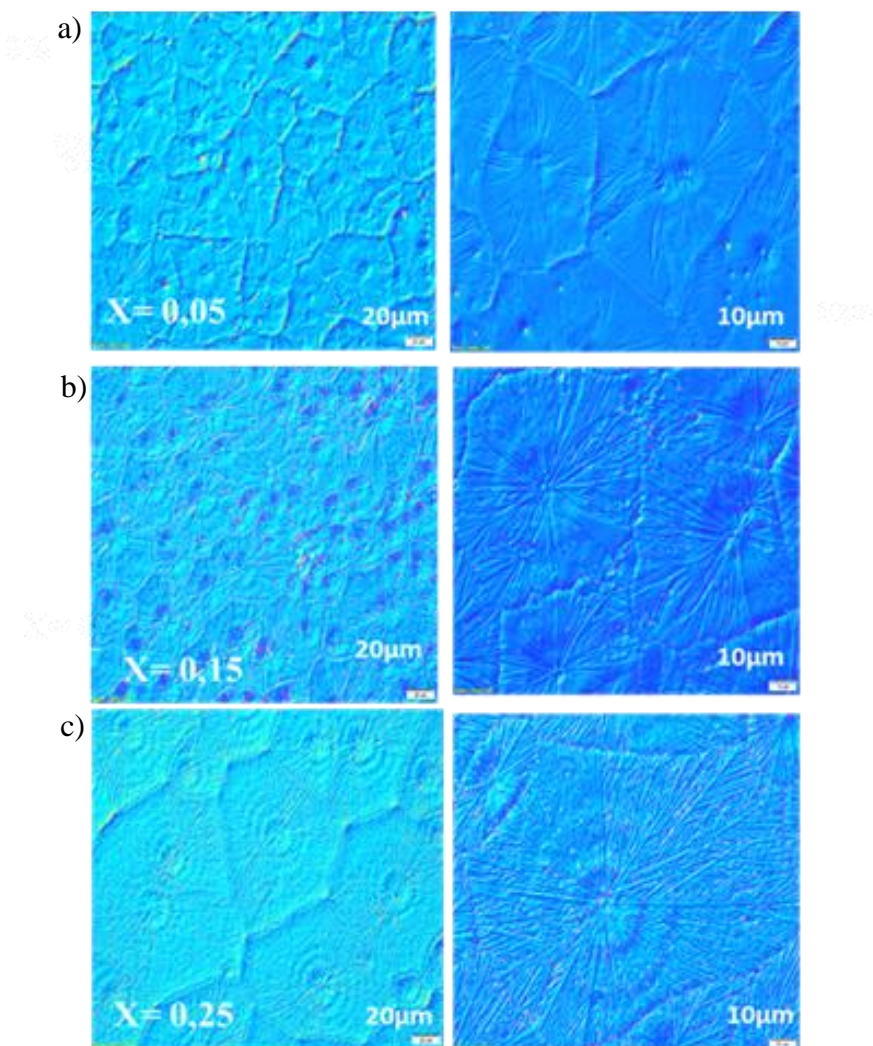


Figure 4.3. Optical micrographs of mixed cation $\text{FA}_{0.75-x}\text{MA}_{0.25}\text{Cs}_x\text{PbI}_3$ perovskite thin films with a) $x = 0.05$, b) 0.15 and c) 0.25 deposited on glass substrates.

By comparing the optical images, we observed that the Cs concentration plays a key role on the perovskite grain sizes and consequently on the film quality. Higher concentration of Cs ($x=0.25$) leads to larger grain size $\sim 130 \mu\text{m}$ in comparison to $80 \mu\text{m}$ obtained with $x = 0.05$ and 0.15.

In this section, we confirmed that the photoinactive hexagonal phase on mixed cation (FA/MA) perovskite previously observed in the literature [10–13] was successfully eliminated by adding Cs cation on the perovskite composition. Moreover, by using a stoichiometric ratio of $\text{FA}_{0.75-x}$

$x\text{MA}_{0.25}\text{Cs}_x\text{PbI}_3$, we succeeded in obtaining pinholes free thin films with a band gap between 1.50 - 1.56 eV by using mixed cation perovskites. We demonstrated that the grain size and consequently the film quality of mixed cation FA/MA/Cs lead iodide perovskites is strongly linked to Cs cation concentration in the system. This fact is expected to exhibit lower carrier recombination rate resulting in enhanced device performances [5, 6, 10, 11].

4.4. Mixed cation perovskite based FETs

In this study, we use mixed cation films as active layer on field effect transistors. We first study the morphology of mixed cation $\text{FA}_{0.75-x}\text{MA}_{0.25}\text{Cs}_x\text{PbI}_3$ perovskite films deposited on hafnium dioxide (HfO_2) which is the main material used as gate insulator in this thesis (Figure 4.4).

$\text{FA}_{0.75-x}\text{MA}_{0.25}\text{Cs}_x\text{PbI}_3$ deposited on HfO_2 substrates

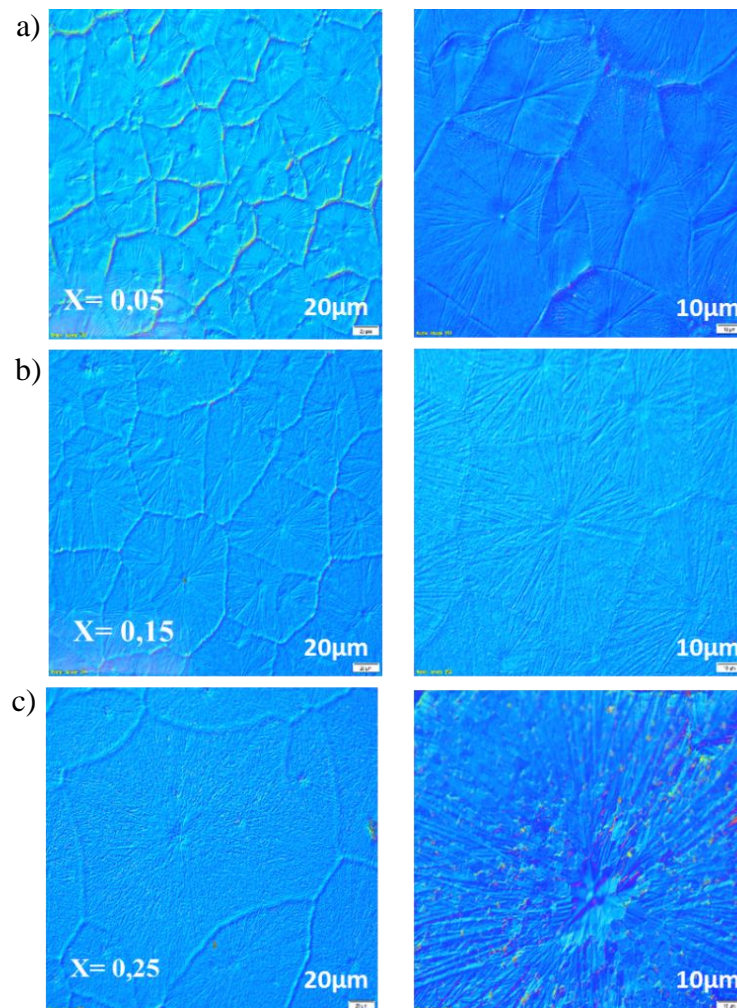


Figure 4.4. Optical micrographs of mixed cation $\text{FA}_{0.75-x}\text{MA}_{0.25}\text{Cs}_x\text{PbI}_3$ perovskite thin films with a) $x = 0.05$, b) 0.15 and c) 0.25 deposited on HfO_2 .

By comparing the optical micrographs in Figure 4.4, we observed the same trend as previously on perovskite thin films deposited on glass substrates. Higher Cs concentration, $x=0.25$, on $\text{FA}_{0.75-x}\text{MA}_{0.25}\text{Cs}_x\text{PbI}_3$ leads to larger grain size resulting in more uniform perovskite thin films either on glass or hafnium dioxide substrates.

Moreover, we found that the grain size of $\text{FA}_{0.75-x}\text{MA}_{0.25}\text{Cs}_x\text{PbI}_3$ exhibits a notable improvement by using hafnium dioxide as substrates in comparison to glass substrates. $\text{FA}_{0.75-x}\text{MA}_{0.25}\text{Cs}_x\text{PbI}_3$ with $x = 0.25$ exhibit an increase on the grain size by up to two times by using hafnium dioxide as substrates leading to values close to 0.3 μm . (Figure 4.5).

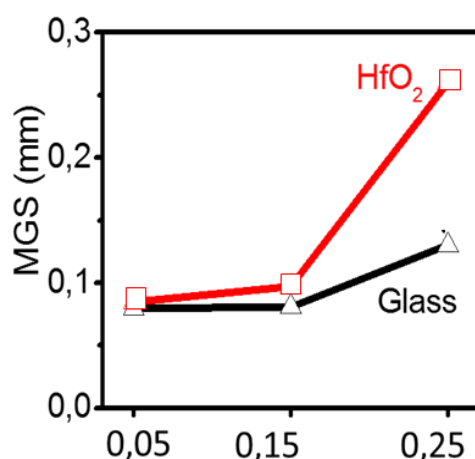


Figure 4.5. Maximum grain size (MGS) of mixed cation $\text{FA}_{0.75-x}\text{MA}_{0.25}\text{Cs}_x\text{PbI}_3$ perovskite thin films with different Cs concentrations deposited on glass and HfO_2 substrates.

Then, we fabricated a field effect transistor in bottom contact geometry with a channel length (L) $\sim 70 \mu\text{m}$ and width (W) $\sim 100 \mu\text{m}$ using mixed cation $\text{FA}_{0.75-x}\text{MA}_{0.25}\text{Cs}_x\text{PbI}_3$ with $x=0.05$, 0.15 and 0.25 and hafnium dioxide (HfO_2) films as gate insulator. The detailed process is described in chapter 2.

The FETs characteristics and device performances measured at room temperature in the dark are illustrated in Figure 4.6 and Table 4.1 respectively. The scan rate used for these measurements is 1V/s. It should be noted that these measurements were extracted after consecutive cycles of biasing.

As previously predicted in the above section, we clearly observed that the concentration of Cs on perovskite $\text{FA}_{0.75-x}\text{MA}_{0.25}\text{Cs}_x\text{PbI}_3$ based FETs plays a key role on the device performances (Figure 4.6). All the devices show an I_D (V_G) curve with a hysteresis depending on Cs concentration.

The performances obtained with low Cs concentration ($x = 0.05$), are extremely poor with a very weak gate modulation and a notable hysteresis in their transfer characteristics. This fact hinders the extraction of the device parameters (Figure 4.6a).

By contrast, a marked enhancement on the devices performances was observed with higher Cs concentrations. $\text{FA}_{0.60}\text{MA}_{0.25}\text{Cs}_{0.15}\text{PbI}_3$ and $\text{FA}_{0.50}\text{MA}_{0.25}\text{Cs}_{0.25}\text{PbI}_3$ lead to stronger gate modulation where both compositions exhibit electron and hole transport with comparable I_{ds} value for both n- and p-type carrier (Figure 4.6 b-c).

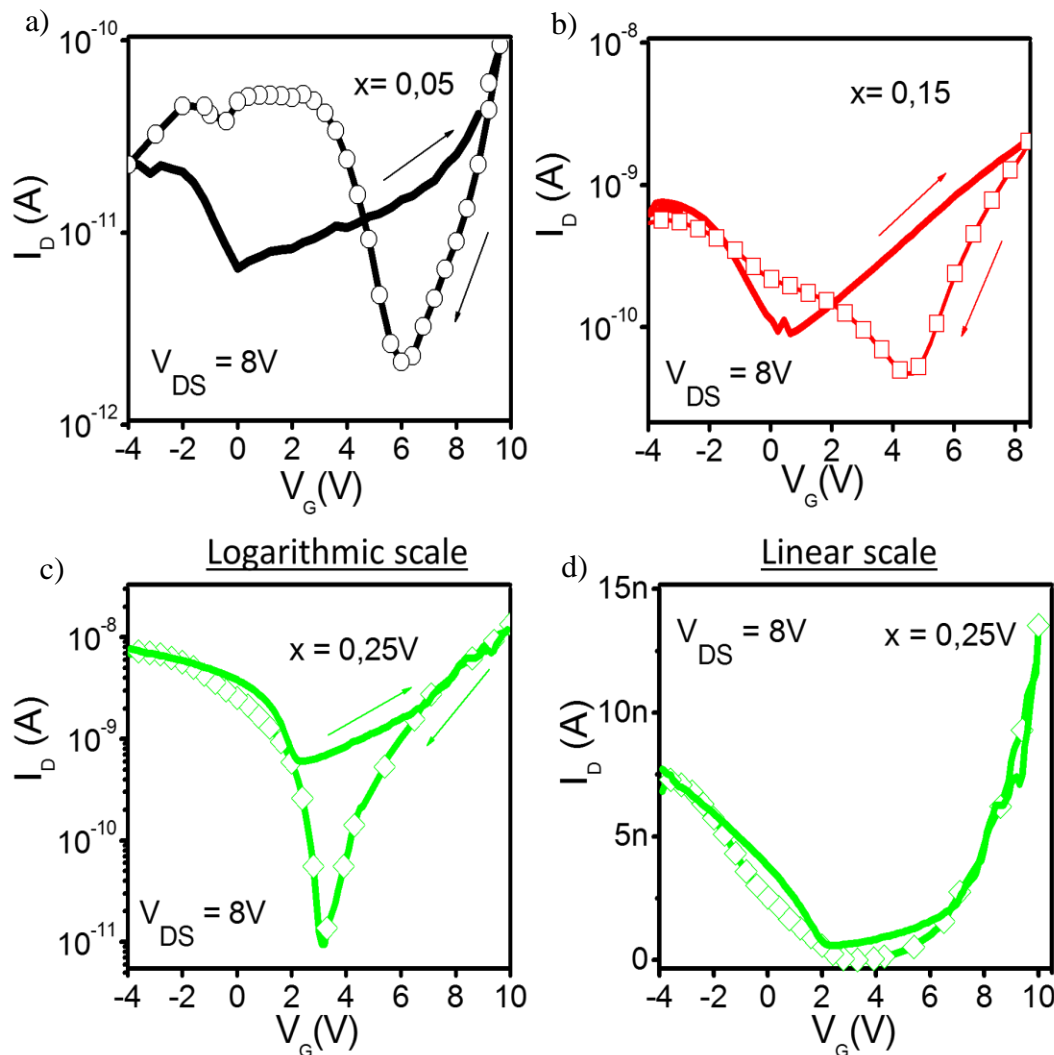


Figure 4.6. Transfer characteristics of mixed cation $\text{FA}_{0.75-x}\text{MA}_{0.25}\text{Cs}_x\text{PbI}_3$ perovskite field effect transistors with different concentration of Cs. a) $x = 0.05$, b) 0.15 and c) 0.25 and d) $x = 0.25$ plot in linear scale.

By using $\text{FA}_{0.5}\text{MA}_{0.25}\text{Cs}_{0.25}\text{PbI}_3$ (Figure 4.6c) the drain current is increased by up to one order of magnitude for both types of carriers in comparison to $\text{FA}_{0.65}\text{MA}_{0.25}\text{Cs}_{0.15}\text{PbI}_3$ (Figure 4.6b).

Consequently, the carrier mobility increases up to one order of magnitude higher resulting in values up to $\sim 1 \times 10^{-3} \text{ cm}^2/\text{Vs}$. These devices also exhibit a better Ion/Ioff ratio with values up to 800 which are up to one order of magnitude higher than the obtained with $\text{FA}_{0.60}\text{MA}_{0.25}\text{Cs}_{0.15}\text{PbI}_3$. In addition to the enhanced performance by using $\text{FA}_{0.5}\text{MA}_{0.25}\text{Cs}_{0.25}\text{PbI}_3$, we found that the I_D - V_G curves illustrated in Figure 4.6c-d exhibit a smaller hysteresis.

$\text{FA}_{0.75-x}\text{MA}_{0.25}\text{Cs}_x\text{PbI}_3$	X = 0.05	X = 0.15	X = 0.25
Vth (V) Forward	Non relevant	0.54	3
Vth (V) Reverse	Hole – 5.5 Electron – 6.5	4.88	2.6
Ion/Ioff Forward	Non relevant	22	14
Ion/Ioff Reverse	25	48	800
Gm (nA/V) Forward	Non relevant	Hole – 0.24 Electron – 0.36	Hole – 1.5 Electron – 2.5
Gm (nA/V) Reverse	Hole – 0.007 Electron – 0.001	Hole – 0.05 Electron – 0.67	Hole – 1.6 Electron – 2.6
μ(cm^2/Vs) Forward	Non relevant	Hole – 5.7×10^{-5} Electron – 3.7×10^{-5}	Hole – 8×10^{-4} Electron – 1×10^{-3}
μ (cm^2/Vs) Reverse	Non relevant	Hole – 5.9×10^{-5} Electron – 1.5×10^{-4}	Hole – 8.5×10^{-4} Electron – 1.5×10^{-3}

Table 4.1 Device parameters (measured in forward and reverse scan) of mixed cation $\text{FA}_{0.75-x}\text{MA}_{0.25}\text{Cs}_x\text{PbI}_3$ perovskite field effect transistors with different concentration of Cs ($x= 0.05, 0.15$ and 0.25).

The Cs contribution on mixed cation (MA/FA/Cs) system leads to a higher grain size perovskite thin films. This fact is expected to reduce significantly the defect - assisted trapping of charge carriers leading to an enhancement on the device performances [10–13].

As shown on Figure 4.6c-d), ambipolar PFET is obtained with $x = 0.25$ highlighting a relatively small hysteresis. To evaluate such hysteresis, transfer characteristics was plotted in linear scale.

In this section, we showed that the incorporation of Cs on mixed cation (MA/FA/Cs) perovskite has a strong impact on the film quality and consequently on the device performances of PFETs. We succeed in obtaining operational mixed cation perovskite based FETs with a gate modulation for p and n-type carriers by growing $\text{FA}_{0.5}\text{MA}_{0.25}\text{Cs}_{0.25}\text{PbI}_3$ perovskite thin films. As mixed cation perovskite is considered as a promising route for the development of more stable and reproducible perovskite based devices [3–5] in comparison to MAPbI_3 , in the next section we analyze the performances and stability of PFETs with MAPbI_3 and $\text{FA}_{0.5}\text{MA}_{0.25}\text{Cs}_{0.25}\text{PbI}_3$ as active layers respectively.

4.5. Mixed cation perovskite based FETs

4.5.1. Devices performances $\text{FA}_{0.5}\text{MA}_{0.25}\text{Cs}_{0.25}\text{PbI}_3$

In this study, we measure the devices performances of perovskite based mixed cation FA/MA with a 25% Cs addition.

The FETs characteristics and device performances are illustrated in Figure 4.7 and Table 4.2.

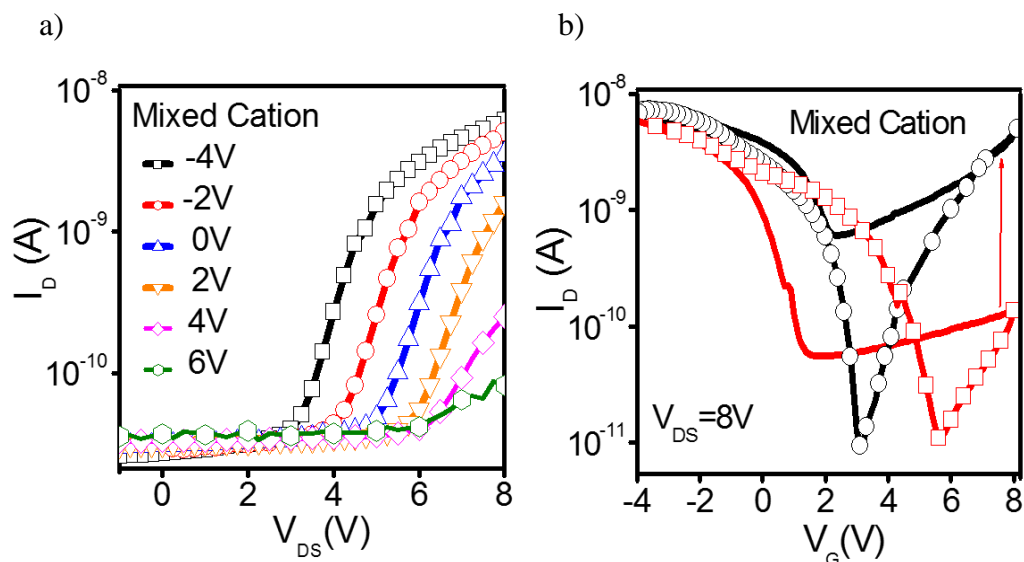


Figure 4.7. a) Output characteristics b) transfer characteristics for mixed cation $\text{FA}_{0.5}\text{MA}_{0.25}\text{Cs}_{0.25}\text{PbI}_3$ as active layers.

Before biasing the device (red line-square in the I_D - V_G curve), the transfer characteristics for $FA_{0.5}MA_{0.25}Cs_{0.25}PbI_3$ as active layer in FETs clearly shows a field effect modulation with a gate modulation for p type carriers exhibiting hole mobility values by up to $8.5 \times 10^{-4} \text{ cm}^2/\text{Vs}$.

Whereas, the measurements obtained after consecutive cycles clearly indicate ambipolar transport with a gate dependence for both n and p type carriers. For the same source and drain voltage ($V_{DS} = 8 \text{ V}$), this device exhibits a balanced electron and hole transport with comparable electron and hole transconductance and mobility values (Table 4.2). This phenomenon is explained with more details in chapter 3.

For the output characteristics we don't get a saturation and we can detect the value of the threshold voltage greater than $V_G = 2 \text{ V}$. We also measure a shift for the starting point between 3 V to 6 V like in $MAPbI_3$ devices. In addition for both cases, before and after biasing, the I_D - V_G curves illustrated in Figure 4.7 exhibit small changes in the transconductance and mobility values for the forward and reverse scan indicating, a reduced hysteresis.

	$FA_{0.5}MA_{0.25}Cs_{0.25}PbI_3$	
	First measurement	After Biasing
V_{th} (V) Forward	0.53	3.4
V_{th} (V) Reverse	4.6	2.6
I_{on}/I_{off}	490	800
G_m (nA/V) Forward	Hole – 1.3 Electron – NR	Hole – 1.5 Electron – 2.5
G_m (nA/V) Reverse	Hole – 1 Electron – NR	Hole – 1.6 Electron – 2.6
μ (cm²/Vs) Forward	Hole – 8.5×10^{-4} Electron – NR	Hole – 8×10^{-4} Electron – 1×10^{-3}
μ (cm²/Vs) Reverse	Hole – 1.5×10^{-4} Electron – NR	Hole – 8.5×10^{-4} Electron – 1.5×10^{-3}

Table 4.2. Device parameters of mixed cation $FA_{0.5}MA_{0.25}Cs_{0.25}PbI_3$ perovskite field effect transistor before and after biasing.

By using $\text{FA}_{0.5}\text{MA}_{0.25}\text{Cs}_{0.25}\text{PbI}_3$ as active layer in FETs, we succeed in obtaining operational FETs at room temperature with a gate modulation for both types of carriers.

In the next section, we evaluate the stability and reproducibility of perovskite based field effect transistors with $\text{FA}_{0.5}\text{MA}_{0.25}\text{Cs}_{0.25}\text{PbI}_3$ and MAPbI_3 as active layers.

4.5.2. Stability and reproducibility of mixed cation and lead iodide perovskite based FETs

Here, we evaluated the stability of perovskite based FETs with MAPbI_3 and $\text{FA}_{0.5}\text{MA}_{0.25}\text{Cs}_{0.25}\text{PbI}_3$ as active layers in the same geometry.

We first study the stability of these devices by operating them under consecutive I_D - V_G cycles continuously over 14 hours as illustrated in Figure 4.8. It should be noted that the stability test was started once we got ambipolar behavior in the transfer characteristics. The time dependent $I_{\text{on}}/I_{\text{off}}$ ratio of these curves is illustrated in Figure 4.8c.

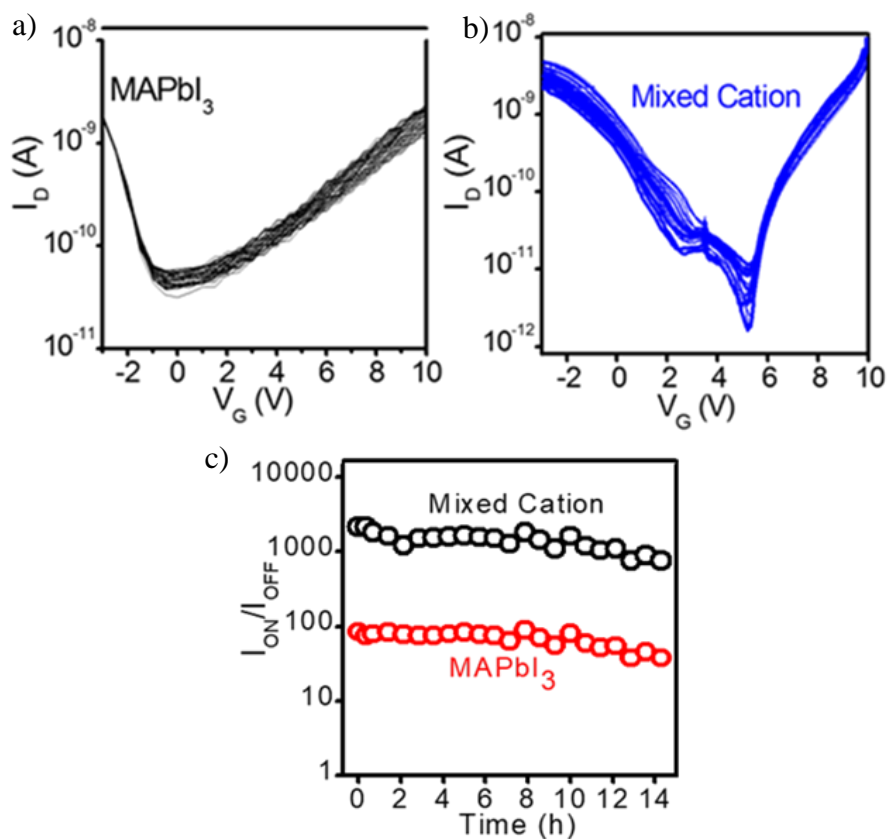


Figure 4.8) Continuous I_D - V_G cycles of PFETs using different active layers a) MAPbI_3 and b) mixed cation $\text{FA}_{0.75-x}\text{MA}_{0.25}\text{Cs}_{0.25}\text{PbI}_3$. c) Time dependent- $I_{\text{on}}/I_{\text{off}}$ ratio for both transistors.

From these transfer characteristics illustrated in Figure 4.8 a-b, we note that the devices performances for both cases, MAPbI₃ and FA_{0.5}MA_{0.25}Cs_{0.25}PbI₃ are slightly affected with the time after consecutive cycles of measurements. We observed that the I_D-V_G curves (V_G = -3 V to 10 V) exhibit small changes for the current after continuous biasing.

The Ion/Ioff ratio as function of time is illustrated in Figure 4.8c. The values remain quite stable by using either MAPbI₃ or FA_{0.5}MA_{0.25}Cs_{0.25}PbI₃, perovskite as active layers in PFETs. Thus, we confirm that these PFETs exhibit a quite good short term stability. This relative stability takes benefit from the hot-casting technique[2] offering the possibility to grow high quality perovskite thin films.

On the other hand, it is reported that adding Cs cation to the mixed cation FA/MA perovskites leads to a thermal stable composition with less phase impurities than MAPbI₃ being less sensitive to the processing conditions [10-13].

Here, we analyze this fact by plotting the maximum drain current at a fixed bias (V_G = -3V, V_{DS} = 8 V), the threshold voltage and mobility for both type of carriers for 20 different devices obtained with MAPbI₃ and FA_{0.5}MA_{0.25}Cs_{0.25}PbI₃ respectively (Figure 4.9).

In Figure 4.9, we clearly observed that mixed cation perovskite FA_{0.5}MA_{0.25}Cs_{0.25}PbI₃ based FETs exhibit more uniform values for the maximum drain current value (Figure 9a). The mobility values for both carriers (Figure 4.9 b and c) exhibit poor reproducibility with high dispersion in their values among 20 separated devices. For MAPbI₃ as active layer in FETs, a broad device parameters distribution is observed for all the conditions.

In this section, we demonstrated that the device performances obtained with hot-casted MAPbI₃ and FA_{0.5}MA_{0.25}Cs_{0.25}PbI₃ as active layers on FETs exhibit small changes after 14 hours of continuous measurements. Moreover, reproducibility test show large dispersion values for mobility and threshold voltage values for both types of transistors. These measurements clearly highlight the challenging fabrication of PFETs...

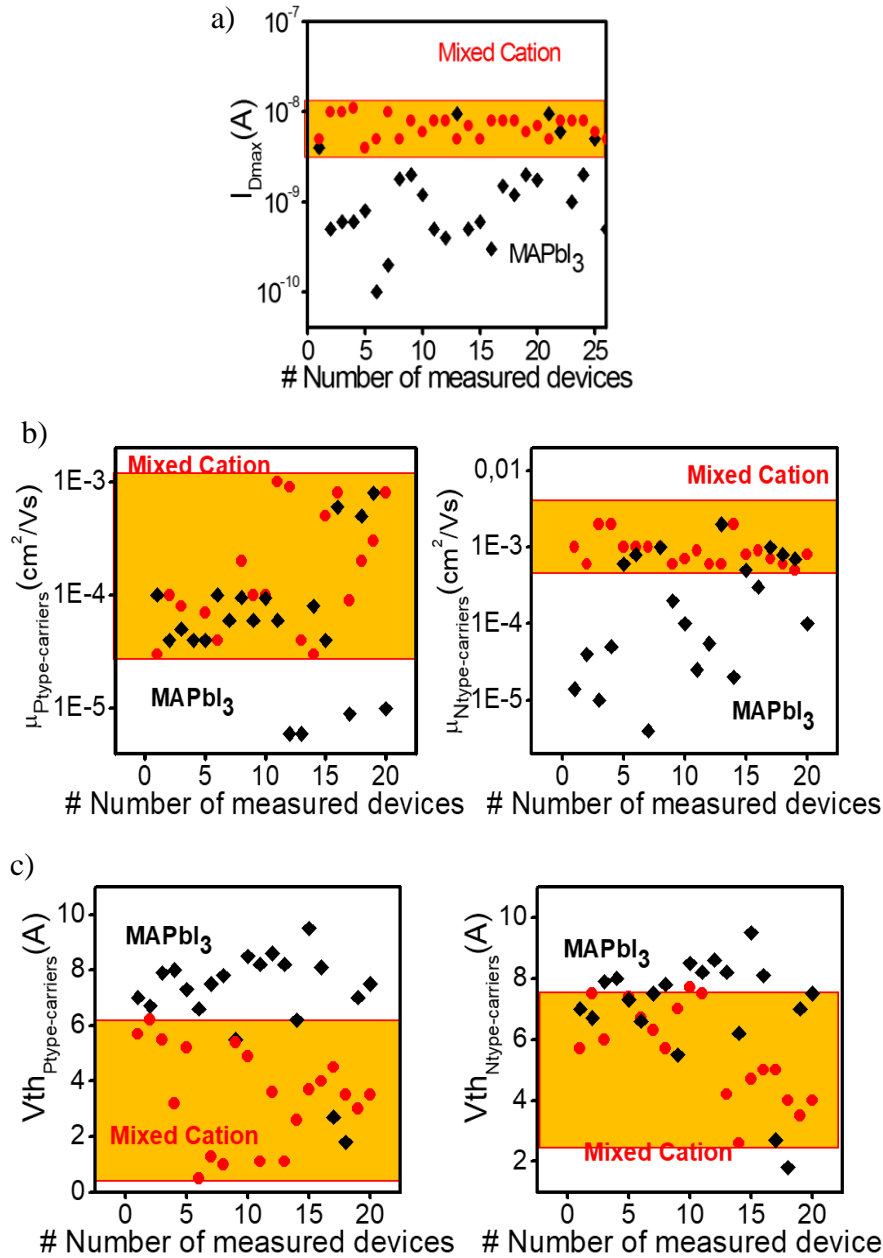


Figure 4.9. Dispersion of transistors parameters for MAPbI_3 and mixed cation $\text{FA}_{0.5}\text{MA}_{0.25}\text{Cs}_{0.25}\text{PbI}_3$ films used as active layers a) I_{Dmax} b) hole and electrons carriers mobility c) P type and N type threshold voltages.

4.6. Conclusion

Here in this chapter, we studied the role of Cs on mixed cation (FA/MA/Cs) perovskites field effect transistors with the stoichiometric ratio of $\text{FA}_{0.75-x}\text{MA}_{0.25}\text{Cs}_x\text{PbI}_3$ ($x = 0.05, 0.15$ and 0.25).

First, we studied the film morphology. We found that higher Cs concentration such as $x = 0.25$ ($\text{FA}_{0.5}\text{MA}_{0.25}\text{Cs}_{0.25}\text{PbI}_3$) leads to a larger grain size and more uniform thin films. Consequently, by employing such layer as active layer in FETs, we obtained ambipolar hybrid perovskite FET operational at room temperature with a small hysteresis in their transfer characteristics. Whereas, lower Cs concentration on mixed cation perovskite ($\text{FA}_{0.75-x}\text{MA}_{0.25}\text{Cs}_x\text{PbI}_3$ and $\text{FA}_{0.75-x}\text{MA}_{0.25}\text{Cs}_x\text{PbI}_3$) have probed to exhibit weaker device performances with a notable hysteresis. We also performed stability analysis with $\text{FA}_{0.70}\text{MA}_{0.25}\text{Cs}_{0.05}\text{PbI}_3$ and MAPbI_3 as semiconductor layer in FETs. The device performances obtained for both materials does not suffer a marked degradation after consecutive cycles of measurements highlighting relatively good short term stability.

Reproducibility tests highlight both types of transistors exhibit low degree of reproducibility. However, it should be noted that further optimization would be needed to obtain a better control during perovskite deposition in order to reduce the degree of dispersion obtained with both materials.

These results are the first results on the stability of hybrid perovskite based FETs at room temperature offering promising routes for understanding the charge transport properties of hybrid perovskites.

The next chapter aims at fabricating perovskite solar cells under air conditions and nitrogen atmosphere with organometallic lead halide perovskite.

4.7. References

- [1] W. Shockley, H.J. Queisser, Detailed balance limit of efficiency of p-n junction solar cells, *Journal of Applied Physics*. 32 (1961) 510–519.
- [2] N.J. Jeon, J.H. Noh, W.S. Yang, Y.C. Kim, S. Ryu, J. Seo, S.I. Seok, Compositional engineering of perovskite materials for high-performance solar cells, *Nature*. 517 (2015) 476.
- [3] N. Pellet, P. Gao, G. Gregori, T.-Y. Yang, M.K. Nazeeruddin, J. Maier, M. Grätzel, Mixed-organic-cation Perovskite photovoltaics for enhanced solar-light harvesting, *Angewandte Chemie*. 126 (2014) 3215–3221.
- [4] D.P. McMeekin, G. Sadoughi, W. Rehman, G.E. Eperon, M. Saliba, M.T. Hörantner, A. Haghighirad, N. Sakai, L. Korte, B. Rech, others, A mixed-cation lead mixed-halide perovskite absorber for tandem solar cells, *Science*. 351 (2016) 151–155.
- [5] M. Saliba, T. Matsui, J.-Y. Seo, K. Domanski, J.-P. Correa-Baena, M.K. Nazeeruddin, S.M. Zakeeruddin, W. Tress, A. Abate, A. Hagfeldt, others, Cesium-containing triple cation perovskite solar cells: improved stability, reproducibility and high efficiency, *Energy & Environmental Science*. 9 (2016) 1989–1997.
- [6] W. Nie, H. Tsai, R. Asadpour, J.-C. Blancon, A.J. Neukirch, G. Gupta, J.J. Crochet, M. Chhowalla, S. Tretiak, M.A. Alam, H.-L. Wang, A.D. Mohite, High-efficiency solution-processed perovskite solar cells with millimeter-scale grains, *Science*. 347 (2015) 522–525. doi:10.1126/science.aaa0472.
- [7] H. Tsai, R. Asadpour, J.-C. Blancon, C.C. Stoumpos, O. Durand, J.W. Strzalka, B. Chen, R. Verduzco, P.M. Ajayan, S. Tretiak, others, Light-induced lattice expansion leads to high-efficiency perovskite solar cells, *Science*. 360 (2018) 67–70.
- [8] M. Shirayama, H. Kadowaki, T. Miyadera, T. Sugita, M. Tamakoshi, M. Kato, T. Fujiseki, D. Murata, S. Hara, T.N. Murakami, others, Optical transitions in hybrid perovskite solar cells: ellipsometry, density functional theory, and quantum efficiency analyses for CH₃NH₃PbI₃, *Physical Review Applied*. 5 (2016) 014012.
- [9] I. Montes-Valenzuela, F. Pérez-Sánchez, A. Morales-Acevedo, Structural, optical and photoluminescence properties of hybrid metal–organic halide perovskite thin films prepared by a single step solution method, *Journal of Materials Science: Materials in Electronics*. (2018) 1–7.
- [10] G.E. Eperon, V.M. Burlakov, P. Docampo, A. Goriely, H.J. Snaith, Morphological control for high performance, solution-processed planar heterojunction perovskite solar cells, *Advanced Functional Materials*. 24 (2014) 151–157.
- [11] A. Dualeh, N. Tétreault, T. Moehl, P. Gao, M.K. Nazeeruddin, M. Grätzel, Effect of annealing temperature on film morphology of organic–inorganic hybrid perovskite solid-state solar cells, *Advanced Functional Materials*. 24 (2014) 3250–3258.

CHAPTER 5. PEROVSKITE BASED SOLAR CELLS FABRICATED IN DIFFERENT ATMOSPHERES

5.1 Introduction

Recent efforts have focused on the development of low-cost and consistent methods for the fabrication of solar cells in air condition being a step forward in processing techniques for the commercialization of perovskite solar cells[1-6].

Tai *et al.*[6] reported efficient and stable perovskite solar cells fabricated under humid conditions (RH ~ 70%) produced on mesoporous TiO₂ and using Pb-(SCN₂) precursor with power conversion efficiencies values (PCE) up to 15%. Troughton *et al.* [1] have developed an anti-solvent method during perovskite spin-coating able to capture the moisture and protect the perovskite layer. They obtained efficient solar cells with PCE up to 10% (area 13.5 cm²) fabricated in 75% RH ambient conditions.

5.2 Introduction

In this chapter, we report both methods for preparing operational perovskite solar cells under air (relative humidity higher than 60%) and in nitrogen glove box conditions. First, we present the air process for perovskite deposition and solar cells fabrication and then, we compare these results to the nitrogen atmosphere condition.

5.3 Perovskite solar cells processed under air

5.3.1 Characterization of perovskite thin film quality

First, we characterized the properties of perovskite thin films deposited using the thermal treatment under air conditions with high relative humidity (RH > 60%). The perovskite

precursor ($\text{CH}_3\text{NH}_3\text{PbI}_{(3-x)}\text{Cl}_x$) used was a commercial solution purchased from Ossila (more details are given in chapter 2).

Figure 5.1 shows the wavelength-dependence absorbance spectra of $\text{CH}_3\text{NH}_3\text{PbI}_{(3-x)}\text{Cl}_x$ perovskite thin films. The band-edge emission and absorption for $\text{CH}_3\text{NH}_3\text{PbI}_{(3-x)}\text{Cl}_x$ perovskite were observed at 1.61 eV (absorption onset at 773 nm) being in good agreements with previous reports [7-8].

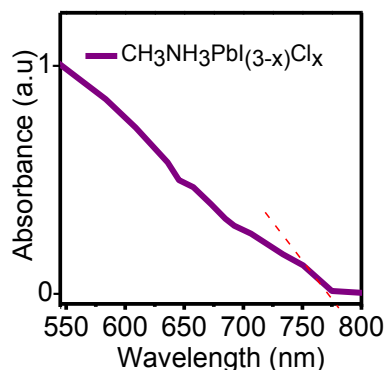


Figure 5.1. The wavelength – dependent absorbance spectra of $\text{CH}_3\text{NH}_3\text{PbI}_{(3-x)}\text{Cl}_x$ perovskite thin films.

The X-ray diffraction (XRD) patterns of $\text{CH}_3\text{NH}_3\text{PbI}_{(3-x)}\text{Cl}_x$ are illustrated in Figure 5.2. The data display sharp and strong diffraction peaks at 2 theta equals to 14.1° and 28.3° which correspond to the (110) and (220) planes of the perovskite crystalline structure indicating a orientated crystal structure as previously reported in the literature[9-11]. The perovskite thin film deposited under humid conditions can be mildly decomposed that's why there is another peak at 2theta equal to 12.6° which corresponding to (001) plane of PbI_2 .

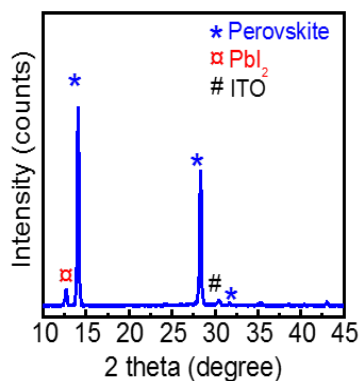


Figure 5.2. XRD patterns of $\text{CH}_3\text{NH}_3\text{PbI}_{(3-x)}\text{Cl}_x$ perovskite thin films on glass/ITO/ PEDOT:PSS substrates deposited under air conditions with $\text{RH} > 60\%$.

The morphological analysis of perovskite thin films using the thermal treatment in comparison with the as casting method are illustrated in Figure 5.3.

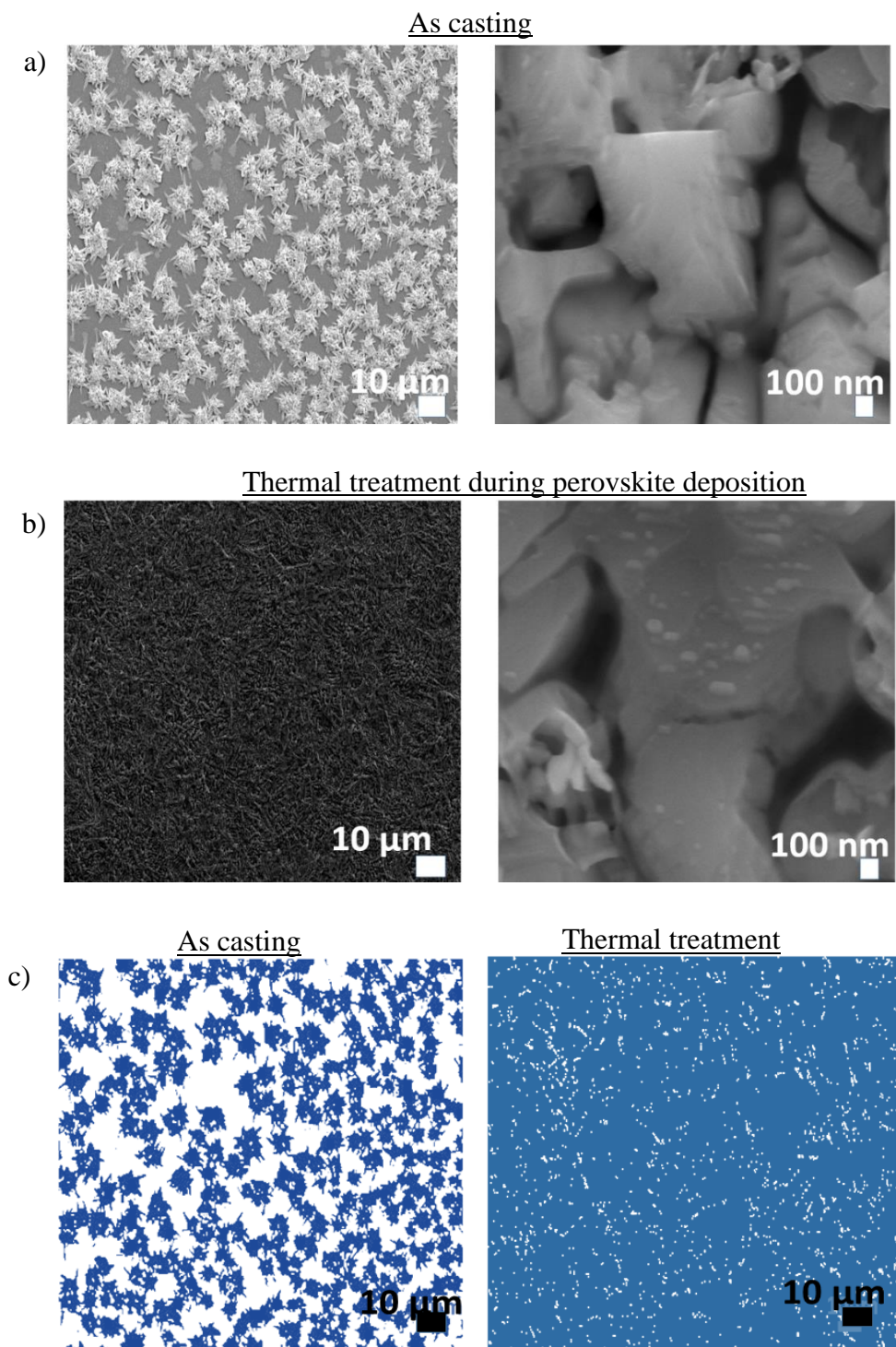


Figure 5.3. SEM images (low and high magnification) of $\text{CH}_3\text{NH}_3\text{PbI}_{(3-x)}\text{Cl}_x$ thin films deposited under high relative humidity ($\text{RH} > 60\%$) using different methods: a) as-casting b) thermal treatment during perovskite deposition. c) treatment with ImageJ of perovskite thin films of SEM images

From the SEM images illustrated in Figure 5.3a, we can observe that the films obtained with the as casting method are not uniform exhibiting a larger presence of non-covered zones. However, the thermal treatment during perovskite deposition provides uniform perovskite thin films which practically cover the entire substrate as illustrated in Figure 5.3b. Both processing conditions show different sizes and shapes of poly-crystalline films. The morphology is related with a network of disoriented high aspect ratio structures suggesting a significant film roughness (some of these results will be discussed later).

The fractional surface coverage values for both conditions were estimated by setting a color threshold on the SEM image and calculating the area above and below such threshold through Image J software. Figure 5.3c illustrates the SEM images after the treatment with ImageJ in where the blue and white colors represent the regions with and without perovskite respectively. For the perovskite thin films deposited under air conditions with the as casting method, the fractional surface coverage values drops to 46% in comparison to 95% for the film obtained with the thermal treatment.

On the other hand, it has been observed that the humidity during perovskite deposition has also an effect in the time needed to turn from yellow phase to the final perovskite phase (dark brown color) during the annealing. For perovskite thin films deposited with the as casting method under humid conditions $RH > 60\%$, the brown color appears 10 seconds after the spin coating step. However using the thermal treatment, this conversion occurs after several minutes. These observations are in good agreement with previous reports in the literature[12].

From the morphological analysis of perovskite thin films deposited under high relative humidity, we can conclude that the moisture has a detrimental impact on the perovskites crystal growth. The thin films are non-uniform with a very low coverage. The main effect of the lamp is to locally reduce the moisture amount. A measurement under the lamp leads to 20% RH compared to the room value $> 60\%$ RH. We demonstrated that using such thermal treatment, uniform perovskite thin films deposition can be achieved under humid conditions.

5.3.2 Perovskite solar cells fabricated under air conditions

Perovskite solar cells were fabricated under air conditions ($RH > 60\%$) using the thermal treatment during perovskite deposition as previously explained. Solar cells are also fabricated with low coverage (as casting method) film for comparison. The device architecture used in this study is illustrated in Figure 5.4 (details about the fabrication are given in the chapter 2).



Figure 5.4. Device architecture of the inverted perovskite solar cells used in this study.

Figure 5.5 shows the current density-voltage (J-V) curves of the best perovskite solar cells fabricated under air conditions ($RH > 60\%$) using the thermal treatment in comparison to the as casting method to deposit hybrid perovskite thin films. The best photovoltaic parameters of those devices are summarized in Table 5.1.

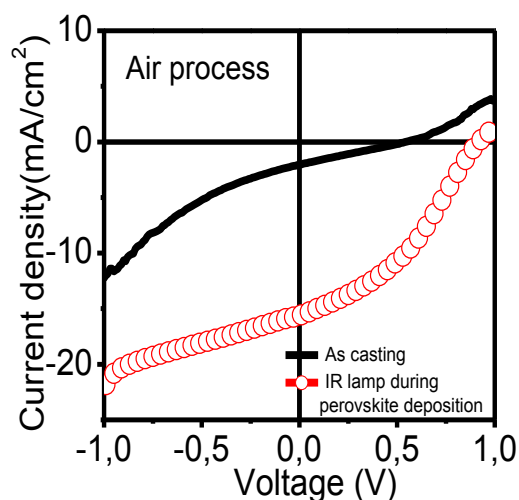


Figure 5.5. Current-density curves of perovskite solar cells performed under air conditions with high relative humidity ($RH > 60\%$) using the thermal treatment and as casting method for perovskite deposition.

The device performances obtained with perovskite solar cells fabricated under air conditions with the as casting method exhibit extremely poor photovoltaic performances. The photocurrent values are very low ($J_{sc} \sim 2.01 \text{ mA/cm}^2$) together with a low open circuit voltage ($V_{oc} \sim 0.54 \text{ V}$) and low fill factor ($FF \sim 0.25$) leading to a PCE value of 0.27%.

Air process	Voc (V)	Jsc (mA/cm²)	FF	Rs*cm² (Ω*cm²)	Rsh*cm² (Ω*cm²)	Efficiency (%)
As casting	0.54	2.01	0.25	120	50	0.27
Thermal treatment during perovskite deposition	0.92	15.63	0.38	38	210	5.46

Table 5.1. Device performance of the best perovskite solar cell using the thermal treatment during perovskite deposition and comparison to the as casting method.

By contrast, we observed a marked improvement on the devices performances by using the thermal treatment. The current density (J_{sc}) and open-circuit voltage (V_{oc}) values were drastically increased from 2.01 mA/cm² to 15.63 mA/cm² and from 0.54 V to 0.92 V respectively along with an increase in the fill factor (FF) from 0.25 to 0.38 leading to a PCE value up to 5.46%.

We also observed that series resistances (R_s) values were decreased from 120 Ω*cm² to 38 Ω*cm² indicating a reduction in the resistance of the semiconductor bulk which suggests a better connection between perovskite and the interfacial layers. On the other hand, shunt resistances (R_{sh}) values were significantly increased from 50 Ω*cm² to 210 Ω*cm² suggesting a higher resistance shunting pathways due to the improved contact between the ETL and HTL with a more uniform perovskite films. Moreover, under a small applied bias voltage the PSCs performed with the thermal method have smaller leakage current in comparison to the PSCs performed with the as casting method which is directly linked with the shunt resistance of the device [13-14]. A better perovskite film quality with high fractional surface coverage contributes also to the photon absorption[15].

The results of the statistical analysis of the photovoltaic parameters obtained from 6 devices fabricated under air condition with both processing conditions are illustrated in Figure 5.6. The distribution of the data is represented by a box plot which is a standardized way for graphically depicting groups of numerical data through their quartiles. The spacing between the different parts of the box indicate the degree of dispersion in the data whereas the end whiskers represent the minimum and maximum of all the data indicating variability outside the upper and lower quartiles. We can clearly observe that the devices fabricated with the thermal

treatment exhibit high degree of reproducibility with small degree of dispersion as illustrated in Figure 5.6.

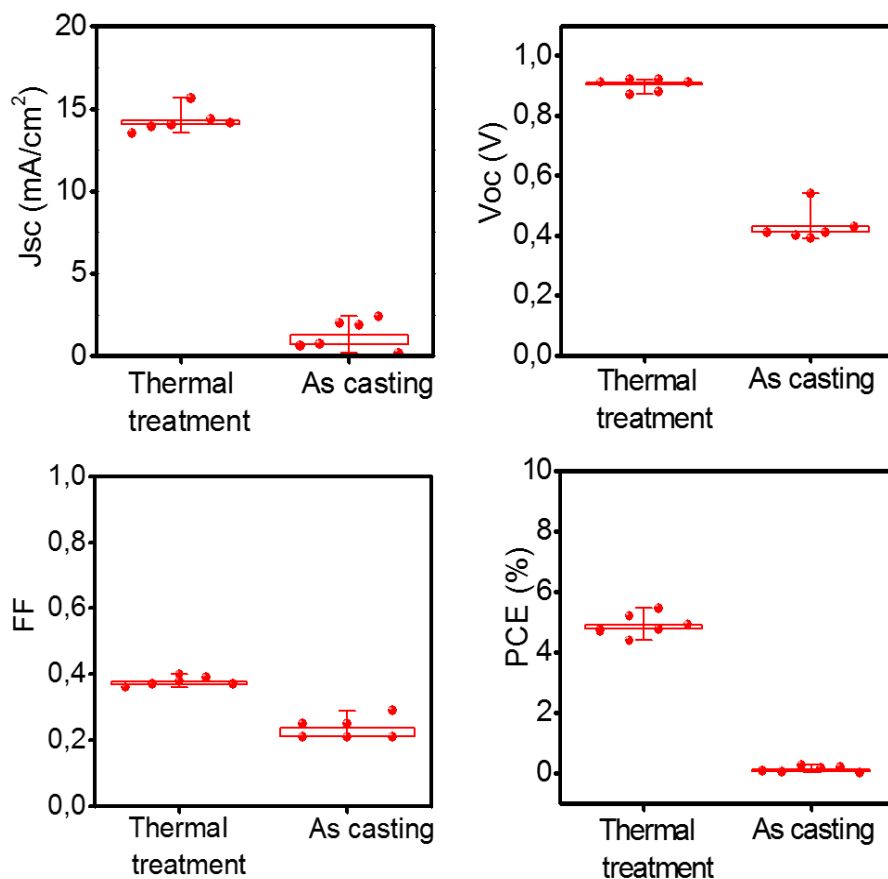


Figure 5.6. Box chart of photovoltaic parameters of a series of 6 perovskite solar cells fabricated under humid conditions.

The average and the standard deviation values of photovoltaic parameters illustrated in Table 5.2 reveal that PSCs with the thermal treatment exhibit extremely low standard deviations.

RH > 60 %	Voc (V)	Jsc (mA/cm ²)	FF	Efficiency (%)
As casting	0.43 ± 0.03	1.3 ± 0.80	0.23 ± 0.02	0.13 ± 0.08
Thermal treatment during perovskite deposition	0.90 ± 0.01	14.39 ± 0.56	0.37 ± 0.01	4.91 ± 0.27

Table 5.2. Device performance of the average of 6 perovskite solar cells using the thermal treatment during perovskite deposition in comparison to the as casting.

By contrast, all the devices fabricated with the as casting method to deposit perovskite thin films under humid conditions does not show diode characteristics or exhibit extremely poor photovoltaic performance with high uncertainty in their performances proving the no viability of those devices. This is mainly due to the bad film quality and low fractional surface coverage values as previously observed in the Section 5.3.1 leading to more randomized performances.

In this section, we presented a thermal treatment during perovskite spin coating which successfully allows the fabrication of perovskite solar cells in humid environment giving efficiencies up to 5.46% with high degree of reproducibility. However, these devices have been prone to exhibit a notable parasitic resistances in their performances with low and high R_{sh} and R_s respectively in comparison to the literature [2,15-16] leading to reduced PCE values.

5.3.3 Effect of perovskite thickness: morphology analysis and device performances of perovskite solar cells

One of the key variables in the fabrication of solar cells using hybrid perovskite as absorber material is the optimization of the processing conditions. In particular, the thickness of perovskite films employed has a strong influence on the film morphology and consequently on the device performances [15,17-18]. In this section, analysis of perovskite film thicknesses correlated to photovoltaic measurements were studied.

First, we characterized the morphology of perovskite thin films with different thicknesses deposited under air conditions using the thermal treatment during the deposition. We deposited mixed halide $CH_3NH_3PbI_{(3-x)}Cl_x$ by spin-coating technique on the top of PEDOT: PSS coated indium tin oxide (ITO) substrates. The perovskite films thickness was controlled by using different spin speeds (3000 rpm, 1500 rpm and 800 rpm) for a 30 seconds spin-coating time to obtain thicknesses of 400 nm, 800 nm and 1000 nm respectively (Figure 5.7). Note that the thickness used in the previous section was 400 nm following previous reports in the literature [17,19].

Figure 5.8 shows the SEM images (low magnification x5500 and high magnification x25000) of 400, 800 and 1000 nm perovskite films.

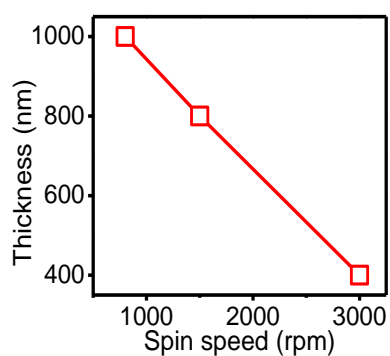


Figure 5.7. Dependence of perovskite layer thickness as a function of spin-coating rotation speed.

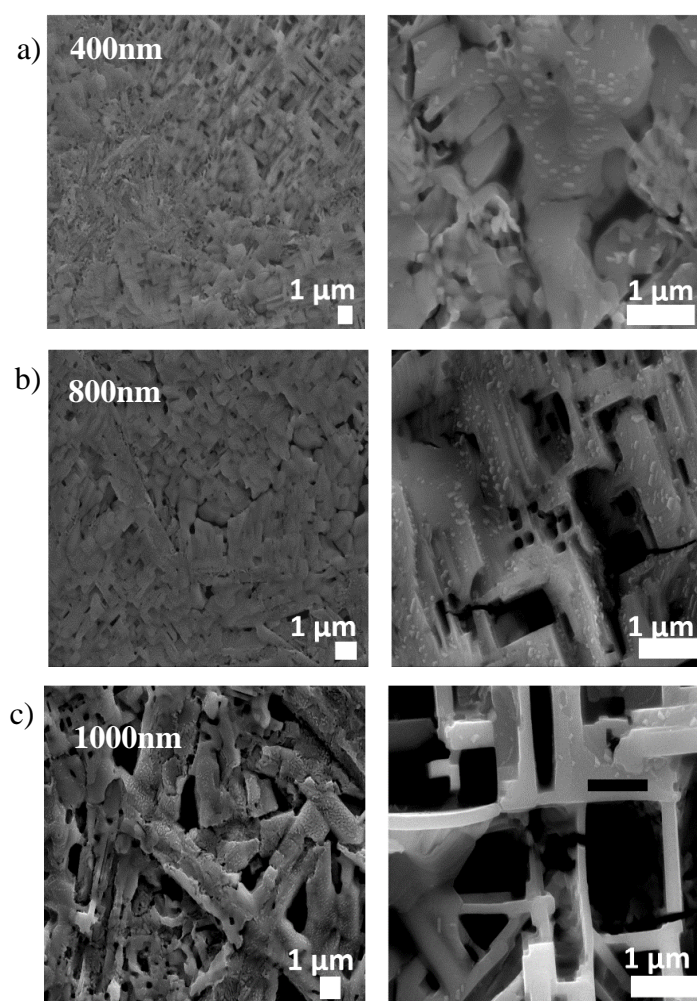


Figure 5.8. SEM images (low and high magnification) of $\text{CH}_3\text{NH}_3\text{PbI}_{(3-x)}\text{Cl}_x$ films with different thickness deposited under air conditions using the thermal treatment. a) 400 nm; b) 800 nm; c) 1000 nm.

We can clearly observe a degradation on the morphology with thicker perovskite film. SEM images show that 1000 nm perovskite films do not cover the entire substrate involving a larger presence of voids and pinholes (Figure 5.8c).

By contrast, the morphology with thinner perovskite films, 400 and 800 nm, exhibits better uniformity and better coverage with a low number of voids and pinholes (Figure 5.8a and Figure 5.8b). Nevertheless, we also observed that thicker perovskite films exhibited larger grain size in comparison to thinner layers. This observation is in good agreement with previous reports in the literature which confirm the dependence of the grain size with the film thickness in where thicker layers induce larger crystalline domains [17].

Figure 5.9 illustrates the fractional surface coverage values estimated from SEM analysis in where the coverage values are gradually decreased from 95% to 90% and finally to 75 % with 400 nm, 800 nm and 1000 nm respectively.

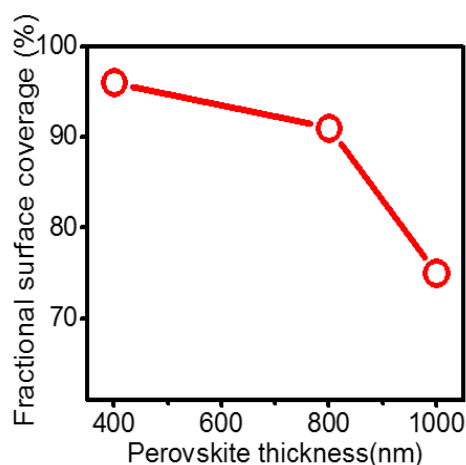


Figure 5.9. Dependence of the fractional surface coverage percentage as a function of perovskite thickness film extracted from Image J and SEM images illustrated in Figure 5.8.

AFM top view images of perovskite thin films with different thickness (400 nm, 800 nm and 1000 nm) are illustrated in Figure 5.10. As expected, we can clearly observe a rougher film with the presence of voids and pinholes with thicker perovskite thin films. The root-mean-square roughness values (Figure 5.11) were extracted from the AFM images of perovskite films giving R_{rms} values of 36 nm, 76 nm and 120 nm with 400 nm, 800 nm and 1000 nm film thick respectively.

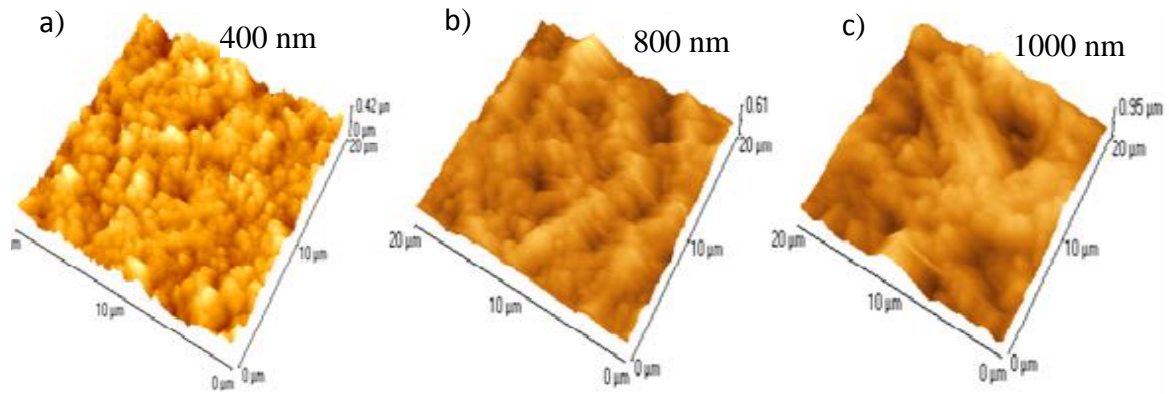


Figure 5.10. AFM top view images of perovskite thin films with different perovskite films thicknesses: a) 400 nm, b) 800 nm and 1000 nm.

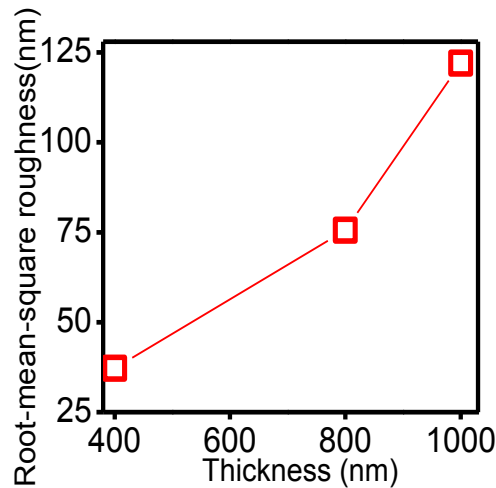


Figure 5.11. Root-mean-square roughness for perovskite thin film as a function of the thin films thickness.

In order to correlate the previous observations with the photovoltaic device performances, we fabricated perovskite solar cells following the device structure illustrated in Figure 5.4.

Figure 5.12 shows the current density-voltage (J-V) characteristics of the devices fabricated with the thermal treatment in air with 400, 800 and 1000 nm perovskite thick films.

The best photovoltaic parameters of those devices are summarized in Table 5.3.

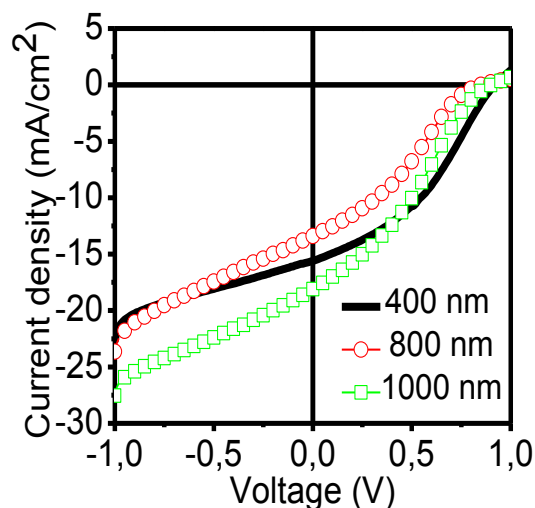


Figure 5.12. Current-density curves of the best perovskite solar cells performed under high relative humidity (RH) with different perovskite thicknesses.

Thickness perovskite (nm)	V_{oc} (V)	J_{sc} (mA/cm ²)	FF	$R_s \cdot \text{cm}^2$ ($\Omega \cdot \text{cm}^2$)	$R_{sh} \cdot \text{cm}^2$ ($\Omega \cdot \text{cm}^2$)	Efficiency (%)
400	0.92	15.63	0.38	38	210	5.46
800	0.85	13.30	0.31	39	120	3.50
1000	0.90	18.11	0.31	35	150	5.05

Table 5.3. Device performance of the best perovskite solar cell using different perovskite thicknesses: 400 nm, 800 nm and 1000 nm.

First, we can observe that the open circuit voltage (V_{oc}) remains almost unchanged for different perovskite thicknesses with values around 0.9 V. The current-density (J_{sc}) values are varied without any trend from 15.63 mA/cm² (400 nm) to 13.30 mA/cm² (800 nm) and 18.11 mA/cm² (1000 nm) respectively. Series resistance (R_s) values are slightly decreased from 38 $\Omega \cdot \text{cm}^2$ (400 nm) and 39 $\Omega \cdot \text{cm}^2$ (800 nm) to 35 $\Omega \cdot \text{cm}^2$ (1000 nm) while the shunt resistances (R_{sh}) values are decreased from 210 $\Omega \cdot \text{cm}^2$ (400 nm) to 120 $\Omega \cdot \text{cm}^2$ (800 nm) and 150 $\Omega \cdot \text{cm}^2$ (1000 nm) respectively. We also observed a prominent S-shape kink in the J-V curves illustrated in Figure 5.12, which becomes more pronounced with thicker film thicknesses suggesting a deterioration of the charge extraction as thickness increases [20-22]. The decrease in the shunt resistance might result from the increased charge recombination driven by the notable presence of voids and pinholes in thicker perovskite films thicknesses leading to a direct contact between electron and hole transport layers. Consequently, the fill factor values are decreased from 0.38

(400 nm) to 0.31 (800 nm and 1000 nm) with PCE values of 5.46% (400 nm) to 3.50 % (800 nm) and 5.05% (1000 nm) respectively.

Perovskite film thickness around 1000 nm has been prone to significant roughness with low fractional surface coverage values however, exhibited device performances comparable with the obtained with thinner layers such as 400 nm. This observation may be related to the larger crystal grain size in thicker films as previously observed in Figure 5.8. Notwithstanding, due to its bad uniformity, worse average devices performances with higher uncertainty values were obtained. Table 5.4 illustrates the device performances of the average 6 perovskite solar cells showing the average and standard deviations values.

From these measurements, we observed that the average Voc value remains almost unchanged showing the same trend as observed in Figure 5.12. The average current density values are again varied without any trend with the thickness however, a drastic increase was observed in the standard deviation of Jsc with values around ± 0.5 (400 nm), ± 1.87 (800 nm), and ± 4.97 (1000 nm) mA/cm² respectively. The average fill factor values slightly decreased with the thickness from 0.36 (400 nm) to 0.29 (800 nm and 1000 nm). Consequently, the average PCE values are decreased as thickness increases with values of 5.05%, 2.54% and 3.42% with standard deviations of $\pm 0.1\%$, 0.56% and $\pm 1.39\%$ for 400 nm, 800 nm and 1000 nm respectively.

Thickness Perovskite (nm)	V_{oc} (V)	J_{sc} (mA/cm²)	FF	Efficiency (%)
400	0.83 \pm 0.02	13.4 \pm 0.5	0.36 \pm 0.01	5.05 \pm 0.1
800	0.81 \pm 0.04	11.03 \pm 1.87	0.28 \pm 0.01	2.54 \pm 0.56
1000	0.87 \pm 0.01	13.05 \pm 4.97	0.29 \pm 0.01	3.42 \pm 1.39

Table 5.4. Device performance of the average of 6 perovskite solar cells using different perovskite thicknesses. Averages standard deviation values are reported.

Therefore, we clearly observed a degradation on the devices performances with thicker perovskite thickness resulting in poor devices performances with higher standard deviations. This is driven by the strong impact of the thickness on the film morphology in where thick perovskite films leads to a bad perovskite morphology causing a detrimental impact on the devices performances along with more randomized performances[10,17,23]. Here, we

optimized the conditions for the thickness of PSCs fabricated under humid conditions with a thermal treatment during perovskite deposition to obtain reproducible devices. The best performances were obtained with 400 nm perovskite films leading to an average PCE value of $5.05 \pm 0.1\%$.

5.3.4 Effect of annealing temperature on mixed halide perovskite: morphology analysis and device performances of perovskite solar cells

One of the major advantages of the inorganic-organic perovskite material is its simple method of deposition. Only a simple heating step with an appropriate temperature is necessary to remove the residual solvents and finally convert the precursor to the crystalline perovskite. In this section, the analysis of different annealing temperature (80 °C, 100 °C and 120 °C) on mixed halide perovskite thin films was correlated to the photovoltaic measurements.

We first characterized the morphology of perovskite thin films on ITO/PEDOT:PSS substrates annealed at temperatures of 80 °C, 100 °C and 120 °C during 120, 90 and 60 minutes respectively.

SEM images of perovskite thin films reveal that the annealing temperature has a strong impact on the film morphology (Figure 5.13).

The SEM images show an increase on the grain size with the temperature. The mean grain size at 80 °C is about 1 μm and reaches 4 μm at 120 °C. These observations are in good agreement with previous reports in the literature [15,24-26] which suggest that annealing temperature higher than 120 °C can lead to an increase of the grain size but also to the decomposition of perovskite thin films (additional formation of PbI_2).

The fractional surface coverage of perovskite thin films shows a significant modification from 91% (80 °C) to 79% (120 °C) exhibiting bad uniformity with the presence of large voids on the film as illustrated in Figure 5.14. However, for 100 °C, the perovskite thin films exhibit good uniformity and good coverage with a fractional surface coverage value of 96%.

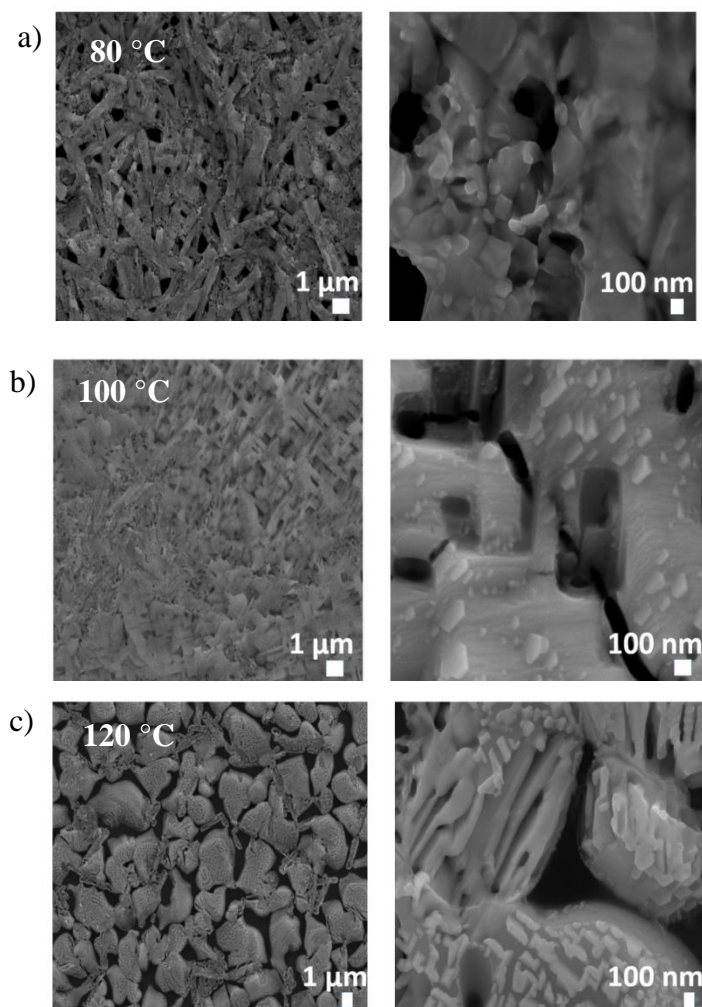


Figure 5.13. SEM images of perovskite thin films (low and high magnification) deposited under high relative humidity ($RH > 60\%$) using different annealing temperatures. a) 80 °C. b) 100 °C. c) 120 °C.

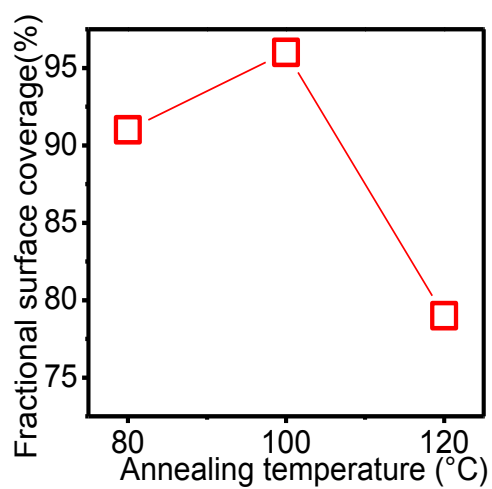


Figure 5.14. Fractional surface coverage percentage as a function of perovskite annealing temperature.

In order to correlate these observations with the photovoltaic performances of perovskite solar cells, we fabricated perovskite solar cells following the structure illustrated in Figure 5.4.

The current density-voltage (J-V) characteristics of the best devices fabricated with different annealing temperature are illustrated in Figure 5.15. The photovoltaic parameters of these devices are summarized in Table 5.5.

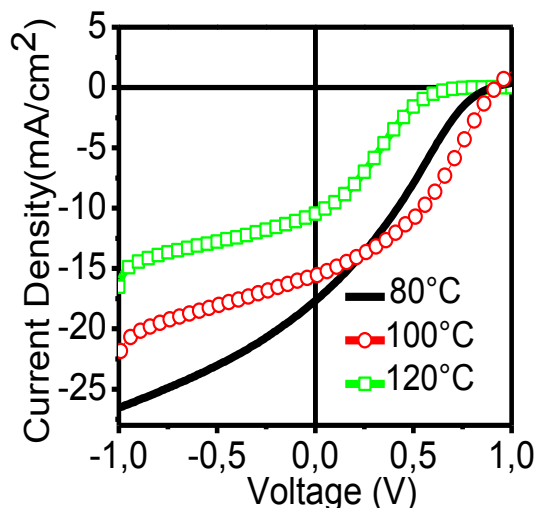


Figure 5.15. Current-density curves of the best perovskite solar cells performed under high relative humidity (RH) with annealing temperatures of 80 °C, 100 °C and 120 °C.

Annealing Temperature	V_{oc} (V)	J_{sc} (mA/cm ²)	FF	R_s *cm ² (Ω *cm ²)	R_{sh} *cm ² (Ω *cm ²)	Efficiency (%)
80 °C	0.9	17.62	0.26	40	134	4.12
100 °C	0.92	15.63	0.38	38	210	5.46
120 °C	0.81	10.32	0.18	42	240	1.50

Table 5.5 Device performance of the best perovskite solar cells using different annealing temperatures.

We can observe that perovskite solar cells using annealing temperatures of 80 °C and 100 °C, have similar photovoltaic performances with PCE values of 4.12 % and 5.46 % respectively. This can be explained by the similarity on the film morphology achieved with films annealed at 80 °C and 100 °C, resulting in similar V_{oc} and J_{sc} values. However, the V_{oc} and J_{sc} obtained with 120 °C are significantly decreased with the temperature from 0.9 V to 0.81 V and from 17.62 mA/cm² to 10.32 mA/cm² respectively leading to a poor PCE values of 1.50%. Moreover, as the annealing temperature increases, for voltages larger than 0.5 V limitations by the series

resistance become more apparent leading to a prominent S-shape kink in the J-V curves (Figure 5.17) suggesting a deterioration of the charge extraction[20-22].

Table 5.6 illustrates the devices performances of the average of 6 perovskite solar cells with different annealing temperatures.

Annealing temperature (°C)	V_{oc} (V)	J_{sc} (mA/cm ²)	FF	Efficiency (%)
80	0.8 ± 0.09	6.16 ± 4.58	0.30 ± 0.03	1.46 ± 1.06
100	0.83 ± 0.02	13.4 ± 0.5	0.36 ± 0.01	5.05 ± 0.1
120	0.7 ± 0.04	7.80 ± 2.06	0.2 ± 0.01	1.10 ± 0.31

Table 5.6. Device performance of the average of 6 perovskite solar cell using different perovskite thicknesses showing the averages and standard deviation values.

We clearly observed that 100 °C shows better photovoltaic performances in terms of reproducibility with smaller standard deviations. The average current density is decreased from 13.4 mA/cm² (100 °C) to 6.16 mA/cm² (80 °C) and 7.80 mA/cm² (120 °C) with a significant increase on the standard deviation values from ± 0.5 to ± 4.58 and ± 2.06 mA/cm² respectively. The average fill factor value is decreased from 0.36 ± 0.01 (100 °C) to 0.30 ± 0.03 (80 °C) and 0.20 ± 0.01 (80 °C). Consequently, the average of the PCE values is significantly decrease from $5.05 \pm 0.1\%$ (100 °C) to $1.46 \pm 1.06\%$ and then $1.10 \pm 0.31\%$ (80 °C and 120 °C) respectively.

Here, we can state that a suitable temperature annealing should be chosen to ensure the evaporation of the solvent and the crystallization of perovskite material in order to obtain good perovskite film morphology under humid conditions. The best devices performances were obtained with 400 nm perovskite films annealed at 100 °C. Annealing temperature around 80 °C has probe to be the optimum annealing temperature to obtain good perovskite film quality in terms of coverage however, it provides worse devices performances in comparison to 100 °C.

Therefore, in this section we optimized conditions for perovskite solar cells fabricated under humid conditions. We have found that the optimum annealing temperature and thickness are 100 °C and 400 nm respectively resulting in a power conversion efficiencies around 5.46% with high degree of reproducibility. However, notable parasitic resistances lead to a reduced PCE values in comparison to reported values nowadays in the literature [16,20-22].

5.4 Perovskite solar cells processed under nitrogen ambient

5.4.1 Comparison of perovskite solar cells fabricated under different atmospheres

The majority of perovskite solar cells reported are fabricated under nitrogen ambient to maintain a controlled and constant atmosphere without humidity.

In this study, we fabricated perovskite solar cells under a controlled nitrogen atmosphere (Glove Box –P ~ 3.8 mBar, H₂O < 0.1ppm, O₂ ~ 0.5ppm) and we compare to the air process. The thickness and annealing temperature for perovskite deposition used in this study were 400 nm and 100 °C respectively following the optimum conditions of the previous section and previous reports in the literature [4,27-28].

Figure 5.16 shows the current density-voltage (J-V) curves of the best device fabricated under air condition and (RH > 60%) and in the nitrogen atmosphere.

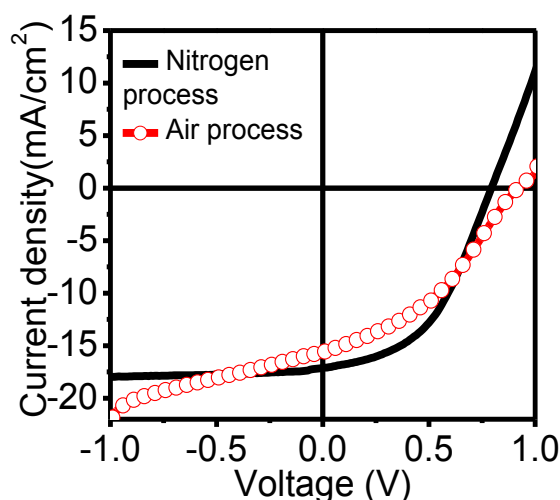


Figure 5.16. Current-density curves of the best perovskite solar cells performed under different atmospheres, humid environment and nitrogen atmosphere.

The best photovoltaic parameters of these devices are summarized in Table 5.7.

Atmospheres	V _{oc} (V)	J _{sc} (mA/cm ²)	FF	R _s *cm ² (Ω*cm ²)	R _{sh} *cm ² (Ω*cm ²)	Efficiency (%)
Air process	0.92	15.63	0.38	38	218	5.46
N ₂ process	0.79	17.11	0.47	17	3545	6.35

Table 5.7. Device performance of the best perovskite solar cells fabricated under different atmospheres

From the Figure 5.16 and Table 5.7, we can clearly observe a marked improvement on the devices performances fabricated under nitrogen conditions. The J_{sc} values are increased from 15.63 mA/cm² to 17.11 mA/cm² and fill factor (FF) is also increased from 0.38 to 0.47; which resulted in an enhancement of about 15% for PCE from 5.46% to 6.35%.

R_s values are significantly decreased from 38 Ω*cm² to 17 Ω*cm² indicating a better contact between perovskite and the interface layers induced by a better control on the perovskite deposition. These observations suggest an improved interfacial connection reducing thus the series resistances and improving charge extraction. Moreover, R_{sh} values are drastically increased from 218 Ω*cm² to 3545 Ω*cm² indicating lower charge carrier recombination.

This overall improvement on the devices performances is mainly due to fact that processing solar cells under a nitrogen conditions facilitate the development of perovskite films under a constant and inert atmosphere (P ~ 3.8mBar, H₂O < 0.1ppm, O₂ ~ 0.5ppm) which tremendously improves the perovskite film characteristics. As previously reported, perovskite layers cast in air conditions exhibit smaller grain sizes in comparison to those cast in N₂ related to a more efficient perovskite nucleation, probably due to the presence of moisture in the air[12,29-30]. Thus, large grain size reduce the total grain boundary leading to a reduction in the film defects and consequently the charge recombination due to the reduced charge trap density[31]. Moreover, larger grain sizes also improves the quality of the contact between perovskite and the interfacial layers[15].

Table 5.8 and Figure 5.17 show the statistical analysis of the photovoltaic parameters of a series of 6 perovskite solar cells fabricated under different atmospheres (air and nitrogen).

Atmospheres	V_{oc} (V)	J_{sc} (mA/cm ²)	FF	Efficiency (%)
Air process	0.90 ± 0.01	14.39 ± 0.56	0.37 ± 0.01	4.91 ± 0.27
N ₂ process	0.70 ± 0.08	14.07 ± 1.5	0.42 ± 0.34	4.34 ± 1.12

Table 5.8. Device performance of the average of 6 perovskite solar cell using different perovskite thicknesses showing the averages and standard deviation values fabricated under different atmospheres.

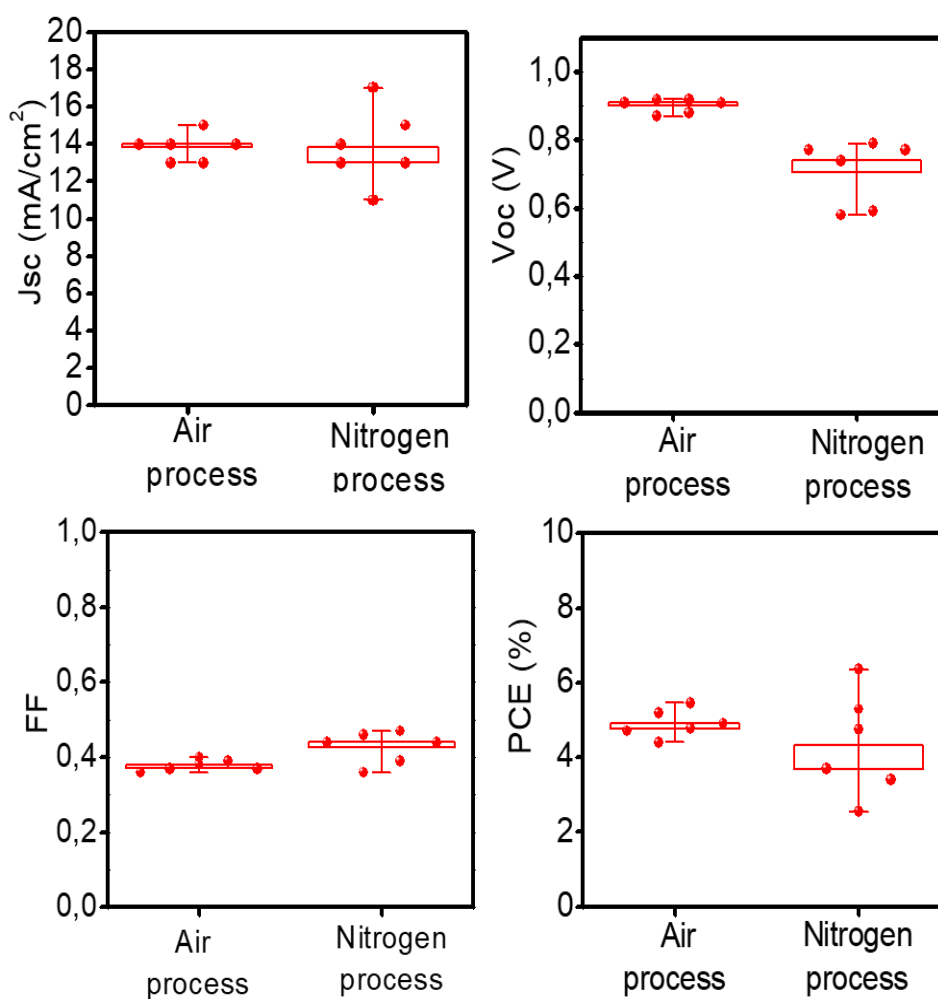


Figure 5.17. Box chart of photovoltaic parameters of a series of 6 perovskite solar cells fabricated under nitrogen and air conditions

We achieved very similar average PCE values processing perovskite solar cells under air and nitrogen conditions with values of 4.91 ± 0.27 % and 4.34 ± 1.12 % respectively as illustrated in Figure 5.17.

The devices fabricated under air condition exhibit a higher degree of reproducibility with smaller standard deviation for parameters such as: $J_{sc} = 14.39 \pm 0.56 \text{ mA/cm}^2$, $V_{oc} = 0.9 \pm 0.01 \text{ V}$, $FF = 0.37 \pm 0.01$ and $PCE = 4.91 \pm 0.27$ in comparison to $14.07 \pm 1.5 \text{ mA/cm}^2$, $0.70 \pm 0.08 \text{ V}$, 0.42 ± 0.34 and finally a PCE of $4.34 \pm 1.12 \%$ respectively.

This proves that the technique used in this thesis to fabricate perovskite solar cells under humid environment exhibit good reliability in PSCs performances. However, as previously observed, the device performances of perovskite solar cells fabricated in air are limited by the parasitic resistances leading to reduced PCEs values in comparison to the reported ones nowadays in the literature [16,20-22].

5.4.2 Improvement of solar cells processed in nitrogen via HTL modification

Hole transporting material (HTM) plays an important role on the perovskite solar cell performances in terms of charge transport and recombination[32-34].

In this thesis, we used the common PEDOT: PSS (poly (3, 4- ethylenedioxythiophene): poly (styrenesulfonic acid)) which is a conjugated polymer widely used as HTL in organic optoelectronics. However, it has been reported that the PEDOT: PSS exhibits poor electrical properties like low conductivity, hindering the charge transport within the layer[50].

In order to improve the solar cells performances, we modified the electrical properties of the PEDOT: PSS. In particular, we modified the conductivity of the material by the addition of a polar and high boiling point organic solvent into the PEDOT: PSS solvent. By adding 5% DMSO to PEDOT: PSS solution, we were able to increase the conductivity values from original values of 0.022 S/cm to 4.27 S/cm.

Morphological characterization was carried out by AFM analysis on PEDOT: PSS thin films deposited on glass/ITO substrates (Figure 5.18).

The root mean-square roughness value of PEDOT: PSS are 1.9 nm and 3.5 nm without and with DMSO solvent addition respectively. We obtain an increase of the grain size for the high conductivity PEDOT: PSS of a factor 2.

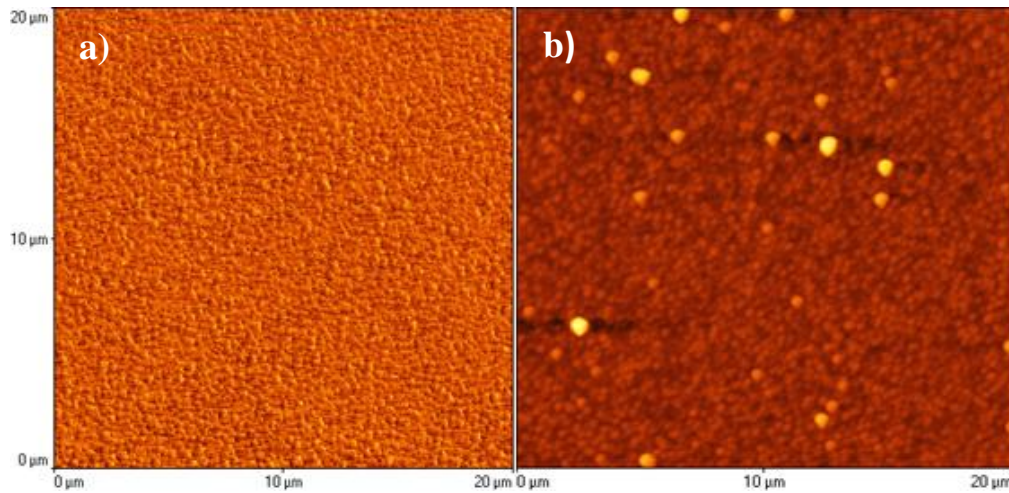


Figure 5.18. Top AFM images PEDOT: PSS films a) without additional treatment b) with DMSO treatment.

In order to examine the effect of DMSO addition in PEDOT: PSS solution on the device performances, inverted structure devices were fabricated.

Figure 5.19 shows the current density-voltage (J-V) curves of the best device fabricated under a controlled atmosphere using PEDOT: PSS modification (5% DMSO addition) in comparison to the standard PEDOT: PSS.

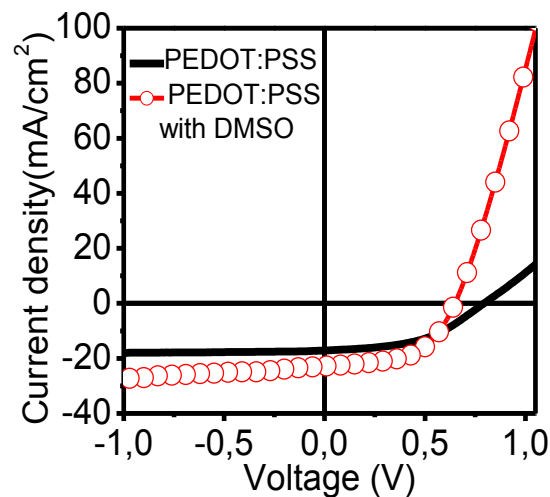


Figure 5.19. Device performance of the best perovskite solar cells using pristine and 5% DMSO in PEDOT: PSS solution.

The best photovoltaic parameters of this solar cell are summarized in Table 5.9.

	V_{oc} (V)	J_{sc} (mA/cm ²)	FF	$R_s * cm^2$ ($\Omega * cm^2$)	$R_{sh} * cm^2$ ($\Omega * cm^2$)	Efficiency (%)
PEDOT:PSS	0.79	17.11	0.47	17	3545	6.35
PEDOT:PSS with DMSO modification	0.65	22.82	0.55	3.45	150	8.16

Table 5.9. Device performance of the best perovskite solar cells fabricated under nitrogen conditions with PEDOT: PSS modification.

We can clearly observe a marked improvement on the device performances with a 5% addition of DMSO on PEDOT: PSS solution leading to PCE values up to 8.16%. Series resistance (R_s) values are greatly decreased from 17 $\Omega * cm^2$ to 3.45 $\Omega * cm^2$. DMSO addition into the HTL (PEDOT:PSS), leads to a more conductive film which results in a decrease in the series resistances values suggesting a more efficient charge transfer between the perovskite and DMSO-treated PEDOS:PSS. By contrast, there is a drop in the shunt resistance which may be related to the changing morphology of the PEDOT: PSS layer which exhibits rougher film thickness. As the perovskite /PEDOT: PSS interface becomes rougher, surface recombination are higher having a direct impact on the shunt resistances values [20-22,35].

The above observations lead to an increase on the J_{sc} and FF values from 17.11 mA/cm² to 22.82 mA/cm² and from 0.47 to 0.55 respectively. Thus, we can see clearly and obvious improvement on the device performance by the addition of DMSO on the HTL.

We succeed in reducing the overall parasitic resistances in the device performances of perovskite solar cells by increasing the conductivity of PEDOT: PSS which hinders the charge transport leading to a PCE values up to 8.16%.

5.4.3 Stability of perovskite solar cells fabricated under a controlled atmosphere

One major challenge to commercialize perovskite solar cells is their environmental instability. Degradation factors, like thermal and chemical instabilities, moisture and oxygen, extreme light exposure can strongly affect the stability of perovskite solar cells.

As it was mentioned before, most of the perovskite solar cells are fabricated under a controlled atmosphere with an inert gas. However, the characterization of these photovoltaic devices are

carried out under ambient conditions in where a significant performances degradation with time is usually observed and even if the samples are encapsulated. Some reports have attributed the origin of such degradation in the devices performances to UV light exposure and UV-induced heating damage to the active layer[36-38].

For this reason, good encapsulation of perovskite devices is of critical importance for increasing device life time. First, in order to evaluate the reliability of the encapsulation with such resist for perovskite solar cells fabricated in nitrogen, we measured the power-voltage characteristics before and after the encapsulation as illustrated in Figure 5.20.

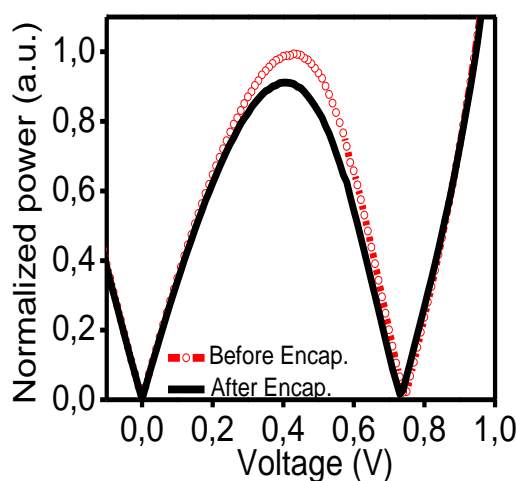


Figure 5.20. Normalized power –voltage dependent of perovskite solar cells before and after encapsulation

We can observe that the open-circuit voltage of the perovskite solar cells does not change after the encapsulation of such devices. On the other hand, the maximum power (P_{max}) achieved with the encapsulated perovskite solar cells show a slight decrease in their values of a 10% indicating thus, a quite efficient encapsulation.

Stability tests were performed in order to analyze the time and ambient effect on the device performances. We performed continuous measurements on the device by monitoring the power-voltage characteristics under light illumination in atmospheric condition (25 °C, 60 % humidity) during 24 hours (Figure 5.21).

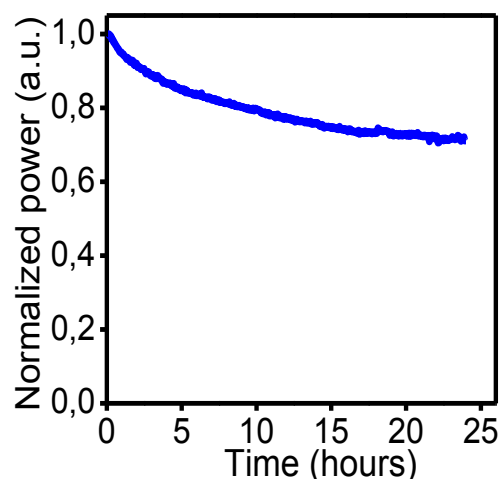


Figure 5.21. Stability as a function of time for encapsulated solar cells under light illumination.

The power- time characteristics exhibit a degradation in the maximum power of a 30% after 24 hours highlighting therefore low stability under light illumination and humid conditions.

Here, we also performed stability test on perovskite solar cells fabricated under humid conditions, however these devices were rapidly degraded with the time. This observation is in good agreement with the fact that the morphology of perovskite films may influence the stability of the devices performances in air[39].

5.5 Conclusion

In this chapter, we presented the fabricated perovskite solar cells in air and in N_2 ambient. We analyzed the thicknesses and the annealing temperature effect for the perovskite thin films in order to optimize the processing conditions. The optimum condition for air deposition is a 400 nm-thick perovskite film annealed at 100 °C leading to solar cells efficiencies values up to $\sim 5\% \pm 0.3\%$. Finally, by modifying the HTL of perovskite solar cells by adding DMSO to PEDOT: PSS solution, we could achieve around 8% PCE solar cells fabricated under a controlled atmosphere.

5.6 References

- [1] J. Troughton, K. Hooper, T.M. Watson, Humidity resistant fabrication of CH₃NH₃PbI₃ perovskite solar cells and modules, *Nano Energy*. 39 (2017) 60–68.
- [2] B. Jeong, S.M. Cho, S.H. Cho, J.H. Lee, I. Hwang, S.K. Hwang, J. Cho, T.-W. Lee, C. Park, Humidity controlled crystallization of thin CH₃NH₃PbI₃ films for high performance perovskite solar cell, *Phys. Status Solidi RRL–Rapid Res. Lett.* 10 (2016) 381–387.
- [3] F. Li, M. Liu, Recent efficient strategies for improving the moisture stability of perovskite solar cells, *J. Mater. Chem. A*. 5 (2017) 15447–15459.
- [4] H.-S. Ko, J.-W. Lee, N.-G. Park, 15.76% efficiency perovskite solar cells prepared under high relative humidity: importance of PbI₂ morphology in two-step deposition of CH₃NH₃PbI₃, *J. Mater. Chem. A*. 3 (2015) 8808–8815.
- [5] J. You, L. Meng, T.-B. Song, T.-F. Guo, Y.M. Yang, W.-H. Chang, Z. Hong, H. Chen, H. Zhou, Q. Chen, others, Improved air stability of perovskite solar cells via solution-processed metal oxide transport layers, *Nat. Nanotechnol.* 11 (2016) 75.
- [6] Q. Tai, P. You, H. Sang, Z. Liu, C. Hu, H.L. Chan, F. Yan, Efficient and stable perovskite solar cells prepared in ambient air irrespective of the humidity, *Nat. Commun.* 7 (2016) 11105.
- [7] M. Shirayama, H. Kadowaki, T. Miyadera, T. Sugita, M. Tamakoshi, M. Kato, T. Fujiseki, D. Murata, S. Hara, T.N. Murakami, others, Optical transitions in hybrid perovskite solar cells: ellipsometry, density functional theory, and quantum efficiency analyses for CH₃NH₃PbI₃, *Phys. Rev. Appl.* 5 (2016) 014012.
- [8] I. Montes-Valenzuela, F. Pérez-Sánchez, A. Morales-Acevedo, Structural, optical and photoluminescence properties of hybrid metal–organic halide perovskite thin films prepared by a single step solution method, *J. Mater. Sci. Mater. Electron.* (2018) 1–7.
- [9] Y. Tidhar, E. Edri, H. Weissman, D. Zohar, G. Hodes, D. Cahen, B. Rybtchinski, S. Kirmayer, Crystallization of methyl ammonium lead halide perovskites: implications for photovoltaic applications, *J. Am. Chem. Soc.* 136 (2014) 13249–13256.
- [10] M.M. Lee, J. Teuscher, T. Miyasaka, T.N. Murakami, H.J. Snaith, Efficient hybrid solar cells based on meso-superstructured organometal halide perovskites, *Science*. (2012) 1228604.
- [11] H. Zhou, Q. Chen, G. Li, S. Luo, T. Song, H.-S. Duan, Z. Hong, J. You, Y. Liu, Y. Yang, Interface engineering of highly efficient perovskite solar cells, *Science*. 345 (2014) 542–546.
- [12] K.K. Bass, R.E. McAnally, S. Zhou, P.I. Djurovich, M.E. Thompson, B.C. Melot, Influence of moisture on the preparation, crystal structure, and photophysical properties of organohalide perovskites, *Chem. Commun.* 50 (2014) 15819–15822.
- [13] R.A. Janssen, J. Nelson, Factors limiting device efficiency in organic photovoltaics, *Adv. Mater.* 25 (2013) 1847–1858.
- [14] C. Waldauf, M.C. Scharber, P. Schilinsky, J.A. Hauch, C.J. Brabec, Physics of organic bulk heterojunction devices for photovoltaic applications, *J. Appl. Phys.* 99 (2006) 104503.
- [15] G.E. Eperon, V.M. Burlakov, P. Docampo, A. Goriely, H.J. Snaith, Morphological control for high performance, solution-processed planar heterojunction perovskite solar cells, *Adv. Funct. Mater.* 24 (2014) 151–157.
- [16] J. Burschka, N. Pellet, S.-J. Moon, R. Humphry-Baker, P. Gao, M.K. Nazeeruddin, M. Grätzel, Sequential deposition as a route to high-performance perovskite-sensitized solar cells, *Nature*. 499 (2013) 316.
- [17] D. Liu, M.K. Gangishetty, T.L. Kelly, Effect of CH₃NH₃PbI₃ thickness on device efficiency in planar heterojunction perovskite solar cells, *J. Mater. Chem. A*. 2 (2014) 19873–19881.
- [18] H.S. Jung, N.-G. Park, Perovskite solar cells: from materials to devices, *Small*. 11 (2015) 10–25.
- [19] A. Reinders, P. Verlinden, A. Freundlich, *Photovoltaic solar energy: from fundamentals to applications*, John Wiley & Sons, 2017.
- [20] S. Shao, J. Liu, H.-H. Fang, L. Qiu, G.H. ten Brink, J.C. Hummelen, L.J.A. Koster, M.A. Loi, Efficient Perovskite Solar Cells over a Broad Temperature Window: The Role of the Charge Carrier Extraction, *Adv. Energy Mater.* 7 (2017) 1701305.
- [21] P. Liao, X. Zhao, G. Li, Y. Shen, M. Wang, A new method for fitting current–voltage curves of planar heterojunction perovskite solar cells, *Nano-Micro Lett.* 10 (2018) 5.

- [22] M. Xie, H. Lu, L. Zhang, J. Wang, Q. Luo, J. Lin, L. ba, H. Liu, W.Z. Shen, L. Shi, C.-Q. Ma, Fully Solution-Processed Semi-Transparent Perovskite Solar Cells With Ink-Jet Printed Silver Nanowires Top Electrode (Solar RRL 2/2018), Sol. RRL. 2 (2018) 1770152.
- [23] Z. Xiao, Q. Dong, C. Bi, Y. Shao, Y. Yuan, J. Huang, Solvent annealing of perovskite-induced crystal growth for photovoltaic-device efficiency enhancement, Adv. Mater. 26 (2014) 6503–6509.
- [24] A. Dualeh, N. Tétreault, T. Moehl, P. Gao, M.K. Nazeeruddin, M. Grätzel, Effect of annealing temperature on film morphology of organic–inorganic hybrid perovskite solid-state solar cells, Adv. Funct. Mater. 24 (2014) 3250–3258.
- [25] D. Khatiwada, S. Venkatesan, N. Adhikari, A. Dubey, A.F. Mitul, L. Mohammad, A. Iefanova, S.B. Darling, Q. Qiao, Efficient perovskite solar cells by temperature control in single and mixed halide precursor solutions and films, J. Phys. Chem. C. 119 (2015) 25747–25753.
- [26] Z. Song, S.C. Wathage, A.B. Phillips, B.L. Tompkins, R.J. Ellingson, M.J. Heben, Impact of processing temperature and composition on the formation of methylammonium lead iodide perovskites, Chem. Mater. 27 (2015) 4612–4619.
- [27] W. Nie, H. Tsai, J.-C. Blancon, F. Liu, C.C. Stoumpos, B. Traore, M. Kepenekian, O. Durand, C. Katan, S. Tretiak, others, Critical role of interface and crystallinity on the performance and photostability of perovskite solar cell on nickel oxide, Adv. Mater. 30 (2018) 1703879.
- [28] H. Tsai, R. Asadpour, J.-C. Blancon, C.C. Stoumpos, O. Durand, J.W. Strzalka, B. Chen, R. Verduzco, P.M. Ajayan, S. Tretiak, J. Even, M.A. Alam, M.G. Kanatzidis, W. Nie, A.D. Mohite, Light-induced lattice expansion leads to high-efficiency perovskite solar cells, Science. 360 (2018) 67–70. doi:10.1126/science.aap8671.
- [29] G.E. Eperon, S.N. Habisreutinger, T. Leijtens, B.J. Bruijnaers, J.J. van Franeker, D.W. deQuilettes, S. Pathak, R.J. Sutton, G. Grancini, D.S. Ginger, others, The importance of moisture in hybrid lead halide perovskite thin film fabrication, ACS Nano. 9 (2015) 9380–9393.
- [30] B.J. Bruijnaers, E. Schiepers, C.H. Weijtens, S.C. Meskers, M.M. Wienk, R.A. Janssen, The effect of oxygen on the efficiency of planar p–i–n metal halide perovskite solar cells with a PEDOT: PSS hole transport layer, J. Mater. Chem. A. 6 (2018) 6882–6890.
- [31] L.M. Herz, Charge-carrier mobilities in metal halide perovskites: Fundamental mechanisms and limits, ACS Energy Lett. 2 (2017) 1539–1548.
- [32] N. Marinova, W. Tress, R. Humphry-Baker, M.I. Dar, V. Bojinov, S.M. Zakeeruddin, M.K. Nazeeruddin, M. Grätzel, Light harvesting and charge recombination in CH₃NH₃PbI₃ perovskite solar cells studied by hole transport layer thickness variation, ACS Nano. 9 (2015) 4200–4209.
- [33] D. Bi, L. Yang, G. Boschloo, A. Hagfeldt, E.M. Johansson, Effect of different hole transport materials on recombination in CH₃NH₃PbI₃ perovskite-sensitized mesoscopic solar cells, J. Phys. Chem. Lett. 4 (2013) 1532–1536.
- [34] J. Jiménez-López, W. Cambarau, L. Cabau, E. Palomares, Charge injection, carriers recombination and homo energy level relationship in perovskite solar cells, Sci. Rep. 7 (2017) 6101.
- [35] D. Huang, T. Goh, J. Kong, Y. Zheng, S. Zhao, Z. Xu, A.D. Taylor, Perovskite solar cells with a DMSO-treated PEDOT: PSS hole transport layer exhibit higher photovoltaic performance and enhanced durability, Nanoscale. 9 (2017) 4236–4243.
- [36] T.A. Berhe, W.-N. Su, C.-H. Chen, C.-J. Pan, J.-H. Cheng, H.-M. Chen, M.-C. Tsai, L.-Y. Chen, A.A. Dubale, B.-J. Hwang, Organometal halide perovskite solar cells: degradation and stability, Energy Environ. Sci. 9 (2016) 323–356.
- [37] Y. Han, S. Meyer, Y. Dkhissi, K. Weber, J.M. Pringle, U. Bach, L. Spiccia, Y.-B. Cheng, Degradation observations of encapsulated planar CH₃NH₃PbI₃ perovskite solar cells at high temperatures and humidity, J. Mater. Chem. A. 3 (2015) 8139–8147.
- [38] G. Niu, X. Guo, L. Wang, Review of recent progress in chemical stability of perovskite solar cells, J. Mater. Chem. A. 3 (2015) 8970–8980.
- [39] J.H. Kim, S.T. Williams, N. Cho, C.-C. Chueh, A.K.-Y. Jen, Enhanced environmental stability of planar heterojunction perovskite solar cells based on blade-coating, Adv. Energy Mater. 5 (2015) 1401229.

CONCLUSION AND PERSPECTIVES

The objective of this thesis was to fabricate operational perovskite based field effect transistors (FET) and solar cells.

I) Perovskite based field effect transistors

The goal assigned at Light to Energy team led by Aditya Mohite from Los Alamos National Laboratory (LANL) was to obtain perovskite based FETs working at room temperature. We used the previously developed hot-casting technique by Nie *et al.* [1] to grow continuous, pinhole-free, highly crystalline and millimeter-scale perovskite crystals. We succeeded in obtaining MAPbI₃ perovskite FETs operational at room temperature without need of illumination. We demonstrated the operation of PFETs with gate modulation for the p type carriers. Device simulations were performed by Nicolò Zagni and Muhammad A. Alam in order to understand the obtained performances (10^{-8} A level of current, low mobility of 0.1 cm²/V.s). After consecutive cycles of measurements, we obtained ambipolar transport characteristics where the perovskite's fermi energy can be successfully modulated by the gate voltage allowing both electron and hole transport in the conduction band and valence band respectively. These devices exhibit small hysteresis with few degradation in transport characteristics after consecutive cycles during 14 hours highlighting thus, short-term stability operation. We also investigated systematically the impact of channel dimension and dielectric layer between gate and perovskites. We confirm that higher channel length on PFETs leads to higher number of defects and grain boundaries across the channel inducing higher charge recombination rate resulting thus in lower device performances with a notable hysteresis in their transfer characteristics.

The analysis of the FET characteristics and the capacitance as a function of different dielectrics (SiO₂, Si₃N₄ and HfO₂) show that the fundamental challenge in the literature for the demonstration of perovskite-based FETs is the screening of the gate electric-field by ionic vacancies. By using high-k dielectric as gate insulator we were able to passivate the charge vacancies and obtain the carrier modulation achieving operational field effect transistors at room temperature. However, by using low-k dielectrics such SiO₂ or Si₃N₄ the transfer characteristics exhibit a very weak gate modulation. For SiO₂ as insulator we obtained a large

hysteresis between the forward and reverse scan hindering thus, the extraction of the main device parameters.

Moreover, we employed mixed cation perovskite layer with a stoichiometric ratio of $\text{FA}_{0.75-x}\text{MA}_{0.25}\text{Cs}_x\text{PbI}_3$ with $x=0.05, 0.15$ and 0.25 as active layers on field effect transistors to study the film quality and device performances. The results obtained reveal that the device performances of PFETs are improved with the amount of Cs on the mixed cation system (FA/MA/Cs). Although high quality perovskite films were obtained with $\text{FA}_{0.6}\text{MA}_{0.25}\text{Cs}_{0.15}\text{PbI}_3$ and $\text{FA}_{0.7}\text{MA}_{0.25}\text{Cs}_{0.05}\text{PbI}_3$ any good devices were obtained with those concentrations. However, by employing the optimized stoichiometric ratio as active layer ($\text{FA}_{0.25}\text{MA}_{0.5}\text{Cs}_{0.25}\text{PbI}_3$), we succeed in obtaining PFETs operational at room temperature with small hysteresis, high transconductance, with an Ion/Ioff ratio $>10^4$, short-term stable operation and better degree of reproducibility.

The literature shows the difficulty to obtain FET device based on perovskite (low temperature operation, required illumination, huge hysteresis) and here we fabricate for the first time a room temperature operating FET devices in dark conditions.

Perspectives

Our results elucidate the key principles for achieving gate modulated carrier transport in hybrid perovskite thin films. The demonstration of operational perovskite FETs at room temperature provides an excellent and viable platform for study the charge transport properties. Advanced functionalities can be explored such as ultra-low light or radiation detection modulated by the gate electrical field among others[4-6].

However, further analysis and understanding would be needed in order to obtain a high efficient perovskite based field effect transistors with better current voltage characteristics:

1. Increase the low current values measured in the case of PFETs. The first simple idea is to decrease the channel length just by using the geometrical effect. Consequently, the amount of defects will decrease in the channel due to the decrease of the number of grain boundary.

This step must overcome the hydrophobicity of the perovskite solution on the gold electrodes. In our case, any devices below $L = 70 \mu\text{m}$ were obtained. The solution could be a plasma treatment of gold to increase the wettability.

2. As grain boundary can affect the FET performances, the addition of bifunctional organic materials (4-ABPACl) in MAPbI₃ precursor solution could help to passivate the defects [12].
3. Analyze the ion diffusion inside perovskite layers by using low temperature measurements on each dielectric based devices.
4. The use of other different dielectrics (such Al₂O₃ or Ta₂O₅ or Cytop) would be helpful to fully understand the origin of the aging effect on the device performances and determine if the n-type transport observed in this thesis comes from the semiconductor/dielectric interface or from the passivation of the vacancies.
5. Increase the reproducibility of the device fabrication by better control the hot casting technique deposition in terms of temperature.
6. Study on our Schottky barrier FET the effect of the metallization on the device performances.

II) Perovskite solar cells fabricated under different atmospheres

The objective of this work is the fabrication of solar cells in nitrogen controled atmosphère and in air conditions. We used a thermal treatment during perovskite deposition which consists in set up an infrared lamp on the top of the spin coater to avoid the moisture impact. This technique allows us to obtain reproducible perovskite solar cells fabricated under humid conditions (RH>60%) reaching PCEs up to 5,05 % ± 0,1. The perovskite thicknesses and annealing temperature were optimized to obtain the maximum efficiency. The best perovskite solar cells with 8% PCE were obtained under a nitrogen atmosphere.

Perspectives

The air process shows very low efficiency compared to the literature and for the same solution we obtain 8% in nitrogen.

Further optimization could be done in order to improve the devices performances:

1. The use of the anti-solvent technique during the perovskite deposition allows to form an intermediate MAI-PbI₂-solvent to delay the crystal growth of perovskites. It has been reported that solvents such Ethyl acetate acts as a moisture absorber during the spin-

coating which allows a better control on the growth and morphology of perovskite films in humid environments.

2. using inorganic metal oxides as ETL and HTL such NiO or ZnO or TiO₂ [9,11 to obtain an efficient charge collection improving consequently the device performances.
3. Incorporating additives such as imidazolium iodide, PCBM or alkali metal ions in the perovskite precursor solution [13] to control the rate of perovskite crystallization. This facilitates the nucleation and modulates the kinetics of crystal growth during crystallization [14].

References

- [1] W. Nie, H. Tsai, R. Asadpour, J.-C. Blancon, A.J. Neukirch, G. Gupta, J.J. Crochet, M. Chhowalla, S. Tretiak, M.A. Alam, H.-L. Wang, A.D. Mohite, High-efficiency solution-processed perovskite solar cells with millimeter-scale grains, *Science*. 347 (2015) 522–525. doi:10.1126/science.aaa0472.
- [2] H. Tsai, R. Asadpour, J.-C. Blancon, C.C. Stoumpos, O. Durand, J.W. Strzalka, B. Chen, R. Verduzco, P.M. Ajayan, S. Tretiak, others, Light-induced lattice expansion leads to high-efficiency perovskite solar cells, *Science*. 360 (2018) 67–70.
- [3] C. Katan, A.D. Mohite, J. Even, Entropy in halide perovskites, *Nature Materials*. 17 (2018) 377.
- [4] W. Knap, V. Kachorovskii, Y. Deng, S. Rumyantsev, J.-Q. Lü, R. Gaska, M. Shur, G. Simin, X. Hu, M.A. Khan, others, Nonresonant detection of terahertz radiation in field effect transistors, *Journal of Applied Physics*. 91 (2002) 9346–9353.
- [5] L. Vicarelli, M. Vitiello, D. Coquillat, A. Lombardo, A. Ferrari, W. Knap, M. Polini, V. Pellegrini, A. Tredicucci, Graphene field-effect transistors as room-temperature terahertz detectors, *Nature Materials*. 11 (2012) 865.
- [6] A. El Fatimy, S.B. Tombet, F. Teppe, W. Knap, D. Veksler, S. Rumyantsev, M. Shur, N. Pala, R. Gaska, Q. Fareed, others, Terahertz detection by GaN/AlGaN transistors, *Electronics Letters*. 42 (2006) 1342–1344.
- [7] P. Mittal, B. Kumar, Y.S. Negi, B.K. Kaushik, R. Singh, Channel length variation effect on performance parameters of organic field effect transistors, *Microelectronics Journal*. 43 (2012) 985–994.
- [8] A. Marchioro, J. Teuscher, D. Friedrich, M. Kunst, R. Van De Krol, T. Moehl, M. Grätzel, J.-E. Moser, Unravelling the mechanism of photoinduced charge transfer processes in lead iodide perovskite solar cells, *Nature Photonics*. 8 (2014) 250.
- [9] H.-S. Kim, N.-G. Park, Parameters affecting I–V hysteresis of CH₃NH₃PbI₃ perovskite solar cells: effects of perovskite crystal size and mesoporous TiO₂ layer, *The Journal of Physical Chemistry Letters*. 5 (2014) 2927–2934.
- [10] P. Rudolph, A. Engel, I. Schentke, A. Grochocki, Distribution and genesis of inclusions in CdTe and (Cd,Zn)Te single crystals grown by the Bridgman method and by the travelling heater method, *J. Cryst. Growth*. 147 (1995). doi:10.1016/0022-0248(94)00617-2.
- [11] J. You, L. Meng, T.-B. Song, T.-F. Guo, Y.M. Yang, W.-H. Chang, Z. Hong, H. Chen, H. Zhou, Q. Chen, others, Improved air stability of perovskite solar cells via solution-processed metal oxide transport layers, *Nature Nanotechnology*. 11 (2016) 75.
- [12] X. Li, M.I. Dar, C. Yi, J. Luo, M. Tschumi, S.M. Zakeeruddin, M.K. Nazeeruddin, H. Han, M. Grätzel, Improved performance and stability of perovskite solar cells by crystal crosslinking with alkylphosphonic acid ω -ammonium chlorides, *Nature Chemistry*. 7 (2015) 703.
- [13] A.-N. Cho, N.-G. Park, Impact of interfacial layers in perovskite solar cells, *ChemSusChem*. 10 (2017) 3687–3704.
- [14] P.-W. Liang, C.-Y. Liao, C.-C. Chueh, F. Zuo, S.T. Williams, X.-K. Xin, J. Lin, A.K.-Y. Jen, Additive enhanced crystallization of solution-processed perovskite for highly efficient planar-heterojunction solar cells, *Advanced Materials*. 26 (2014) 3748–3754.
- [15] M. Li, X. Yan, Z. Kang, X. Liao, Y. Li, X. Zheng, P. Lin, J. Meng, Y. Zhang, Enhanced efficiency and stability of perovskite solar cells via anti-solvent treatment in two-step deposition method, *ACS Applied Materials & Interfaces*. 9 (2017) 7224–7231.

RÉSUMÉ EN FRANÇAIS

Les pérovskites hybrides organiques-inorganiques sont un groupe de matériaux décrit par la formule chimique générique AMX_3 (A = cation organique, M = cation métallique et X = anion halogène). Ces matériaux ont fait l'attention de nombreuses recherches durant ces dernières années principalement dans le domaine des énergies renouvelables où ils démontrent des performances exceptionnelles.

En effet les rendements de conversion d'énergie des cellules solaires à base de pérovskite hybrides ont été considérablement améliorés, passant d'environ 3,8% [1] en 2009 à environ 22% actuellement [2–4]. Ces rendements sont alors tout à fait comparables à ceux des cellules solaires à base de silicium permettant ainsi une réduction des coûts technologiques par l'utilisation de ce nouveau matériau [5,6]. Les propriétés exceptionnelles des pérovskites organométalliques sont attribuées au fait qu'elles associent les avantages des composés inorganiques cristallins à ceux des molécules organiques, ce qui permet l'obtention d'une faible masse effective, une importante absorption optique, une faible énergie de liaison de l'exciton à température ambiante et une faible densité de pièges et de défauts [7-13]. Ces propriétés exceptionnelles peuvent aussi être utilisées dans d'autres dispositifs optoélectroniques tels que les détecteurs de rayonnement (rayons gamma et rayons X) [14,15], les lasers à pompage optique [16], les diodes électroluminescentes (DEL) [16,17] et les transistors à effet de champ (FET) [18–20].

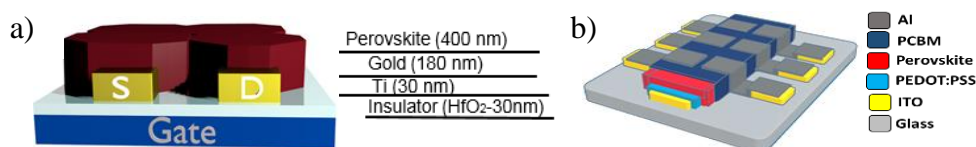
Cependant, bien que les systèmes photovoltaïques montrent d'excellentes performances, les pérovskites hybrides organiques-inorganiques présentent des inconvénients pratiques limitant le passage à la production. Plusieurs problèmes majeurs demeurent comme : la toxicité du plomb, la sensibilité de la pérovskite à l'atmosphère [21-23] et la difficulté de réalisation de dispositifs électroniques à la température ambiante [17-19] limitant ainsi les nombreuses applications.

Dans cette thèse, nous nous sommes intéressés à deux défis liés aux pérovskite hybrides: le développement de transistors à effet de champ fonctionnant à température ambiante et le développement d'une méthode efficace et à faible coût pour la fabrication de cellules solaires dans des conditions atmosphériques.

Cette thèse est divisée en cinq chapitres:

Dans le chapitre 1, nous présentons l'état de l'art concernant les matériaux à base de pérovskite hybrides en décrivant brièvement leurs origines, leurs caractéristiques et propriétés et les principales applications. En fonction de la composition, le groupe des pérovskites peut être séparé en deux catégories principales [7]: les pérovskites d'oxydes inorganiques (dont la composition est constituée de cations inorganiques oxydés) et les pérovskites d'halogénures (qui présentent un mélange de cations halogénés dans la structure cristalline). Les matériaux à base d'oxyde de pérovskite sont connus pour présenter plusieurs propriétés physiques telles que la ferroélectricité, le ferromagnétisme, la piézoélectricité et la supraconductivité. Ils étaient couramment utilisés comme piles à combustible à oxyde solide, comme membranes de perméation pour l'oxygène et pour la photocatalyse [25–27]. D'un autre côté, les pérovskites halogénées et plus particulièrement les pérovskites hybrides (contenant un cation organique) sont considérées comme un matériau émergent pour le développement d'applications optoélectroniques [7-13]. La fin du chapitre se focalise sur les transistors à effet de champ et les cellules solaires. Nous utilisons la structure transistor pour analyser les propriétés de transport dans ces matériaux. Cependant, la réalisation de transistors à la température ambiante à base de pérovskite reste complexe. Les cellules solaires quant à elles présentent un excellent rendement mais nécessitent une fabrication en atmosphère contrôlée. Nous présenterons donc les avancées récentes dans ce domaine ainsi que les principales difficultés à dépasser.

Le chapitre 2, présente les différents matériaux et les étapes de fabrication utilisées dans cette thèse pour le développement de transistors à effet de champ et de cellules solaires. Les principes de fonctionnement de base pour chaque application sont également présentés. Les transistors à effet de champ (FET) ont été fabriqués en utilisant une structure de grille enterrée, tandis que les cellules solaires ont été fabriquées à l'aide de la configuration inversée, comme illustré à la Figure 1.



Pour la fabrication de FET, nous avons utilisé la technique d'enduction sur substrat chauffé développé par Nie et al. [12] pour faire croître des cristaux de pérovskite millimétrique. Cette

technique consiste à déposer la solution de précurseur de pérovskite (70 ° C) sur des substrats préchauffés (180 ° C), la cristallisation finale se réalise par un recuit à 100 ° C pendant 10 minutes. Dans le cas de la fabrication d'une cellule solaire à l'ambiante, nous avons placé une lampe infrarouge sur le dessus de la tournette afin de chauffer en continu l'échantillon à 70 ° C pendant le dépôt de la pérovskite. Après cette étape, les échantillons ont été recuits à 100 ° C pendant 90 minutes.

La dernière partie de ce chapitre est consacrée à la description des techniques utilisées pour l'étude de la morphologie des films et la caractérisation des dispositifs, telles que la diffraction des rayons X (XRD), la diffraction des rayons X en incidence rasante (GIWAX), le spectre d'absorption optique, la microscopie à force atomique (AFM), microscopie électronique à balayage (SEM) et caractérisation courant-tension des dispositifs.

Dans le chapitre 3, nous analyserons le fonctionnement à température ambiante de transistors à base de pérovskite hybride MAPbI₃ (iodure (I) de méthylammonium (MA) et de plomb (Pb)) dans des conditions d'obscurité. Nous décrivons d'abord la morphologie des couches minces de pérovskites en utilisant des images optiques, la diffraction des rayons X et des mesures d'absorbance. Ces résultats confirment le fait que nous obtenons des films minces polycristallins dont la taille des cristallites est de l'ordre de la centaine de micromètres. Nous avons utilisé MAPbI₃ en tant que couches semi-conductrices pour réaliser des transistors à effet de champ. Différents diélectriques d'isolant de grille ont été testés et les meilleures performances ont été obtenues avec du HfO₂. Les dispositifs montrent une modulation pour des porteurs de type p avant polarisation (Figure 2) et un comportement ambipolaire ensuite.

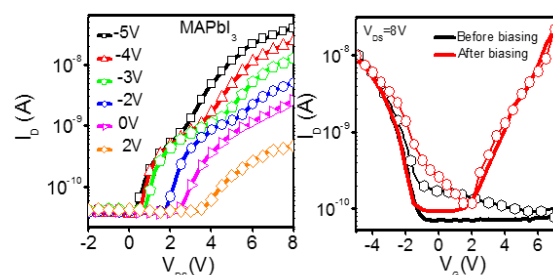


Figure 2. Caractéristiques de sortie et de transfert des FET à base de pérovskite MAPbI₃.

L'origine du courant de type n peut être attribué à une conduction par les pièges et les défauts d'interface. De plus dans le cas de notre dispositif à barrière Schottky, il est souvent observé un comportement ambipolaire par l'injection d'électrons à travers la barrière. Néanmoins, une analyse plus poussée serait nécessaire pour bien comprendre ces phénomènes.

Nous avons également étudié l'impact de la dimension du canal sur les transistors. Une plus grande longueur de canal entraîne un nombre plus élevé de joints de grains dans le canal et par conséquent, des performances plus faibles. On notera que nos dispositifs présentent une hystérésis notable sur leurs caractéristiques de transfert.

Au chapitre 4, nous utilisons la pérovskite hybride contenant comme cation du Césium et du formamidinium (FA) dont la composition est $\text{FA}_{0.75-x}\text{MA}_{0.25}\text{Cs}_x\text{PbI}_3$. La combinaison du Césium (Cs) et du Formamidinium permet d'obtenir une meilleure stabilité en température, ceci a par ailleurs déjà été étudié dans la littérature [28,29]. Nous étudions la morphologie du film de pérovskite à cations mixtes avec différentes concentrations de Césium ($x = 0,05, 0,15$ et $0,25$). Les résultats indiquent qu'une concentration de Cs de $x = 0,25$ conduit à une meilleure qualité de film et à de meilleures performances du dispositif avec une hystérésis réduite et des valeurs de transconductance élevées (Figure 3). Nous avons également effectué une analyse de stabilité et de reproductibilité des FET à base de $\text{FA}_{0,5}\text{MA}_{0,25}\text{Cs}_{0,25}\text{PbI}_3$ et MAPbI_3 mettant en évidence un fonctionnement stable à court terme où les dispositifs présentent une faible dégradation après 14 heures de mesures en continu.

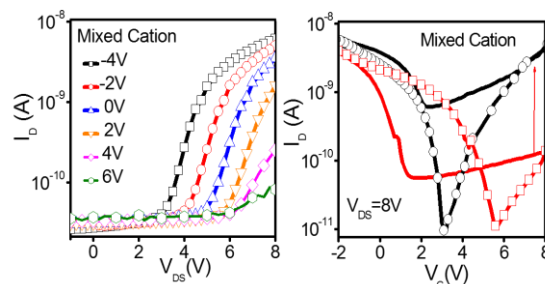


Figure 3. Caractéristiques de sortie et de transfert des FET à base de pérovskite à cations mixtes.

Le chapitre 5 présente les cellules solaires fabriquées dans le cadre de cette thèse. Nous avons étudié deux conditions de synthèse, soit sous atmosphère contrôlée d'azote, soit sous air (conditions d'humidité et de température habituelles). Pour la fabrication de cellules solaires à base de pérovskite dans des conditions atmosphériques, nous avons mis en place un traitement thermique lors du dépôt de pérovskite afin de limiter l'effet d'humidité. Plus précisément, nous avons utilisé une lampe infrarouge (IR) permettant de chauffer de manière continue l'échantillon à 70°C . Une optimisation en termes de température de recuit, d'épaisseur ont permis d'atteindre un rendement de 5%. Les cellules obtenues quant à elles sous atmosphère

d'azote ont démontré des rendements de l'ordre de 8% après l'amélioration des résistances séries et parallèle de ces cellules (Figure 4).

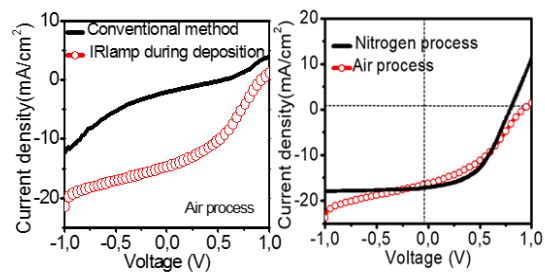


Figure 4. Densité de courant de cellules solaires à base de pérovskite réalisées sous air et sous atmosphère d'azote.

References

- [1] D.B. Mitzi, C. Feild, W. Harrison, A. Guloy, Conducting tin halides with a layered organic-based perovskite structure, *Nature*. 369 (1994) 467.
- [2] M.A. Green, Y. Hishikawa, W. Warta, E.D. Dunlop, D.H. Levi, J. Hohl-Ebinger, A.W. Ho-Baillie, Solar cell efficiency tables (version 50), *Progress in Photovoltaics*. 25 (2017).
- [3] W.S. Yang, B.-W. Park, E.H. Jung, N.J. Jeon, Y.C. Kim, D.U. Lee, S.S. Shin, J. Seo, E.K. Kim, J.H. Noh, others, Iodide management in formamidinium-lead-halide-based perovskite layers for efficient solar cells, *Science*. 356 (2017) 1376–1379.
- [4] M. Saliba, T. Matsui, J.-Y. Seo, K. Domanski, J.-P. Correa-Baena, M.K. Nazeeruddin, S.M. Zakeeruddin, W. Tress, A. Abate, A. Hagfeldt, others, Cesium-containing triple cation perovskite solar cells: improved stability, reproducibility and high efficiency, *Energy & Environmental Science*. 9 (2016) 1989–1997.
- [5] K. Masuko, M. Shigematsu, T. Hashiguchi, D. Fujishima, M. Kai, N. Yoshimura, T. Yamaguchi, Y. Ichihashi, T. Mishima, N. Matsubara, others, Achievement of more than 25% conversion efficiency with crystalline silicon heterojunction solar cell, *IEEE Journal of Photovoltaics*. 4 (2014) 1433–1435.
- [6] A. Shah, P. Torres, R. Tscharnner, N. Wyrsh, H. Keppner, Photovoltaic technology: the case for thin-film solar cells, *Science*. 285 (1999) 692–698.
- [7] P. Gao, M. Grätzel, M.K. Nazeeruddin, Organohalide lead perovskites for photovoltaic applications, *Energy & Environmental Science*. 7 (2014) 2448–2463.
- [8] A. Chilvery, S. Das, P. Guggilla, C. Brantley, A. Sunda-Meya, A perspective on the recent progress in solution-processed methods for highly efficient perovskite solar cells, *Science and Technology of Advanced Materials*. 17 (2016) 650–658.
- [9] M.D. McGehee, Materials science: fast-track solar cells, *Nature*. 501 (2013) 323.
- [10] N.J. Jeon, J.H. Noh, Y.C. Kim, W.S. Yang, S. Ryu, S.I. Seok, Solvent engineering for high-performance inorganic–organic hybrid perovskite solar cells, *Nature Materials*. 13 (2014) 897.
- [11] P. Fan, D. Gu, G.-X. Liang, J.-T. Luo, J.-L. Chen, Z.-H. Zheng, D.-P. Zhang, High-performance perovskite CH₃NH₃PbI₃ thin films for solar cells prepared by single-source physical vapour deposition, *Scientific Reports*. 6 (2016) 29910.
- [12] W. Nie, H. Tsai, R. Asadpour, J.-C. Blancon, A.J. Neukirch, G. Gupta, J.J. Crochet, M. Chhowalla, S. Tretiak, M.A. Alam, H.-L. Wang, A.D. Mohite, High-efficiency solution-

- processed perovskite solar cells with millimeter-scale grains, *Science*. 347 (2015) 522–525. doi:10.1126/science.aaa0472.
- [13] W. Chen, Y. Wu, Y. Yue, J. Liu, W. Zhang, X. Yang, H. Chen, E. Bi, I. Ashraful, M. Grätzel, others, Efficient and stable large-area perovskite solar cells with inorganic charge extraction layers, *Science*. (2015) aad1015.
- [14] J. Ding, High detectivity and rapid response in perovskite CsPbBr₃ single-crystal photodetector, *J. Phys. Chem. C*. 121 (2017). doi:10.1021/acs.jpcc.7b01171.
- [15] D.N. Dirin, I. Cherniukh, S. Yakunin, Y. Shynkarenko, M.V. Kovalenko, Solution-grown CsPbBr₃ perovskite single crystals for photon detection, *Chem. Mater*. 28 (2016). doi:10.1021/acs.chemmater.6b04298.
- [16] S.A. Veldhuis, P.P. Boix, N. Yantara, M. Li, T.C. Sum, N. Mathews, S.G. Mhaisalkar, Perovskite materials for light-emitting diodes and lasers, *Advanced Materials*. 28 (2016) 6804–6834.
- [17] Y. Ling, Z. Yuan, Y. Tian, X. Wang, J.C. Wang, Y. Xin, K. Hanson, B. Ma, H. Gao, Bright light-emitting diodes based on organometal halide perovskite nanoplatelets, *Advanced Materials*. 28 (2016) 305–311.
- [18] X.Y. Chin, D. Cortecchia, J. Yin, A. Bruno, C. Soci, Lead iodide perovskite light-emitting field-effect transistor, *Nature Communications*. 6 (2015) 7383.
- [19] F. Li, C. Ma, H. Wang, W. Hu, W. Yu, A.D. Sheikh, T. Wu, Ambipolar solution-processed hybrid perovskite phototransistors, *Nature Communications*. 6 (2015) 8238.
- [20] Y. Mei, C. Zhang, Z. Vardeny, O. Jurchescu, Electrostatic gating of hybrid halide perovskite field-effect transistors: balanced ambipolar transport at room-temperature, *MRS Communications*. 5 (2015) 297–301.
- [21] M.K. Gangishetty, R.W. Scott, T.L. Kelly, Effect of relative humidity on crystal growth, device performance and hysteresis in planar heterojunction perovskite solar cells, *Nanoscale*. 8 (2016) 6300–6307.
- [22] J. Troughton, K. Hooper, T.M. Watson, Humidity resistant fabrication of CH₃NH₃PbI₃ perovskite solar cells and modules, *Nano Energy*. 39 (2017) 60–68.
- [23] Q. Tai, P. You, H. Sang, Z. Liu, C. Hu, H.L. Chan, F. Yan, Efficient and stable perovskite solar cells prepared in ambient air irrespective of the humidity, *Nature Communications*. 7 (2016) 11105.
- [25] J. Zhu, H. Li, L. Zhong, P. Xiao, X. Xu, X. Yang, Z. Zhao, J. Li, Perovskite oxides: preparation, characterizations, and applications in heterogeneous catalysis, *Acs Catalysis*. 4 (2014) 2917–2940.

- [26] M. Kubicek, A.H. Bork, J.L. Rupp, Perovskite oxides—a review on a versatile material class for solar-to-fuel conversion processes, *Journal of Materials Chemistry A*. 5 (2017) 11983–12000.
- [27] M. Pena, J. Fierro, Chemical structures and performance of perovskite oxides, *Chemical Reviews*. 101 (2001) 1981–2018.
- [28] N. Pellet, P. Gao, G. Gregori, T.-Y. Yang, M.K. Nazeeruddin, J. Maier, M. Grätzel, Mixed-organic-cation Perovskite photovoltaics for enhanced solar-light harvesting, *Angewandte Chemie*. 126 (2014) 3215–3221.
- [29] D.P. McMeekin, G. Sadoughi, W. Rehman, G.E. Eperon, M. Saliba, M.T. Hörantner, A. Haghighirad, N. Sakai, L. Korte, B. Rech, others, A mixed-cation lead mixed-halide perovskite absorber for tandem solar cells, *Science*. 351 (2016) 151–155.

Titre : Développement et caractérisation des dispositifs à base de pérovskite : transistors à effet de champ et cellules solaires

Mots clés : Pérovskite Hybride, transistors à effet de champ, cellules solaires, diélectrique haute permittivité, MAPbI₃, FAMACsPbI₃

Résumé : L'objectif de cette thèse était l'étude de dispositifs électroniques à base de pérovskites hybrides. Dans ce cadre nous avons développé et fabriqué des transistors à effet de champ (FET) ainsi que des cellules solaires à base de pérovskite.

Dans le cas des transistors, en utilisant des couches minces de pérovskites hybride hautement cristallisées nous avons réalisé des transistors ambipolaires fonctionnant à la température ambiante et présentant une hystérésis faible, une transconductance élevée (pour ce type de matériau), et un rapport $I_{on} / I_{off} > 10^4$. Dans le cadre de cette thèse l'utilisation de plusieurs diélectriques nous a permis d'obtenir une forte modulation de la conductance du canal avec des tensions de grille relativement faibles (4-6V). Dans ce cadre l'oxyde d'Hafnium de permittivité relative $\epsilon_r=23.5$ a montré de très bonnes performances et une très bonne compatibilité pour la croissance de pérovskite hybride.

Après plusieurs étapes de polarisation les dispositifs ont présenté un fonctionnement stabilisé et ont été mesurés au cours des cycles consécutifs pendant 14 heures avec peu de changement dans leurs performances. Nous avons mis en évidence que l'augmentation du champ électrique a permis la formation d'un canal de trous à l'interface. La polarisation consécutive des dispositifs à base de HfO₂/pérovskite a amené à la création d'un second courant d'électrons et a mis en évidence un fonctionnement ambipolaire final. L'ensemble des dispositifs ont présenté une hystérésis dont l'amplitude était parfois non négligeable. Cela a démontré la présence de charges mobiles ioniques aux interfaces qui influence les courants de sorties du dispositif.

Dans la dernière partie de la thèse nous nous sommes intéressés à la croissance de pérovskite hybride pour la production de cellules solaires. Nous avons étudié les deux conditions de croissance suivantes : conditions sous air normal (humidité relative > 60%) et en atmosphère d'azote en boîtes à gants (humidité relative < 0.1 ppm). Par ces deux voies nous avons obtenu respectivement des rendements de conversion photovoltaïque respectivement de 5% et 8%.

Titre: Development and characterization of perovskite based devices: field effect transistors and solar cells.

Keywords : Hybrid perovskite, field effect transistors, solar cells, high k dielectric, MAPbI₃, FAMACsPbI₃

Abstract : The objective of this thesis was the study of electronic devices based on hybrid perovskites. In this context we have developed and produce field effect transistors (FETs) and solar cells based on hybrid perovskite material.

In the case of transistors, using thin layers of highly crystallized hybrid perovskites we have made ambipolar transistors operating at room temperature and having low hysteresis, high transconductance (for this type of material) and a ratio of $I_{on} / I_{off} > 10^4$. In the context of this thesis, the use of several dielectrics allowed us to obtain a high modulation of the channel conductance with relatively low gate voltages (4-6V). Hafnium oxide with relative permittivity $\epsilon_r = 23.5$ showed very good performances and a very good compatibility for the hybrid perovskite growth.

After several polarization steps the devices exhibited stabilized operation and were measured in consecutive cycles for 14 hours with small change in their performance. We have shown that the increase of the electric field allowed the formation of a hole channel at the interface. The successive polarization of HfO₂ / perovskite-based devices led to the creation of a second electron current and demonstrated a final ambipolar device. All the devices presented a hysteresis with amplitude sometimes not negligible. This demonstrated the presence of mobile ion charges at the interfaces that influence the output currents of the device.

In the last part of the thesis we focused our work in hybrid perovskite growth for the production of solar cells. We have studied two growth conditions: conditions under normal air (relative humidity > 60%) and nitrogen atmosphere in glove boxes (relative humidity < 0.1 ppm). By these two paths we obtained photovoltaic conversion efficiencies of 5% and 8% respectively.

